Model and Control Validation of a High Speed Supercavitating Vehicle

A THESIS
SUBMITTED TO THE FACULTY OF THE GRADUATE SCHOOL
OF THE UNIVERSITY OF MINNESOTA
BY

David Escobar Sanabria

IN PARTIAL FULFILLMENT OF THE REQUIREMENTS
FOR THE DEGREE OF
MASTER OF SCIENCE

Gary J. Balas, Roger E.A. Arndt, Advisers

July, 2012

Acknowledgements

I want to express all my gratitude to my academic advisors, in chronological order: Professor Ernesto Cordoba Nieto of the National University of Colombia for his continuous support during and after my undergraduate studies, his guidance and encouragement have been indispensable for my career; Professor Jaime Ivan Ordoez of the National University of Colombia for his support, advice, and extraordinary encouragement and help in finding alternatives for my graduate education. Third, my current advisor; Professor Gary J. Balas for giving me the great opportunity to work and learn with him as well as for his support, patience, advice, and flexibility; finally, professor Roger E.A. Arndt for his support, opportunities, encouragement, time, and guidance.

I want also to acknowledge Professor Demoz Gebre-Egziabher for his advice throughout my years in Minnesota and for serving on my thesis committee.

I would also like to thank current and previous members from the Cavitation and Bubbly Flows Research Group at the Saint Anthony Falls Laboratory: Austin Murch, Ellison Kawakami, Seung Jae Lee, Hamid Mokhtarzadeh, Arnar Hjartarson, and Jon Fraatz. Their work, discussions, assistance, and feedback have been very important for the development of this thesis. This group has been an admirable example of human cooperation, and I am glad to have been part of it.

I want also to thank all who have shared with me academic and life experiences during my time in the United States.

This work has been supported by the Office of Naval Research (ONR) under contract number N00014-12-1-0058, project title: "Development of Control Strategies for Very High Speed Cavity-Running Bodies: Simulations and Small-Scale Experiments". Dr. Ron Joslin is the contract monitor.

Dedication

A mi amada familia: Mirian, Humberto, Francisco y Lucia por su apoyo

y

A mi adorada amiga Eliana Gil, tu luz y energia estaran conmigo por siempre

Abstract

Underwater, supercavitating vehicles can achieve higher speeds than conventional submarine vehicles due to the drag reduction result of the vehicle-fluid isolation. Research on the control of high speed supercavitating vehicles has led to theoretical solutions; however, validation and testing of control laws to drive the vehicle motion are expensive, complex and have not been presented in the open literature.

This thesis presents an approach to the experimental validation of control systems for a supercavitating test vehicle in the longitudinal plane. The supercavitating vehicle considered in this thesis consists of a cylindrical body with a disk cavitator and two lateral, sweptback, wedge fins. The control validation platform enables the use of the high speed water tunnel located at the Saint Anthony Falls Laboratory to recreate realistic flight scenarios including the effect of ocean waves on the vehicle. The test platform uses the hydrodynamic forces produced by the fluid-vehicle interaction, embedded flight computer, and analytical equations of motion to test the closed-loop system performance in real time. The equations of motion for the test vehicle are derived based on experiments in which the effect of perturbed flow on the vehicle motion is also considered. A controller for the test vehicle is synthesized using H-infinity optimization. Water tunnel tests successfully validated the supercavitating vehicle model and controller. The objectives were tracking of pitch angle reference commands and rejection of disturbances produced by an oscillating foil gust generator.

The experimental results show the accuracy of the vehicle modeling and control design as well as the effect of the perturbed flow on the closed-loop system performance. The experience gained from this work enabled the introduction of the next generation test platform capable to capture planing phenomena.

Contents

List of Tables

List of Figures

Chapter 1

Introduction

1.1 Motivation and Objectives

An underwater vehicle traveling at high speeds inside a continuous gas bubble is referred to as High Speed Supercavitating Vehicle (HSSV). A HSSV is able to achieve higher speeds than non-supercavitating vehicles on the order of 70 [m/s] because of the drag reduction achieved by decreasing the contact area between the vehicle and the water [1]. A HSSV also attenuates hydrodynamic vibrations and flow perturbations coming from ocean waves due to the fluid-vehicle isolation. Research on HSSV dynamics, control and guidance has been of great interest due to the speeds that these vehicles can achieve [2].

The physics and control of supercavitating vehicles can be understood by using facilities as the high speed water tunnel located at the Saint Anthony Falls Laboratory (SAFL) of the University of Minnesota. The SAFL facilities motivated and enabled this research, in which the main goal is the development of a system for testing control laws that drive the motion of a HSSV prototype. The vehicle prototype considered in this thesis, shown in Figure 1.1, consists of a cylindrical body with two actuated control surfaces: a disk cavitator and two lateral sweptback wedge fins.

The motion of a HSSV depends upon the forces acting at its center of gravity (c.g.). These forces are generated by the control surfaces (cavitator and fins), perturbed flow (gusts), planing occurring when the vehicle pierces the bubble, and gravitational acceleration. Mathematical models for the considered vehicle architecture have been presented in [3], [4], and [5]. Nevertheless, qualitative and quantitative descriptions of

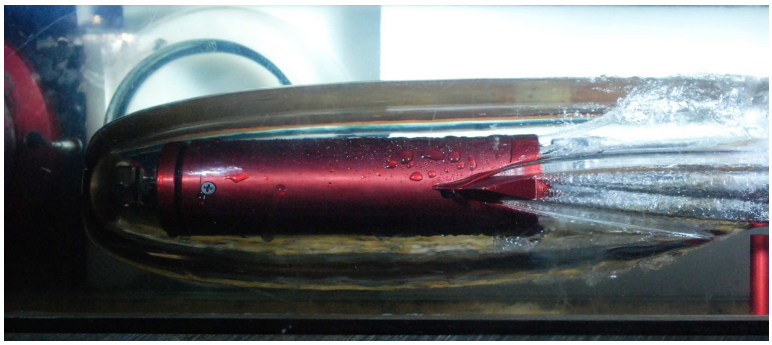

Figure 1.1: Supercavitating test vehicle (COSCIS-3) at SAFL-high speed water tunnel

forces generated by the perturbed flow have not been explored and less in the context of the vehicle motion.

Dynamical models and control strategies for supercavitating vehicles have been proposed in [4], [5], [6]; however, the open literature shows that these theoretical results have not been experimentally validated. In fact, validation and testing of control systems in realistic scenarios represents a challenge in terms of infrastructure, time, and operational costs; for example, undersea testing is an expensive and complicated procedure. Early validation and testing of control systems in realistic scenarios can reduce costs associated with undersea operations. Thus, the main objective of this thesis is the development of a cost efficient experimental system devoted to validate control algorithms for a supercavitating vehicle prototype. The scope of this thesis is the control of a non-planing HSSV.

Simple mathematical models of the test vehicle considered in the thesis are needed to accurately describe the vehicle dynamics, construct the control test platform, and design control laws for the vehicle motion. Hence, the second objective of this thesis is the experimental validation of force models for the HSSV prototype. The longitudinal equations of motion are derived based on forces produced by swept wedge fins, disk cavitator, and perturbed flow produced by a oscillating foil gust generator that emulates the effect of ocean waves. Methods for generating planing and initial measurements of planing force are presented; however, mathematical descriptions of planing forces are not derived in this thesis.

1.2 Approach

An experimental platform is developed to study the interaction of a HSSV test vehicle and the supercavity. The platform is able to measure the forces and moments acting on a supercavitating test vehicle. These forces and moments are produced by: the control surface deflections (cavitator and fins), an oscillating foil gust generator, and combination of deflections of the gust generator and cavitator that lead to planing.

A simple model of the HSSV longitudinal motion is created using force data from experiments. This model is given in terms of hydrodynamic, inertial, and geometric parameters. A linear version of the HSSV longitudinal motion is also derived.

A system is developed to test the control systems of a HSSV via hybrid testing, a method that combines analytical and experimental validation approaches. Hybrid testing integrates numerical simulation and real-time measurements of physical variables to emulate and test the operation of a dynamical system. This methodology has been successfully used in structural engineering to evaluate the dynamic response of structures to earthquakes and strong winds [7], [8]. Hybrid testing is one step beyond simulation of dynamical systems.

The hybrid test system, referred to as the Hybrid Test Platform for Supercavitating Vehicles (HyTPSV), reproduces flight scenarios as follows: measurements of hydrodynamic forces applied to the supercavitating test vehicle are used by the real-time simulation computer to propagate the vehicle equations of motion. The vehicle states (pitch rate, pitch angle, velocity components), computed through the equations of motion, are transmitted to the vehicle embedded computer, where the control algorithms are executed. The control law commands the cavitator and fin deflections that vary the hydrodynamic forces applied to the experimental vehicle to drive its emulated motion. These forces are fed back to the dynamics simulation computer to complete the loop.

A control law designed via H-infinity optimization ([9], [10]) is successfully tested on the system. Its objective is to track pitch angle reference commands and reject disturbances applied to the cavitator command and produced by the gust generator installed in the SAFL high speed water tunnel.

1.3 Thesis Structure

This thesis consists of seven chapters including this introductory Chapter. Chapter 2 introduces the physics of a HSSV. Chapter 3 describes the experimental infrastructure and methods developed to model the vehicle longitudinal motion. Chapter 4 presents results of experiments and derives a simple model of the HSSV longitudinal motion. The force effectiveness of the control surfaces, (cavitator and fins) and disturbances produced by the gust generator are discussed as are the planing forces generated through deflections of the cavitator and gust generator. The effect of perturbed flow on the supercavity geometry and its mitigation via cavitator actuation is also presented. Finally, the mathematical model of the HSSV motion is derived by using theoretical and experimental results.

Chapter 5 presents the experimental infrastructure and methods to validate control laws of the HSSV prototype. The high level architecture and specific implementation of the hybrid test platform are described. The control design based on models of the HSSV motion, actuation, and time delay is presented. Finally, experiments to evaluate the tracking and disturbance rejection performance of the closed-loop system are described. Chapter 6 discusses results of the control experiments presented in chapter 5.

Finally, chapter 7 presents the conclusions on the work presented throughout this thesis. The future perspectives on the modeling and control validation are also discussed. In addition, a new generation test platform that overcomes problems of the hybrid test platform developed in this thesis is proposed.

Chapter 2

Physics of a HSSV

This chapter presents a brief background used throughout this thesis on the supercavity physics and HSSV longitudinal motion. Section 2.1 introduces the supercavitation phenomenon. Section 2.2 describes the architecture of the HSSV considered in this thesis as well as the general form of the HSSV longitudinal equations of motion. These equations are used in Chapters 4, 5 and 6 to derive the longitudinal vehicle dynamics, develop the control validation infrastructure and design a control law for the HSSV motion. The model of cavitator forces derived by Logvinovich [11] is described in Section 2.3. These models are experimentally validated in Section 4.1.1. Section 2.4 describes the general form of the fin forces, which are used in Section 4.1.2, together with experiments described in Section 3.2.2, to derive simple mathematical descriptions of the fin forces. Section 2.6 presents the causes and effects of perturbed flow on underwater vehicles. The impact of perturbed flow on the HSSV motion is discussed in more detail in Section 4.1.3. Section 2.5 qualitatively describes the planing phenomenon, but not in detail since this thesis is mainly focused on non-planing supercavitating vehicles. Finally, Section 2.7 presents a brief description of the supercavity geometry that is used in Section 3.2.5 to support the experimental generation of planing.

2.1 Supercavitation

Supercavitation occurs when a body is partially or totally enveloped by a large and continuous gas bubble called supercavity [1], [12]. A supercavitating vehicle can increase

the speed as it travels inside a supercavity formed at the cavitator located at the nose of the vehicle.

The cavitation number (σ), described in equation 2.1, is a parameter used to describe the geometry of the supercavity and forces generated at the cavitator.

$$\sigma = \frac{2(p_\infty - p_c)}{\rho U_\infty^2} \tag{2.1}$$

p_∞ is the pressure outside the cavity, p_c is the pressure inside the cavity, ρ is the fluid density, and U_∞ is the relative speed between the flow and the cavitator center of pressure (c.p). Supercavitation is achieved for cavitation numbers below certain threshold, i.e., $\sigma < \sigma_\tau$. The cavitation number can be lowered by either increasing the relative speed between the flow and the cavitator (U_∞) or by decreasing the difference ($p_\infty - p_c$). Blowing air near the nose of the vehicle increases p_c and allows the formation of ventilated supercavities. Ventilated supercavitation is used to form supercavities at low speeds until reaching natural supercavitation at higher speeds.

2.2 HSSV Description

The assumed HSSV architecture in this thesis consists of a cylindrical body, a disk cavitator with one degree of freedom, and two wedge fins with one degree of freedom and connected to a servo-motor through the same axle. Furthermore, this thesis focuses only on the longitudinal plane of the vehicle. A schematic of the vehicle is shown in Figure 2.1.

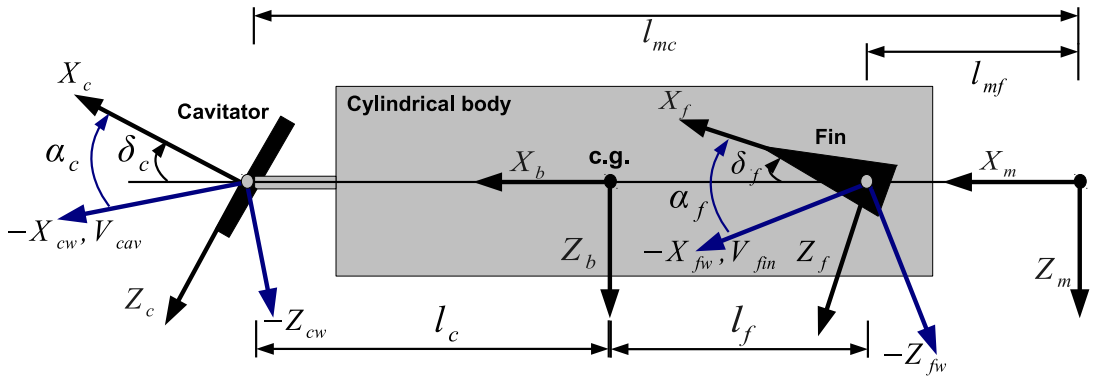

Figure 2.1: HSSV and coordinate frames

2.2.1 HSSV - Coordinate frames and angles

The coordinate frames used for the HSSV analysis, depicted in Figure 2.1, are described as follows.

- Cavitator frame (X_c, Y_c, Z_c): Attached to the cavitator control surface, its X_c axis forms an angle δ_c with the centerline of the HSSV body. δ_c is referred to as cavitator deflection. This angle is positive in the clockwise direction.
- Cavitator wind frame (X_{cw}, Y_{cw}, Z_{cw}): Attached to the cavitator c.p. velocity vector. $-X_{cw}$ axis forms an angle α_c with X_c. α_c is referred to as cavitator angle of attack. This angle is positive in the clockwise direction.
- Fin frame (X_f, Y_f, Z_f): Attached to the fin control surfaces, its X_f axis forms an angle δ_f with the centerline of the HSSV body. δ_f is referred to as fin deflection. This angle is positive in the clockwise direction.
- Fin wind frame (X_{fw}, Y_{fw}, Z_{fw}): Attached to the fin c.p. velocity vector. $-X_{fw}$ axis forms an angle α_f with X_f. α_f is referred to as fin angle of attack. This angle is positive in the clockwise direction.
- Body frame (X_b, Y_b, Z_b): Attached to HSSV body center of gravity (c.g.), the X_b axis is tied to the body's centerline.
- Measurement frame (X_m, Y_m, Z_m): In this frame, the forces and moments are measured. The center of this frame is the point for which a force in the Z_m direction produces zero torque about Y_m.

2.2.2 HSSV Longitudinal Equations of Motion

The generalized longitudinal equations of motion of a HSSV are given in equations 2.2, 2.3, and 2.4.

$$m(\dot{u} + qw) = \sum F_x = F_{x_{fins}} + F_{x_{cav}} + F_{x_{planing}} + F_{x_g} + F_{x_{dist}} + F_{x_{thrust}} \tag{2.2}$$

$$m(\dot{w} - qu) = \sum F_z = F_{z_{fins}} + F_{z_{cav}} + F_{z_{planing}} + F_{z_g} + F_{z_{dist}} \tag{2.3}$$

$$I_{yy}\dot{q} = \sum M_y = M_{y_{fins}} + M_{y_{cav}} + M_{y_{planing}} + M_{y_{dist}} \tag{2.4}$$

$\dot{q}$ is the angular acceleration about the Y_b axis; u and w are the velocities in the X_b and Z_b directions respectively; m is the mass of the vehicle; I_{yy} is the moment of inertia about Y_b; $F_{x_{cav}}$, $F_{z_{cav}}$, and $M_{y_{cav}}$ are the forces and pitch moment generated by the cavitator; $F_{x_{fins}}$, $F_{z_{fins}}$, and $M_{y_{fins}}$ are the forces and pitch moment generated by the fins; $F_{x_{planing}}$, $F_{z_{planing}}$, and $M_{y_{planing}}$ are the forces and pitch moment generated by planing; $F_{x_{thrust}}$ is the force generated by the thrust; and $F_{x_{dist}}$, $F_{z_{dist}}$, and $M_{y_{dist}}$ are the forces and pitch moment generated by external disturbances (perturbed flow). Note that the forces are described in the body frame.

2.3 Cavitator Forces

The cavitator surface is always in contact with the fluid and partially responsible for the drag developed by the HSSV. This control surface rotates about a pivot located at a distance L_c from the HSSV's center of gravity (c.g.). This rotation is denoted by δc, which is positive in the clockwise direction. In this thesis the cavitator is assumed to be a disk of diameter d_c and area $A_c = \frac{1}{4}\pi d_c^2$. Figure 2.2 shows a picture of a disk cavitator with the velocity of the center of pressure (V_{cav}) and the coordinate frames.

The tangential hydrodynamic forces acting on the surface of a disk cavitator are negligible; therefore, the only significant force is assumed to be normal to the cavitator surface and applied at the center of pressure (geometric center of the disk). The net force normal to the cavitator is $F_{cav} = \frac{1}{2}\rho||V_{cav}||^2 A_c C_{D0}(1+\sigma)\cos(\alpha_c)$ [11]. Equations 2.5 and 2.6, proposed by Logvinovich [11], describe the drag and lift forces respectively. These forces are the projection of the cavitator net force (F_{cav}) on the cavitator wind axes (X_{cw}, Z_{cw}) depicted in Figure 2.2. Expressions 2.5 and 2.6 hold for angles between -45 and 45 degrees. The drag force is parallel to the velocity at the cavitator center of pressure, whereas the lift force is normal to the drag.

$$D_c = \frac{1}{2}\rho||V_{cav}||^2 A_c C_{D0}(1+\sigma)\cos^2(\alpha_c) \tag{2.5}$$

$$L_c = -\frac{1}{2}\rho||V_{cav}||^2 A_c C_{D0}(1+\sigma)\cos(\alpha_c)\sin(\alpha_c) \tag{2.6}$$

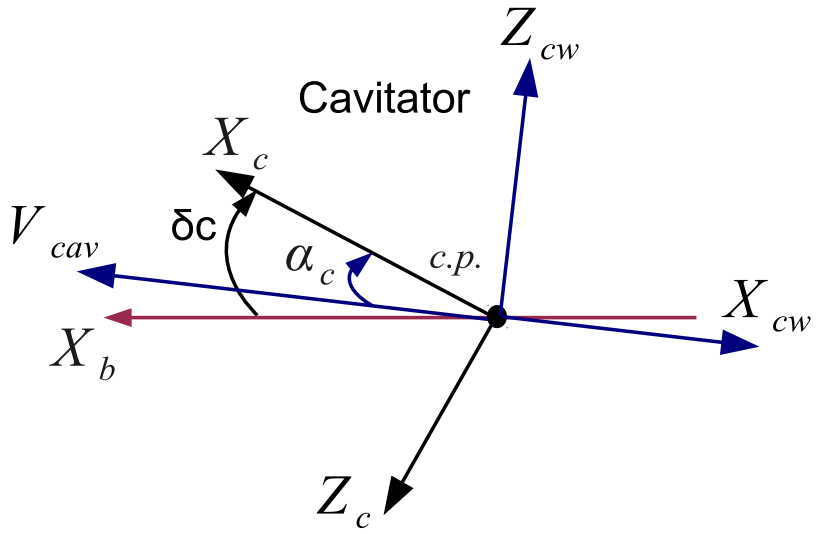

Figure 2.2: Cavitator diagram

C_{D0} is a constant with an approximate value of 0.815 [13]. Notice that a positive cavitator angle of attack produces negative lift, which points down in the wind axes. The cavitator coefficients of drag (C_{CD}) and lift (C_{CL}) are given in equations 2.7 and 2.8.

$$C_{CD} = \frac{D_c}{\frac{1}{2}\rho||V_{cav}||^2 A_c} = C_{D0}(1+\sigma)\cos^2(\alpha_c) = C_x \cos^2(\alpha_c) \tag{2.7}$$

$$C_{CL} = \frac{L_c}{\frac{1}{2}\rho||V_{cav}||^2 A_c} = -C_{D0}(1+\sigma)\cos(\alpha_c)\sin(\alpha_c) = -C_x \cos(\alpha_c)\sin(\alpha_c) \tag{2.8}$$

The resulting hydrodynamic forces act at the center of pressure; hence, the net moment about it is equal to zero, that is, ($C_{CM} = 0$).

Since the cavitator is in motion together with the HSSV, the cavitator velocity (V_{cav}) and cavitator angle of attack (α_c) are derived as a function of the vehicle states. The velocity of the cavitator center of pressure (V_{cav}), expressed in the body frame, is given in equation 2.9.

$$V_{cav} = V_{cg} + \Omega \times \vec{r}_{cav} \tag{2.9}$$

$V_{cg} = [u, 0, w]^T$ is the velocity of the vehicle's center of gravity in the body axes, $\Omega = [0, q, 0]^T$ is the angular velocity of the vehicle, and $r_{cav} = [l_c, 0, 0]^T$ is the position of the cavitator center of pressure with respect the vehicle's center of gravity assuming that the cavitator is aligned with the X_b axis. $(\times)$ is the cross product operator. Equation 2.9 is then rewritten as 2.10. The cavitator angle of attack α_c is given in expression 2.11.

$$V_{cav} = \begin{bmatrix} u \\ 0 \\ w - l_c q \end{bmatrix} \tag{2.10}$$

$$\alpha_c = tan^{-1}\left(\frac{w - l_c q}{u}\right) + \delta_c \tag{2.11}$$

The drag and lift forces expressed in the body axes are presented in equations 2.12 and 2.13. These forces are obtained through coordinate transformations of the forces expressed in the cavitator wind frame and given in equations 2.5 and 2.6.

$$F_{x_{cav}} = -\frac{1}{2}\rho||V_{cav}||^2 A_c C_{D0}(1+\sigma)\cos(\alpha_c)\cos(\delta_c) \tag{2.12}$$

$$F_{z_{cav}} = \frac{1}{2}\rho||V_{cav}||^2 A_c C_{D0}(1+\sigma)\cos(\alpha_c)\sin(\delta_c) \tag{2.13}$$

The moment respect the vehicle c.g. generated by the cavitator is given in equation 2.14.

$$M_{y_{cav}} = -F_{z_{cav}} l_c \tag{2.14}$$

For small angles α_c and δ_c, expressions 2.12 and 2.13 can be approximated by 2.15 and 2.16 respectively.

$$F_{x_{cav}} \approx -\frac{1}{2}\rho||V_{cav}||^2 A_c C_{D0}(1+\sigma) \tag{2.15}$$

$$F_{z_{cav}} \approx \frac{1}{2}\rho||V_{cav}||^2 A_c C_{D0}(1+\sigma)\delta_c \tag{2.16}$$

Equations 2.16 and 2.16 suggest that for small angles of attack and cavitator deflections the drag force does not vary and the lift force mostly depend on only the cavitator deflection respect the body frame.

2.4 Fin Forces

The fins are control surfaces that stabilize the vehicle and provide lift for trimming. They are located near the tail of the vehicle and can be used to control the HSSV dynamics. Wedge swept fins with span b, chord c, fin area $S_f = bc$, wedge angle β_f, and sweep angle θ_f are considered in this thesis. Figure 2.3 shows a schematic of a wedged fin.

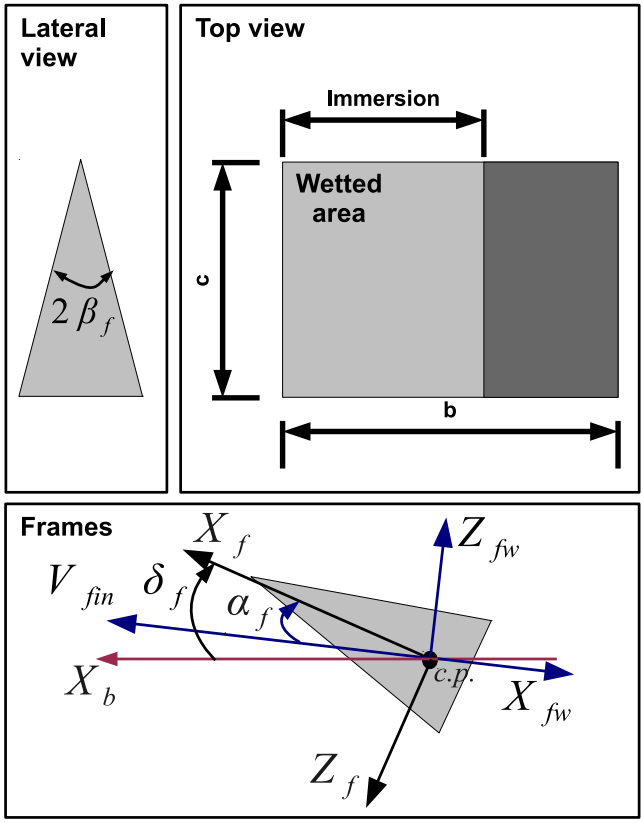

Figure 2.3: Fin diagram

A fin piercing the main supercavity of a HSSV can operate in three regimes; first, the fin can be partially wetted at small angles of attack for which the slope of the fin angle of attack versus lift is maximum (regime I); second, the fins can develop partial supercavities at intermediate angles of attack for which the slope of the fin angle of attack versus lift is lower than the previous case (regime II); finally, for higher angles of attack the fins can be fully enveloped by a supercavity (regime III), this results in zero lift [14].

Fin immersion (I_{fin}) and hence the wetted area of the fin (S_{f0}) vary according to the fin position relative to the bubble. Thus, the drag and lift forces applied to the fin along X_{fw} and Z_{fw} respectively, depend upon the wetted area (immersion), fin angle of attack (α_f), and regime. Experimental and simulation studies ([14] , [5]) have shown that the lift curves as a function of small angles of attack and for different immersions follow a linear behavior with different slopes associated to the regime. The drag and lift forces generated by the fin are given in expressions 2.17 and 2.18 respectively.

$$D_{fin} = \frac{1}{2}\rho||V_{fin}||^2 S_f C_{FD}(\alpha_{fin}, I_{fin}) \tag{2.17}$$

$$L_{fin} = \frac{1}{2}\rho||V_{fin}||^2 S_f C_{FL}(\alpha_{fin}, I_{fin}) \tag{2.18}$$

$C_{FD}(\alpha_{fin}, I_{fin})$ and $C_{FL}(\alpha_{fin}, I_{fin})$ are the fin coefficients of drag and lift respectively. These coefficents are derived in Chapter 4 based on experiments presented in Chapter 3. It is assumed that the moment about Y_f is negligible ($M_{y_{fin}} = 0$).

Since the fin is in motion together with the HSSV, the fin velocity (V_{fin}) and fin angle of attack (α_f) are derived as a function of the vehicle states. In addition, the fin forces are expressed in the HSSV body frame on which the equations of motion are written. The velocity of the fin center of pressure (V_{fin}), expressed in the body frame, is given in equation 2.19.

$$V_{fin} = V_{cg} + \Omega \times \vec{r}_{fin} \tag{2.19}$$

$\vec{r}_{fin} = [-l_f, 0, 0]^T$ is the position of the fin center of pressure respect the vehicle's center of gravity. Equation 2.19 leads to equation 2.20. The fin angle of attack is

presented in expression 2.21.

$$V_{fin} = \begin{bmatrix} u \\ 0 \\ w + l_f q \end{bmatrix} \tag{2.20}$$

$$\alpha_f = tan^{-1}\left(\frac{w + l_f q}{u}\right) + \delta_f \tag{2.21}$$

The fin forces expressed in the body axes and in vector form are given in equation 2.22. Note that $\theta_V^b = \alpha_f - \delta_f = tan^{-1}\left(\frac{w+l_f q}{u}\right)$ is the angle between the V_{fin} vector and the X_b axis. The moment respect the vehicle c.g. generated by the fins ($M_{y_{fin}}$) is given in equation 2.23.

$$\begin{bmatrix} F_{x_{fins}} \\ F_{z_{fins}} \end{bmatrix} = \begin{bmatrix} cos(\theta_V^b) & -sin(\theta_V^b) \\ sin(\theta_V^b) & cos(\theta_V^b) \end{bmatrix} \begin{bmatrix} -D_{fins} \\ -L_{fins} \end{bmatrix} \tag{2.22}$$

$$M_{y_{fin}} = F_{z_{fin}} l_f \tag{2.23}$$

2.5 Planing Forces

The planing force, generated when the vehicle pierces the supercavity, is a high amplitude force that pushes the vehicle toward the interior of the bubble. Models of planing force have been proposed by Logvinovich ([11]) and Paryshev ([15]). These models are explored and related to the vehicle dynamics and controls in [1]. These models are not presented because this thesis is focused on non-planing supercavitating vehicle. Nevertheless, an initial view to the experimental generation of planing in the SAFL high speed water tunnel is presented in Chapters 3 and 4. Figure 2.4 shows the test vehicle used in this thesis when planing is generated.

2.6 Perturbed Flow

Waves on the sea surface and ocean currents disturb the motion of underwater vehicles traveling under the sea surface. The effect of waves is most prominent near the sea surface and negligible in the ocean depth [16], [17]. The effect of sea conditions can

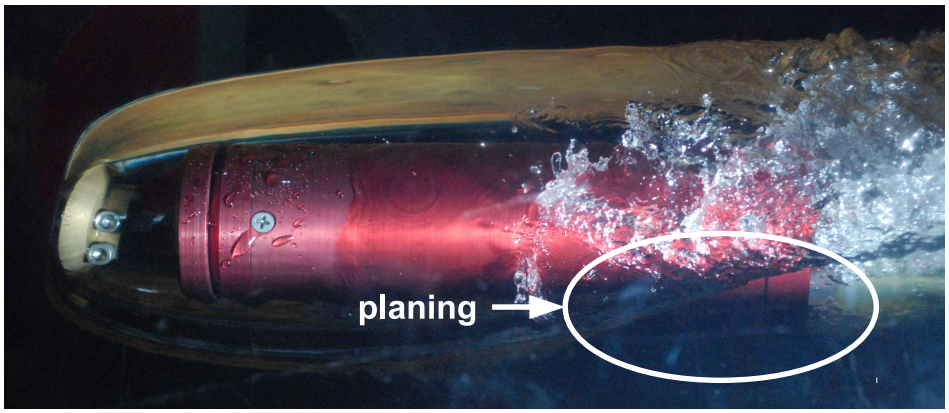

Figure 2.4: Planing in CoSCIS-3 at SAFL, University of Minnesota

be scaled to experiments in a high speed water tunnel; for instance, the investigation presented in [18] addressed this problem by using the SAFL high speed water tunnel and an oscillating foil gust generator.

For supercavitating vehicles, qualitative and quantitative analysis of the effect of perturbed flow on the HSSV motion could not be found in the open literature. A supercavitating vehicle traveling near the ocean surface suffers perturbations in the motion due to the waves on the surface. The main effect is the variation of the angle of attack felt by the wetted portions of the HSSV body. Variations in the angle of attack produce force variations that perturb the HSSV motion and deformations of the supercavity that also impact the hydrodynamic forces acting on the HSSV. An initial experimental view of this topic is presented in this thesis.

2.7 Supercavity Description

The HSSV dynamics is highly coupled with the supercavity kinematics because the fin immersion and planing are function of the location of the bubble with respect to the vehicle body. For this reason a brief description of the supercavity is given in this section. These concepts also enable the experimental generation of planing for research purposes as is done in Section 3.2.5. Figure 2.5 shows a schematic of the supercavity in which the parameters that describe the bubble geometry are depicted.

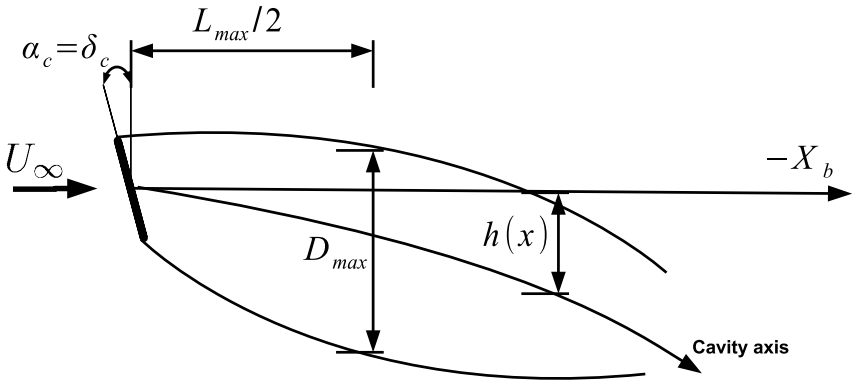

Figure 2.5: Schematic of supercavity

Mathematical descriptions of the geometry parameters shown in Figure 2.5 are presented by Logvinovich [11]. The maximum diameter (D_{max}), half cavity length ($L_{max}/2$), cavity deformation ($h(x)$) are given in equations 2.24, 2.25, 2.26 respectively.

$$D_{max} = d_{cav}\sqrt{\frac{C_{D0}(1+\sigma)}{\sigma}} \tag{2.24}$$

$$L_{max} = \frac{d_{cav}}{2}\left(\frac{1.92}{\sigma} - 3\right) \tag{2.25}$$

$$h(x) = -\frac{C_{CL}}{\pi}\int_0^{X_s}\frac{dx}{R^2(x)} = \frac{1}{\pi}C_{D0}(1+\sigma)cos(\alpha_c)sin(\alpha_c)\int_0^{X_s}\frac{dx}{R^2(x)} \tag{2.26}$$

Notice that the dimensions of the bubble described by D_{max} and L_{max} only depend on the cavitation number and the cavitator diameter. Equation 2.26 is considered in the cavitator wind axes; hence, positive cavitator angles of attack produce upward displacements ($h(x)$) of the cavity axis.

For a static vehicle attached to axis X_b, it is possible to generate planing by either decreasing the diameter of the cavity sections or displacing the cavity axis. The cavity axis displacement ($h(s)$) is function of the cavitator angle of attack that can be varied via cavitator actuation or variations in the fluid direction respect to the cavitator. This result is used in Section 3.2.5 for generating planing.

Chapter 3

Model Validation Methods

This chapter is focused on the experimental infrastructure and experiments conducted to validate and derive models of the HSSV motion and supercavity geometry. The following chapter is divided into two sections. Section 3.1 describes the infrastructure used to track the supercavity motion and acquire data for the modeling of forces acting on a supercavitating test vehicle. Section 3.2 describes experiments conducted to study cavitator and fin forces, effect of perturbed flow on forces applied to the HSSV, effect of cavitator perturbations and perturbed flow on the bubble geometry, and lastly planing forces.

3.1 Experimental Infrastructure

This section describes the hardware and software components of the experimental infrastructure used for the HSSV modeling. First the overall description of the platform is presented; then, the components of the system are described.

3.1.1 Overall Description

Experiments to validate and derive models of the HSSV and supercavity motion can be conducted in the SAFL high speed water tunnel where the Control Surface-Cavity Interaction Simulator (CoSCIS) is placed. The test vehicle uses ventilation to establish the supercavity. The cavitator and fins of the test vehicle are manipulated via a real-time embedded system that is synchronized with a high speed camera to capture the

time evolution of the supercavity geometry. The forces and moments applied to the test vehicle are measured by a six degree of freedom force transducer. The force/moment data is transmitted through analog signals read by a FPGA based device. This device filters and digitally transmit the force/moment data. The position of the gust generator is read and transmitted by this device. The gust generator position and force/moment data is sent to the real-time embedded system via serial communication. The real-time embedded system uses the acquired data from the external devices to execute the water tunnel experiments. The experimental data are transmitted to a host computer where it is displayed and stored for analysis. Figure 3.1 shows a diagram of the infrastructure architecture. The subsystems are described below.

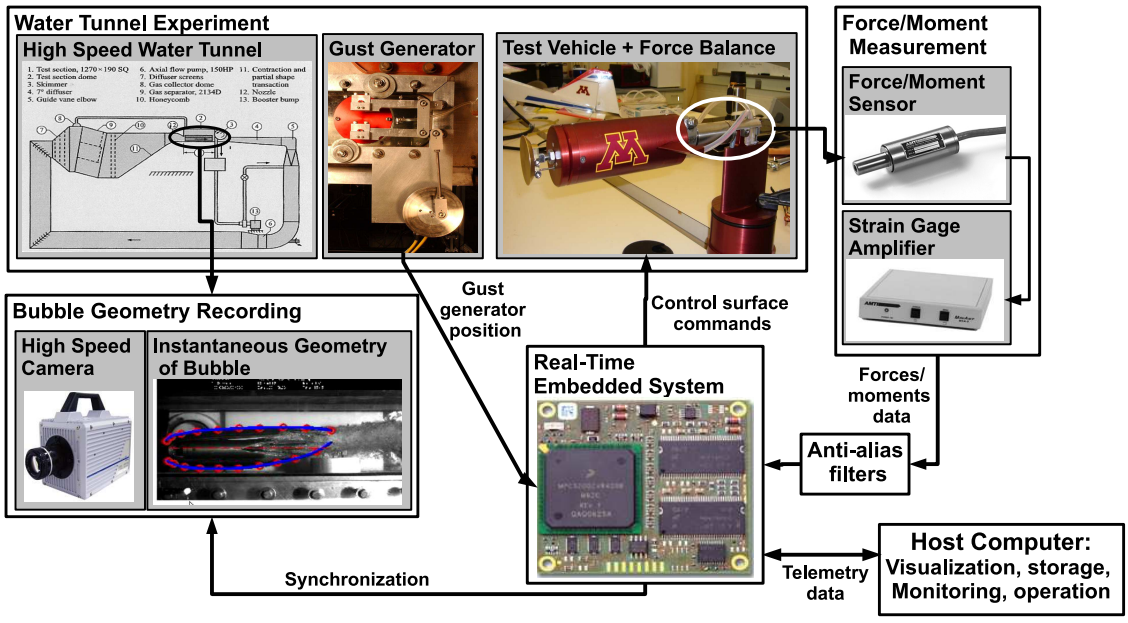

Figure 3.1: Modeling infrastructure architecture

3.1.2 High Speed Water Tunnel

The SAFL high speed water tunnel has the following features [12].

- Recirculating and closed-circuit tunnel
- Regulation of absolute pressure

- Maximum speed of 20 m/s
- It is able to remove large amounts of air during ventilation experiments, this enables the experimentation for long periods of time without saturated water recirculating in the tunnel
- Dimension of the test section is 0.19 m (Width) x 0.19 m (Height) x 1 m (Long)
- Three windows to observe and record experiments

A schematic of the water tunnel at SAFL is shown in Figure 3.2.

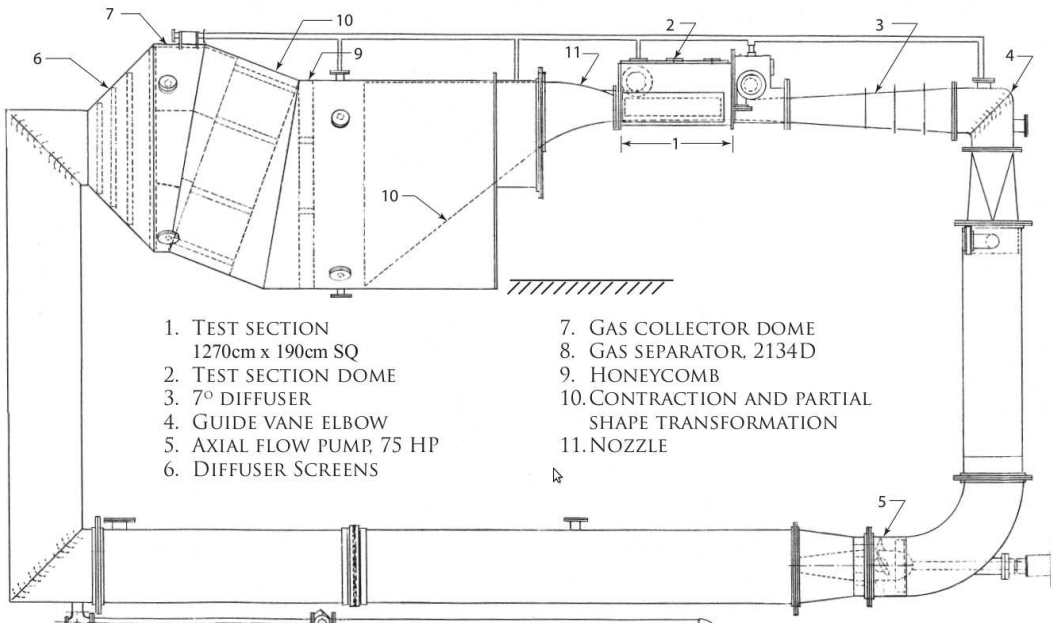

Figure 3.2: Water tunnel at SAFL

The speed of the water tunnel is calibrated via a Laser Doppler Velocimetry (LDV) system. The calibrations need to be carried out for every test vehicle placed in the tunnel.

3.1.3 Control Surface-Cavity Interaction Simulator (CoSCIS-3)

CoSCIS-3 is a test vehicle prototype developed to study the interaction of the supercavity, fluid, and control surfaces as well as emulate vehicle motion in the high speed water

tunnel, as described in Chapter 5. This test system has the following characteristics:

- Water proof cylindrical body with two servo actuators in its interior to deflect the control surfaces. The cylinder has radius 50 mm and length 0.2 m.
- Disk cavitator and two lateral fins whose rotational axle is normal to the longitudinal plane.
- Ventilation supply at the front of the cylinder to form ventilated supercavities.
- Six degree of freedom force/balance transducer.

The control surfaces are controlled through PWM (pulse width modulated) signals sent from a real-time embedded system. A brief description of the control surfaces used in the CoSCIS-3 is given as follows.

CoSCIS-3 Cavitator

A disk cavitator of 40 mm diameter is considered. The control surface is linked to a servo actuator located in the interior of the cylindrical body of the test vehicle. The cavitator is able to rotate +/- 10 degrees about its pivot. The cavitator is at zero angle when the surface of the disk is parallel to the vertical axis of the vehicle's body (Z_b). The distance from the cavitator center of pressure to the measurement frame (force balance transducer) is 0.25 m.

CoSCIS-3 Fins

The fins are 15 degrees half angle wedge-shaped and have a 35 degrees swept. The sweep allows placing the axle at the mean aerodynamic center [19]. The fins have a chord $c = 20$ mm and a height $b = 35$ mm. The fins are able to rotate +/-10 degrees about their common axle. The distance from the fin center of pressure to the measurement frame is 80 mm.

Force/Moment Measurement Unit

The forces and moments are measured using an underwater multi-axes force/moment transducer (AMTI MC1-6 500). This transducer has six channels of outputs (F_{X_m}, F_{Y_m},

F_{Z_m}, M_{X_m}, M_{Y_m}, M_{Z_m}) and is fabricated with stainless steel. The maximum load in the axial, transversal, and vertical directions (F_{X_m}, F_{Y_m} , F_{Z_m}) are 2200 N, 1100 N and 1100 N respectively. The maximum torque loads for the moments about the axial, transversal, and vertical directions (M_{X_m}, M_{Y_m}, M_{Z_m}) are all equal to 1.1 $N \cdot m$. The forces are measured with respect to the measurement frame, defined in Section 2.2.1.

The AMTI MSA-6 amplifier is used to amplify and filter analog signals generated by the strain gages of the transducer. This device filters frequencies beyond 1KHz, outputs analog signals in the range +/- 10 Volts, and transmits force/moment data through serial communication with a resolution per line of 10 bits and a transmission rate of up to 100 samples per second.

The force/moment transducer has several limitations that affect the way in which the experiments are carried out. These limitations are:

- Drifts caused by temperature variations are present in the six measurements, specially in F_{X_m}. When the sensor is submerged in water (lower temperature), force F_{X_m} decreases its value. The drifts for F_{X_m} are of the order of 5 Newtons, which is 1/3 of the the drag developed by the test vehicle at 4.4 m/s. The drifts in all the channels except F_{X_m} can be neglected.

- The measurement range of interest is small in comparison with the full range of the transducer. At 4.4 m/s of water speed the drag and lift forces generated by both cavitator and fins do not exceed 2% of the maximum loads.

- The force transducer does not filter parasite frequencies present in the electric network of the Saint Anthony Falls Laboratory. These frequencies are lower than 1Khz.

The limitations of the force/moment measurement system were overcome throughout the following strategies:

- The analog signals are used instead of the 10 bits data to increase the resolution of the force measurements. The analog signals are sampled by the signal processing device (Section 3.1.5) with a resolution of 16 bits.

- Anti-alias filters are implemented to eliminate the parasite frequencies due to the SAFL electric network. More details are presented in Section 3.1.5.

- The drifts are low frequency components of the signal that can be removed through high pass filters. Hence, experiments to measure forces along X_m need to be performed at frequencies higher than the high-pass filter cut off frequency. For instance, force data resulting from cavitator oscillations at 1 Hz can be filtered with a high pass filter whose cut frequency is 0.1 Hz. Thus, the filtered force data corresponds to the cavitator drag force.

3.1.4 Gust Generator

An oscillating foil system developed for research on low drag partially cavitating hydrofoils is used to study the effect of perturbed flow on the supercavity geometry and forces/moments applied to the test vehicle. Figure 3.3 shows a schematic obtained from [20], which shows the gust generator perturbing the flow that the test vehicle observes.

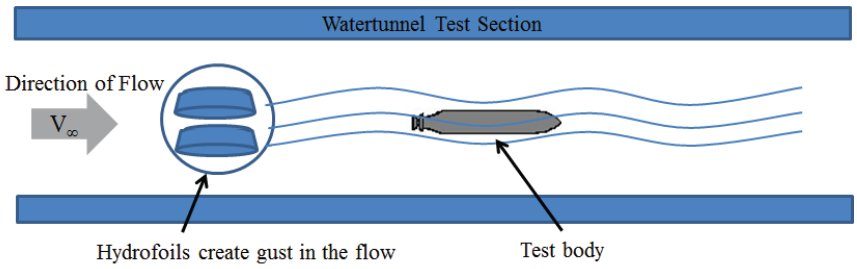

Figure 3.3: Schematic of gust generator perturbing the flow

The disturbance generation system has the ability to create a two dimensional upstream gust with oscillating hydrofoils. Rice [21] provides a baseline for the design of this system. A basic diagram of the oscillating hydrofoil is shown in Figure 3.4. The system design is briefly described in the following paragraph.

Two NACA 0020 hydrofoils are oscillated in phase to provide a uniform gust, which is produced by the pivot arm displacements. The pivot arm is in turn linked to the connecting arm, which is moved by the DC motor rotation. The eccentric wheel provides offsets that allow for 2, 4, 6, 8 and 10 degrees of amplitude in the oscillations. Given the broad range of motor angular speeds (0-3500 RPM) and the flow speeds of the SAFL high speed water tunnel (up to 20 m/s), a wide range of sea unsteady conditions can

be simulated.

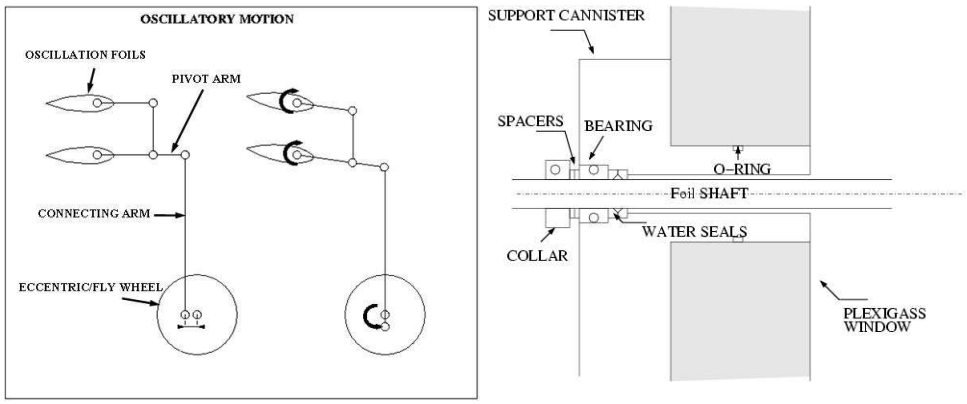

Figure 3.4: Gust generator diagram

The gust system is mounted in the water tunnel, just in front of the test vehicle downstream. Figure 3.5 shows the system mounted in the SAFL high speed water tunnel.

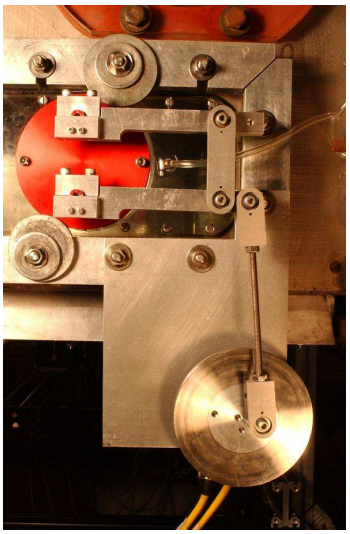

Figure 3.5: Gust generator picture

The DC motor (Parker Automation - BE Series) connected to the gust generator is driven by a drive unit (Aries AR-30xE drive) that controls the angular velocity of the motor's shaft and transmits the angular position of the shaft via an analog signal. The

analog signal is used to track the position of the gust generator during the water tunnel experiments.

3.1.5 Signal Processing Device

The analog sensor signals generated by the Force/Moment transducer-amplifier and the gust generator contain parasite frequencies, which are filtered by using the NI CompactRIO. The CompactRIO is a FPGA based device that samples the signals with 16 bits of resolution at 1.67 KHz and filters frequencies beyond 15 HZ through fourth order Butterworth filters. The filtered signals are transmitted at 40 samples per second via serial communication (RS-232). This device is used as an analog to digital converter with antialias filters.

3.1.6 High Speed Camera

The purpose of the high speed camera is to capture video of water tunnel experiments. The real-time embedded system that executes the experiments, turns on a LED (Light-Emitting Diode) to synchronize the first frame of the video with the overall system. The LED can also be used to trigger additional events. The recorded videos are transformed to images, which are sampled and post processed to obtain the geometry parameters and boundary of the supercavity. The camera used at SAFL is the FASTCAM APX RS, which has a full 1,024 by 1,024 pixel resolution, up to 3,000 fps, 512 by 512 pixels at 10,000 frames per second.

3.1.7 Real-Time Embedded System

The embedded system is loaded with programs that drive the experiments described later in Section 3.2. This system has the following specific functions:

- Drive the control surfaces (cavitator and fins) of the test vehicle (CoSCIS-3) by using PWM (pulse width modulated) signals.
- Acquire force/moment data from the signal processing device as well as the position of the gust generator from the DC motor connected to the oscillating foil.
- Additional filtering of signals if needed.

- Transmit telemetry data to a host computer for visualization and storage

The Phytec MPC5200B-tiny small board computer is the host for the real-time embedded system. This embedded system has the following features: 760 MIPS of processing power, a double precision Floating Point Unit (FPU), On-board memory (flash:16MB, SDRAM:64MB), multiple serial channels, up to three inter-IC sound (IS) interfaces, and support for Ethernet.

eCos (Embedded Configurable Operating System) is an open source real-time operating system used to interface application level programs with the hardware layer. eCos allows a flexible configuration of hardware modules and software level capabilities, eCos also provides a C/C++ tool-chain with POSIX and other standard and non-standardized APIs (application programmer interfaces). This operating system allows the real-time execution of tasks through a single or multiple threads [22]. Variety of hardware and protocols are supported; for example, serial devices; IP, IPv6, UDP and TCP over Ethernet ; PCMCIA; USB; and PCI.

The embedded system executes software developed under the object oriented programming paradigm. The programming language in which the software layers and modules are implemented is C++.

3.1.8 Supervisory Control and Data Acquisition (SCADA) Software

A Java based application was developed to exchange data with the real-time embedded system that runs the water tunnel experiments. This software displays the experimental variables in a friendly graphical user interface (GUI) and stores data in MAT format files (Matlab). In addition, the software functions as a terminal interface to talk with the embedded system bootloader. Figure 3.6 shows a screen shot of this program.

3.2 Experimental Approach

This section describes the experiments conducted to: 1) Construct maps from cavitator and fins angle of attack to cavitator and fin forces respectively; 2) evaluate the effect of the perturbed flow on the forces applied to the test vehicle; 3) evaluate the effect of cavitator deflections and perturbed flow on the supercavity geometry; and 4) initially view the generation of planing forces in the SAFL high speed water tunnel.

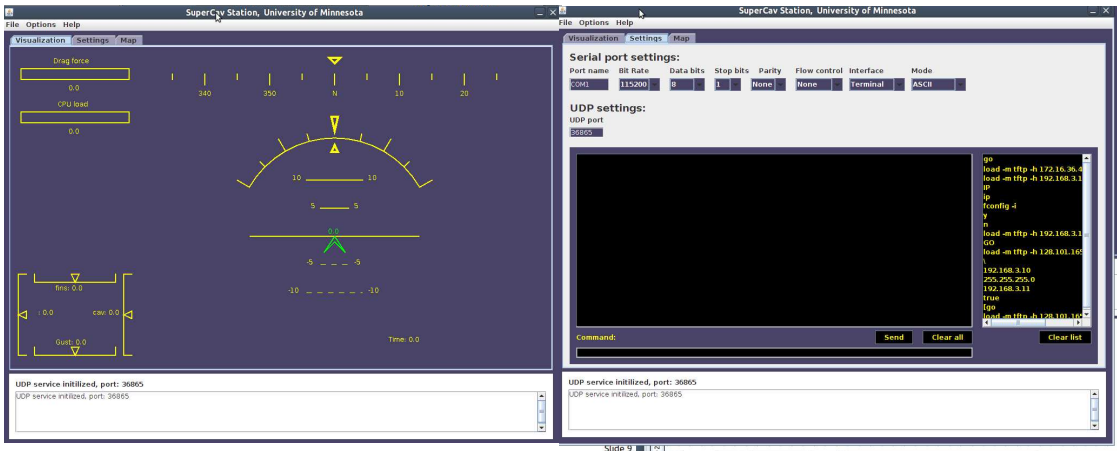

Figure 3.6: Supercav-Station GUI

3.2.1 Cavitator Forces

The acquisition of lift and drag forces generated by the cavitator is performed under the assumption that the fluid velocity is parallel to X_m, which in turn is aligned with X_c when $\delta_c = 0$. Therefore, the cavitator deflection is approximately equal to the cavitator angle of attack, i.e. $\delta_c \approx \alpha_c$. The experiment to acquire the cavitator forces is described as follows: The disk cavitator deflection was commanded with sinusoids of amplitude 9 degrees at different frequencies (0.25, 0.5, 1, and 2 Hz) and the lift and drag force responses were measured. The force measurements were passed through band pass filters that removed drifts, vibrations of the test vehicle, and parasite high frequencies. the filter has as cut off frequencies equal to 0.1 and 6 Hz. Conditions of the experiment are as follows: Water tunnel speed was 4.39 m/s, no fins mounted on the vehicle, and flow rate was 20 liters per minute (lpm).

An experiment in which the fins were mounted on the model was performed to visualize the coupling between cavitator and fins. The fin deflection was set to zero ($\delta_f = 0$), while a sinusoid of 1 Hz and 8 degrees of amplitude was applied to the cavitator deflection. Experimental conditions are as follows: Water tunnel speed was 4.39 m/s, fins were partially wetted with no partial supercavitation (regime I), and flow rate was 20 liters per minute (lpm).

3.2.2 Fin Forces

The acquisition of lift and drag forces generated by the fins is performed under the assumption that the fluid velocity is parallel to X_m, which in turn is aligned with X_f when $\delta_f = 0$. Therefore, the fin deflection is approximately equal to the fin angle of attack, i.e. $\delta_f \approx \alpha_f$. the experiment to acquire the fin forces is described as follows: The fin deflection was commanded with sinusoids of amplitude 7 degrees at different frequencies (0.25, 0.5, 1, and 2 Hz) and the lift and drag force responses were measured and filtered. The filter has as cut off frequencies equal to 0.1 and 6 Hz. The fin immersion (I_{fin}) was not determined because of the complexity of measuring it; hence, I_{fin} is assumed as constant. The conditions for this experiment are as follows: Water tunnel speed was 3.01 m/s, fins were partially wetted with no partial supercavitation (regime I), and flow rate was 20 lpm.

3.2.3 Perturbed Flow

The effect of perturbed flow on the vehicle motion was evaluated by using the gust generator described in Section 3.1.4. The gust generator produces sinusoidal perturbations in the fluid that vary the effective angles of attack at different parts of the vehicle body. Two experiments were developed to evaluate the effect of perturbed flow on the HSSV forces.

Supercavity Isolation

An experiment was executed to evaluate the effect of gust oscillations on the forces observed by the vehicle with and without the supercavity. Forces were measured for two conditions: First, no supercavity enveloping the test vehicle; and second, the supercavity was established. For this experiment, the gust generator ran at 2 Hz with an oscillation amplitude of 6 degrees. Control surface deflections were set to $\delta_f = 0$ and $\delta_c = 0$. Conditions for this experiment are as follows: Water tunnel speed was 3.77 m/s, fins were partially wetted with no partial supercavitation (regime I), and flow rate was 20 lpm. DC and high frequency components of the force measurements were removed through a band pass filter to capture only the response to the gust generator oscillations. The filter has cut off frequencies equal to 0.4 and 6 Hz.

Perturbed Flow with no Fins

An experiment was performed to validate the effect of perturbed flow on the forces applied to the supercavitating test vehicle with no fins mounted. Two scenarios were explored: First, the gust generator ran at 2 Hz and 6 degrees of amplitude; second, the gust generator was turned off. Conditions for this experiment are as follows: Water tunnel speed was 3.77 m/s, and flow rate was 20 lpm. DC and high frequency components of the force measurements were removed through a band pass filter to capture only the response to the gust generator oscillations. The filter has cut off frequencies equal to 0.4 and 6 Hz.

3.2.4 Cavitator Angle of Attack and Supercavity Geometry

The gust generator and cavitator deflections vary the cavitator angle of attack (α_c), which in turn produces a deformation ($h(x, \alpha_c)$) of the supercavity axis (equation 2.26). This deformation results in vertical displacements of the bubble transversal sections as discussed in Section 2.7.

An experiment was performed to visualize the bubble deformation for different cavitator angles of attack. The cavitator was driven with a train of pulses with period equal to 3 seconds and whose maximum and minimum values were +9 and -9 degrees respectively. In this experiment the fins were not mounted on the vehicle.

A second experiment was performed to observe the the variations in the supercavity geometry as a result of oscillations of the gust generator and oscillations of both the gust generator and cavitator. This experiment is described as follows: A sinusoid of frequency f_{gust} and amplitude A_{gust} was commanded to the gust generator $\delta_g(t) = A_{gust}\sin(2\pi f_{gust}t)$. Then a shifted signal of the form $\delta_c = -\frac{A_{cav}}{A_{gust}}\delta_g(t)$ was applied to the cavitator deflection. Notice that δ_g was accessible by the embedded system. In this experiment the fins were mounted on the vehicle. The geometric parameters of the supercavity to be evaluated are the supercavity axis deformation ($h(x)$) at $x = L_{max}/2$), distance to section with maximum diameter ($L_{max}/2$), and maximum diameter of the supercavity sections (D_{max}). These geometric parameters are described in Section 2.7. The time evolution of the bubble geometry is recorded and video is synchronized with the embedded system. The video frames are sampled at 5 Hz and processed to obtain

the geometric parameters of the supercavity ($h(x = L_{max})$, L_{max} and D_{max}). The conditions for both experiments are as follows: Water tunnel speed was 3.01 m/s and flow rate was 20 lpm.

3.2.5 Planing Forces

Planing forces can be generated by deflecting the cavity axis of the bubble such that the test vehicle pierces the main supercavity. The cavity axis deformation is function of the cavitator angle of attack [11], as discussed in Section 2.7. The cavitator angle of attack varies as a function of the cavitator deflection δ_c and perturbed flow. Adding the effect of perturbed flow to the maximum cavitator deflection it is possible to achieve cavitator angles of attack and bubble displacements such that planing is reached.

An experiment to generate dynamic planing forces was performed. The cavitator deflection was set to $\delta_c = 10^o$ while was the gust generator deflection oscillated at 1 Hz. Planing forces $F_{x_{planing}}$ and $F_{z_{planing}}$ were considered in the body frame. Conditions for the experiment are as follows: Water tunnel speed was 3.01 m/s, no fins mounted on the vehicle, and flow rate was 20 lpm.

Chapter 4

Model Validation Results

The main objective of this chapter is the derivation of the non-planing HSSV equations of motion in the longitudinal plane, which are used in Chapter 5 to implement a control validation infrastructure and design a control law for the vehicle motion. This chapter presents mathematical force models of the cavitator, fins, and perturbed flow based on results of experiments described in Chapter 3. The HSSV longitudinal equations of motion are derived based on these force models. Moreover, planing forces and the effect of cavitator deflections and perturbed flow on the bubble geometry are initially discussed. A description of each section in this chapter is as follows: Section 4.1.1 presents mathematical expressions of the cavitator forces that are compared with the Logvinovich models described in Section 2.3. Simple mathematical expressions of the fin forces are derived in Section 4.1.2. The perturbed flow effect on the forces applied to the HSSV is discussed in Section 4.1.3. Planing forces generated as described in Section 3.2.5 are initially viewed in Section 4.1.5. Section 4.2 presents the HSSV nonlinear and linear equations of motion as well as the simulation of the HSSV motion subject to perturbations to the control surface deflections (cavitator and fins). These simulations show the stability characteristics and transient response of the vehicle.

4.1 Model Validation Experimental Results

4.1.1 Cavitator Forces

The cavitator force measurements from experiments described in Section 3.2 are normalized via equations 2.7 and 2.8 to obtain the coefficients of drag and lift respectively. The lift coefficient (C_{CL}) and cavitator angle of attack ($\alpha_c \approx \delta_c$) are fitted to a line via least squares polynomial fitting. The coefficient of lift is found to follow $C_{CL} = \frac{\partial C_{CL}}{\partial \alpha_c}\alpha_c = -0.9961\alpha_c$. By using the previous result, equation 2.8, and approximation given in expression 4.1 the cavitation number is found to be $\sigma = 0.27$. For the test platform used in this research, the cavitation number (σ) is unavailable via pressure measurements; therefore, the use of lift measurements is the way in which it is calculated.

$$C_{CL} = -C_{D0}(1+\sigma)\cos(\alpha_c)\sin(\alpha_c) \approx -C_{D0}(1+\sigma)\alpha_c \approx -0.9961\alpha_c \tag{4.1}$$

The cavitator lift force can be calculated using the Logvinovich model described in Section 2.3 and cavitation number (σ). This model is compared in Figures 4.1 and 4.2 with the experimental lift data and linear approximation. The experimental lift coefficient (C_{CL}) data versus cavitator angle of attack (α_c) are compared in Figure 4.1 with the Logvinovich and linear models of lift given in expressions 2.8 and 4.1 respectively. The time evolution of the experimental lift data given $\alpha_c(t) \approx \delta_c(t) = 8sin(2\pi t)$ [deg] is compared in Figure 4.4 with the Logvinovich and linear models of lift. Figures 4.1 and 4.2 show that the lift forces given by the experimental data, Logvinovich model, and linear approximation have good agreement for the considered values of cavitator angle of attack.

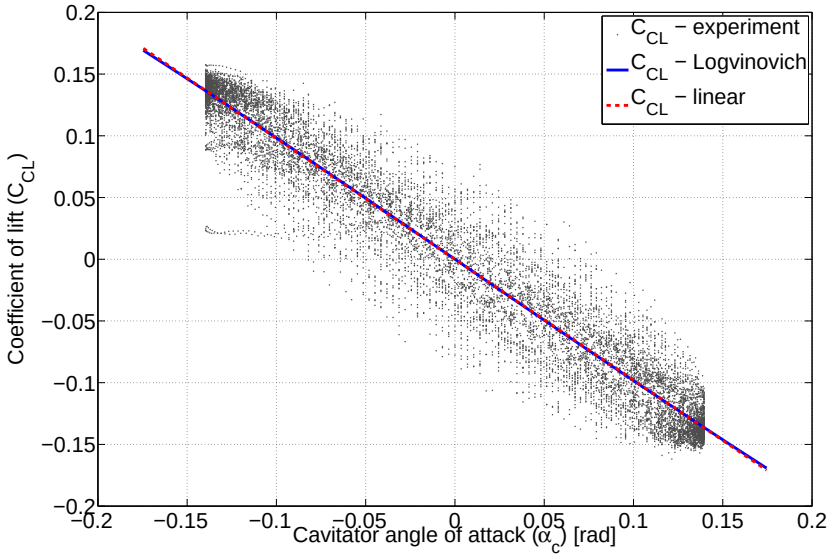

Figure 4.1: Cavitator lift coefficient Vs. cavitator angle of attack

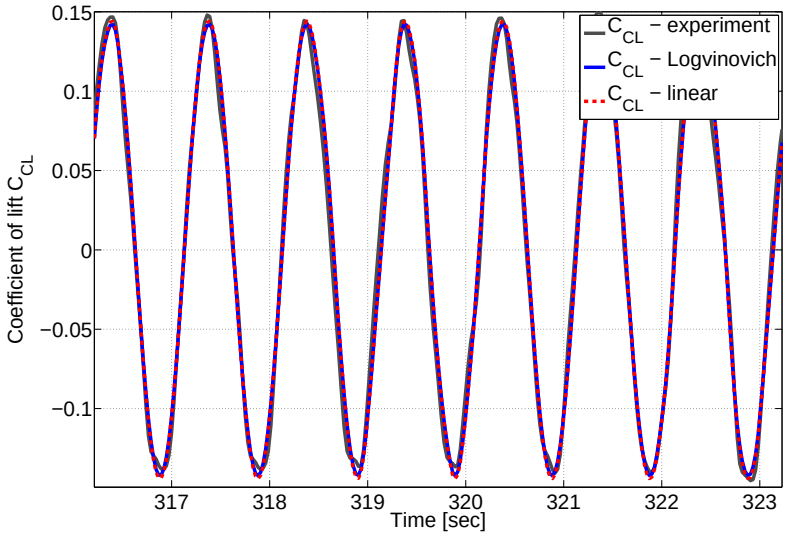

Figure 4.2: Time domain validation of cavitator lift coefficient (C_{CL})

Offsets in the test vehicle positioning lead to biases of the cavitator angle of attack,

that is, for $\delta_c = 0$ the cavitator angle of attack is not exactly zero, instead it is $\alpha_c \approx \Delta\alpha_c$. This offset does not impact the computation of $\frac{\partial C_{CL}}{\partial \alpha_c}$ because of the DC component of the lift is removed with the band pass filter. However, the offset in the vehicle positioning has the effect of translating the drag curve by $\Delta\alpha_c$ in the α_c axis. This translation needs to be removed to obtain an accurate model of drag force. Furthermore, the band pass filter applied to the drag data removes the value of drag at zero angle of attack. The drag force at zero cavitator angle of attack can not be accurately extracted from the non-filtered measurements; hence, the drag at zero angle of attack given by Logvinovich ($C_{D0}(1+\sigma)$) is assumed.

The filtered and normalized drag measurements that include the offset positioning effect are fitted using a second order polynomial of the form $C_{CD_{off}} \approx a_{cd}\alpha_c^2 + b_{cd}\alpha_c + c_{cd}$. The maximum of this curve is equal to $C_{CD}^0 = -b_{cd}^2/(4a_{cd}) + c_{cd}$ and it is located at $\Delta\alpha_c = \frac{-b_{cd}}{2a_{cd}}$, that is, the offset in the vehicle positioning. If the curve is horizontally displaced by $\Delta\alpha_c$ and vertically displaced by C_{CD}^0, then the resulting curve is $C_{CD} \approx a_{cd}\alpha_c^2$. This curve is the drag coefficient, with zero drag at zero angle of attack.

The drag coefficient, considering the value of drag at zero angle of attack, can be modeled by adding $C_{D0}(1+\sigma)$ (Logvinovich) to the quadratic form. This description of the cavitator drag coefficient, given in expression 4.2, captures the variational effect of α_c on C_{CD} as well as the value of drag at zero angle of attack.

$$C_{CD} = C_{D0}(1+\sigma) + a_{cd}\alpha_c^2 = C_{D0}(1+\sigma) - 1.1608\alpha_c^2 \tag{4.2}$$

The cavitator drag force can be also calculated using the Logvinovich model of drag described in Section 2.3 and cavitation number (σ) computed from the lift data. This model is compared in Figures 4.3 and 4.4 with the experimental drag data and the quadratic approximation. The experimental drag coefficient (C_{CD}) data versus cavitator angle of attack (α_c) are compared in Figure 4.3 with the Logvinovich and quadratic models of drag given in expressions 2.7 and 4.2 respectively. The measured drag coefficient is translated to match with the logvinovich and quadratic models of drag, that is, the filtered drag data is added with $C_{D0}(1+\sigma) - C_{CD}^0$ and translated by $-\Delta\alpha_c$ in the α_c axis. The experimental data dispersion in Figure 4.3 is result of the resolution of the force transducer in the axial direction. The time evolution of the experimental drag data, given $\alpha_c(t) \approx \delta_c(t) = 8sin(2\pi t)$ [deg], is compared in

Figure 4.4 with the Logvinovich and quadratic models of drag. The quadratic model ($C_{CD_{off}} \approx a_{cd}\alpha_c^2 + b_{cd}\alpha_c + c_{cd}$) includes the positioning offset as well as the filtering effect since it is fitted with the filtered drag measurements. The drag curve given by the Logvinovich model is translated by $\Delta\alpha_c$ in the α_c axis and filtered with the same band pass filter used for the measurements, that is, $C_{D0}(1+\sigma)\cos^2(\alpha_c + \Delta\alpha_c(t))$ passed through the band pass filter described in Section 3.2.1. Figures 4.3 and 4.4 show agreement between the drag force data and the Logvinovich and quadratic models of drag.

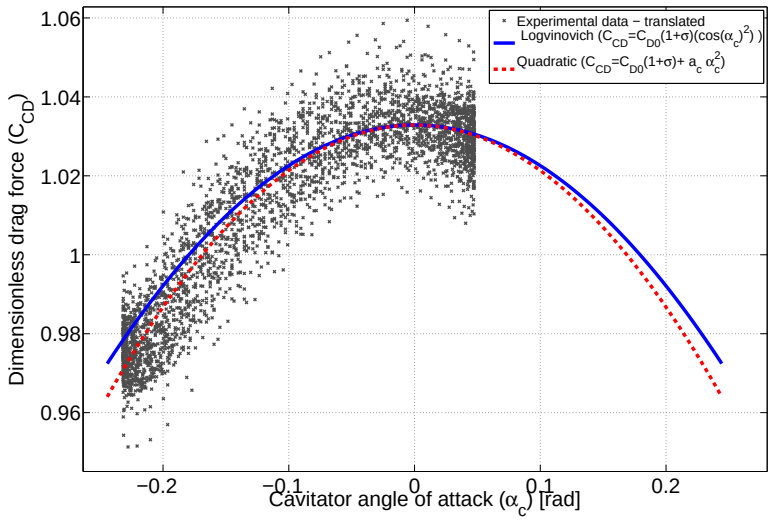

Figure 4.3: Cavitator drag coefficient versus cavitator angle of attack

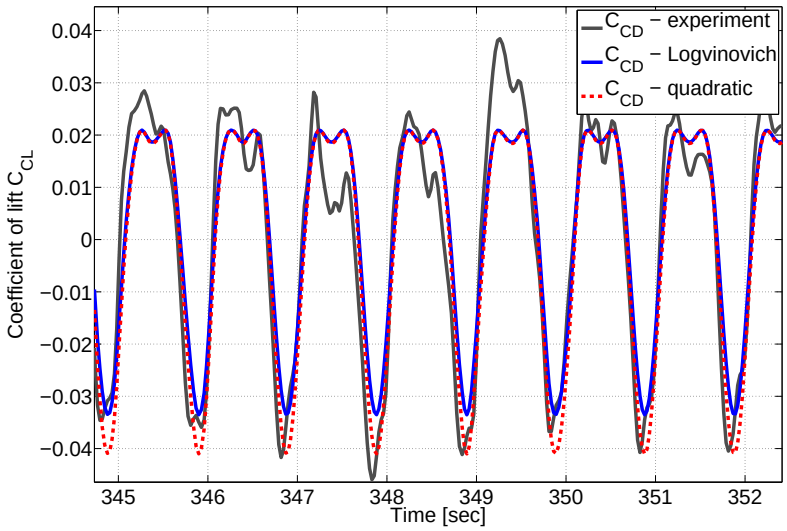

Figure 4.4: Time domain validation of cavitator drag coefficient (C_{CD})

Although the measurements of lift and drag forces agree with the Logvinovich, linear and quadratic forms; the Logvinovich models have an explicit value of the cavitation number. For this reason, the Logvinovich expressions of lift and drag (2.8 and 2.7) are used in the dynamical modeling of the vehicle. The linear and quadratic models are used to calculate the value of the cavitation number (σ) and vehicle positioning offset ($\Delta\alpha_c$).

For the experiment in which the fins were mounted on the test vehicle (described in Section 3.2.1), the slope of the curve C_{CL} versus α_c is $\frac{\partial C_{CL}}{\partial \alpha_c} = -0.9010$, which is smaller than the slope with no fins mounted on the vehicle. This result suggests that the fin forces and angle of attack vary as a function of the cavitator angle of attack. Further analysis is required to explain this phenomenon.

4.1.2 Fin Forces

The fin force measurements from the experiment described in Section 3.2 are normalized via equations 2.17 and 2.18 to obtain the fin coefficients of drag and lift respectively. Notice that the coefficients of lift and drag include the forces of the two lateral fins mounted on the test vehicle. The lift coefficient (C_{FL}) and fin angle of attack ($\alpha_f \approx \delta_f$)

are fitted to a line via least squares polynomial fitting. The coefficient of lift is found to follow expression 4.3.

$$C_{FL} = \frac{\partial C_{FL}}{\partial \alpha_f}\alpha_f = 4.8487\alpha_f \tag{4.3}$$

Figure 4.5 shows the experimental data of C_{FL} versus α_f and the linear approximation of C_{FL} as a function of α_f. The time evolution of C_{FL}, given an input of the form $\alpha_f(t) \approx \delta_f(t) = 7sin(2\pi t)$ [deg] is shown in Figure 4.6.

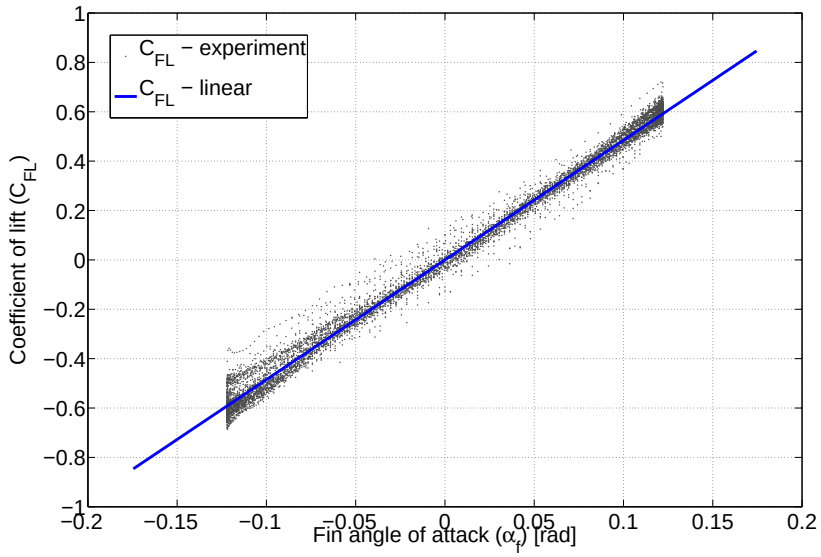

Figure 4.5: Fin lift coefficient Vs. fin angle of attack

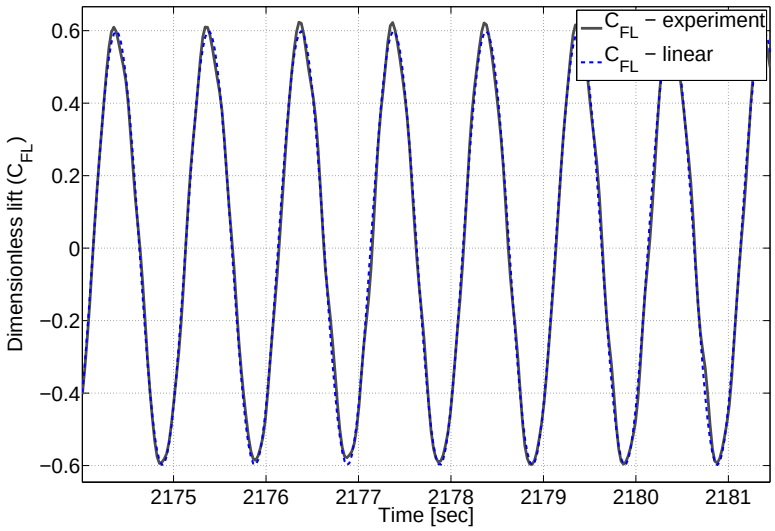

Figure 4.6: Time domain validation of fin lift coefficient (C_{FL})

The offsets in the test vehicle positioning lead to biases of the fin angle of attack ($\Delta\alpha_f$), which translate the drag curve along the α_f axis as in the cavitator case. These offsets need to be removed to accurately describe the variational effect of the fins on the drag force.

The filtered and normalized drag data (experiment described in 3.2), including effect of positioning offset, are fitted to a second order polynomial of the form $C_{FD_{off}} \approx a_{fd}\alpha_f^2 + b_{fd}\alpha_f + c_{fd}$. The curve of the fin drag coefficient with no vehicle positioning offset and zero drag at zero angle of attack is given in expression 4.4. The drag force introduced by the fins at zero angle of attack is assumed to be zero in this thesis because of two reasons: First, precise values of steady drag forces can not be accurately obtained with the current platform due to low frequency drifts along axis X_m; and second, the observed variations of drag force are small in comparison with the drag force introduced by the cavitator.

$$C_{FD} = a_{fd}\alpha_f^2 = 9.3734\alpha_f^2 \tag{4.4}$$

The quadratic model of drag force as a function of the fin angle of attack (α_f) is compared in Figure 4.7 with the experimental drag data, which is translated to match

with the quadratic form as in the cavitator case (Section 4.1.1). The time evolution of the drag force measurements is compared in Figure 4.8 with the quadratic model that includes the effect of the filter and offset in the vehicle positioning ($C_{FD_{off}} \approx a_{fd}\alpha_f^2 + b_{fd}\alpha_f + c_{fd}$). The fin angle of attack is of the form $\alpha_f(t) \approx \delta_f(t) = 7sin(2\pi t)$. Figures 4.7 and 4.8 show agreement between the experimental data and quadratic model of drag produced by the fins.

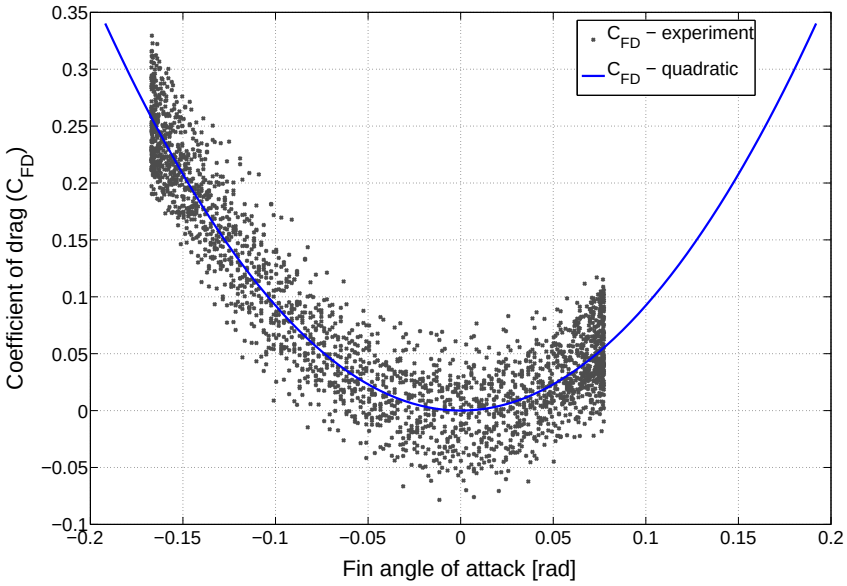

Figure 4.7: Fin drag coefficient versus fin angle of attack

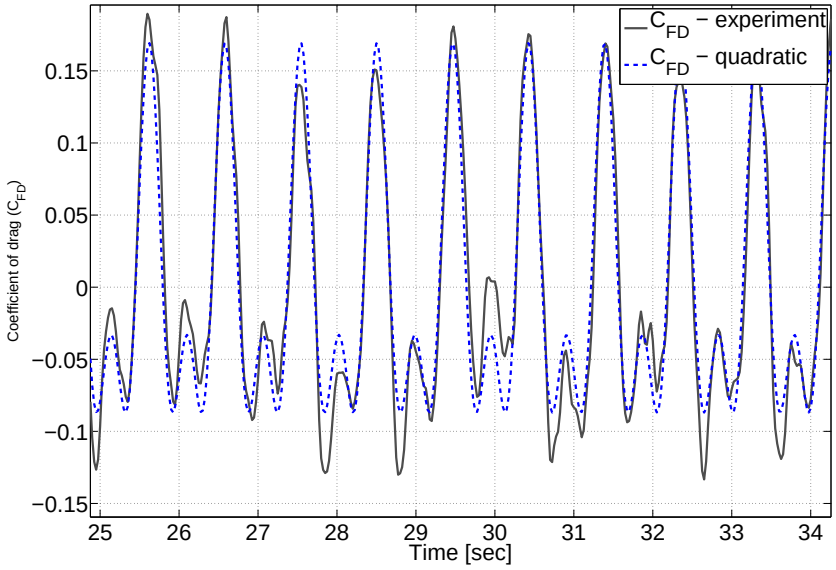

Figure 4.8: Time domain validation of fin drag coefficient C_{FD}

The lift and drag force coefficients given in equations 4.3 and 4.4 are used for the dynamical modeling of the HSSV presented in Section 4.2.

4.1.3 Perturbed Flow

Supercavity Isolation

The results of the first experiment described in Section 3.2.3 are presented in this section. Recall that for this experiment the fins are mounted on the test vehicle. Figure 4.9 shows the action of the gust generator on forces F_x and F_z in the body frame, which is different to the wind frame due to variations of the water velocity direction. This Figure is divided into three parts, from left to right; first, the vehicle is completely wetted, which results in F_x and F_z oscillations of approximately 0.5 and 2 Newtons of amplitude respectively; second, the supercavity is initialized; and third, the supercavity is established, for which the oscillation amplitudes in F_x and F_z are decreased to approximately 0.1 and 0.5 Newtons respectively. This shows a reduction of nearly 75% in both F_x and F_z perturbations generated by the gust generator. The remaining

oscillations are mostly due to the fin angle of attack variations; therefore, removing the fins yields to almost null oscillations of F_x and F_z.

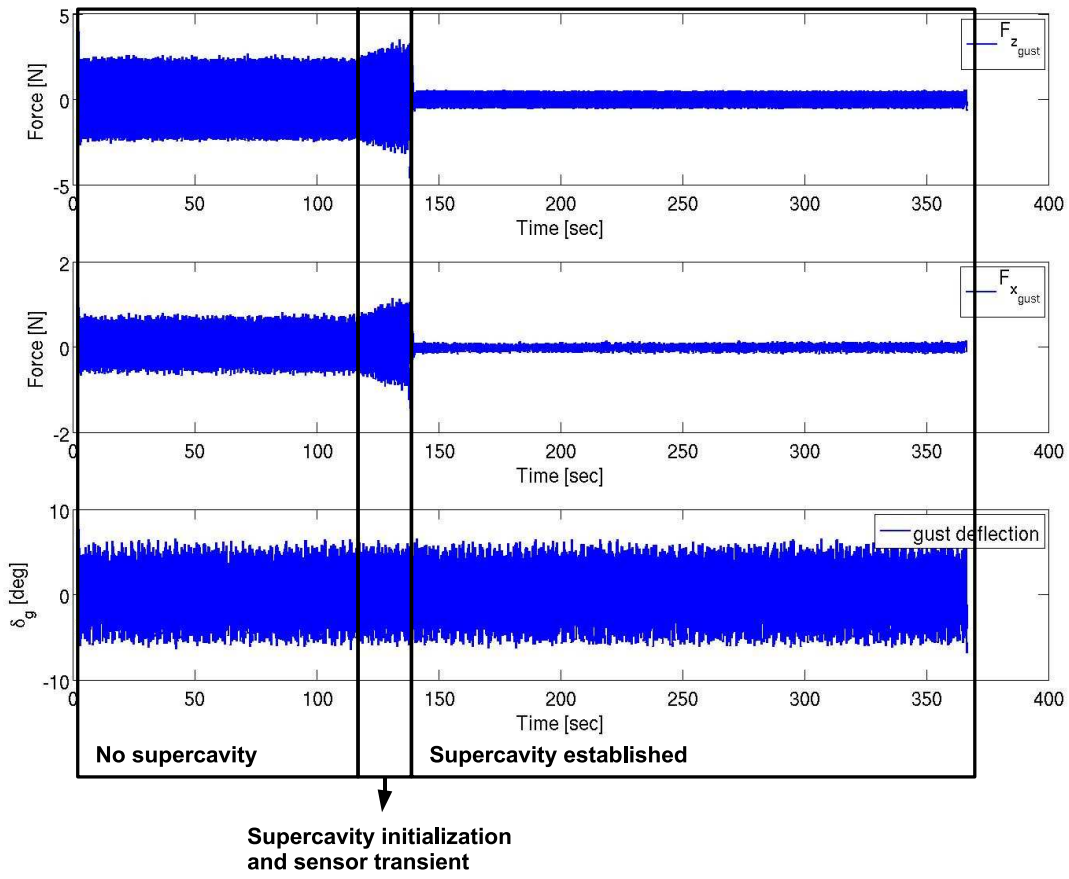

Figure 4.9: Gust effect with and without supercavitation

The presence of disturbances for a non-supercavitating underwater vehicle translates to variations of the angle of attack observed by the vehicle's body. Since the entire body is wetted, the force variations are higher than variations in a partially wetted body enveloped with a supercavity.

Perturbed Flow with no Fins

The results of the second experiment described in Section 3.2.3 are presented in this section. Recall that the objective of the experiment is to evaluate the effect of perturbed flow on the test vehicle with no fins. Figure 4.10 shows the force oscillations produced by the gust generator, considered in the body frame. These force oscillations are null in comparison with forces observed when the fins are on the supercavitating vehicle. This occurs because variations in the cavitator angle of attack produced by the perturbed flow lead to very small variations of the forces in the body frame.

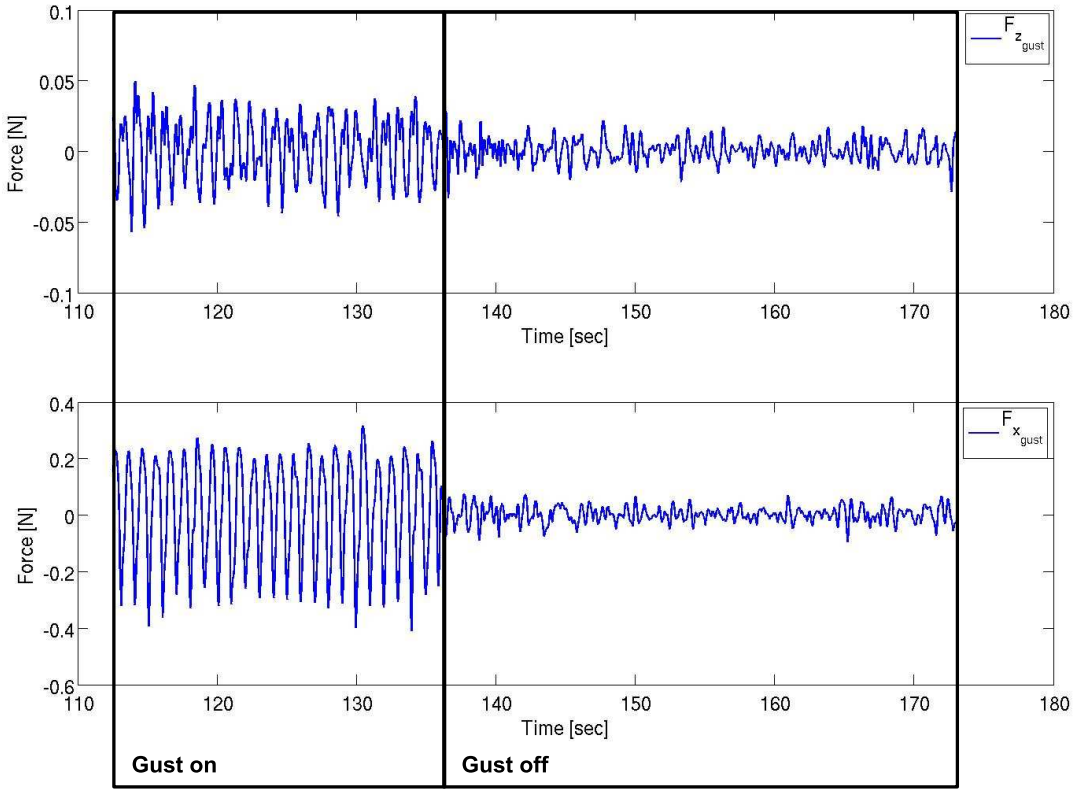

Figure 4.10: Gust generator effect without fins

The cavitator forces in the body frame, given in expressions 2.12 and 2.13, show that for small values of δ_c, the effect of small variations in α_c do not have impact on the forces ($F_{x_{cav}}$ and $F_{z_{cav}}$). Specifically, for $\delta_c = 0$, equations 2.12 and 2.13 are rewritten

into equations 4.5 and 4.6.

$$F_{x_{cav}} = -\frac{1}{2}\rho||V_{cav}||^2 A_c C_{D0}(1+\sigma)\cos(\alpha_c) \tag{4.5}$$

$$F_{z_{cav}} = 0 \tag{4.6}$$

These equations suggest that for small values of α_c variations in $F_{x_{cav}}$ are small and variations of $F_{z_{cav}}$ are null. These derivations follow what is observed in the experiment whose results are shown in Figure 4.10.

4.1.4 Cavitator Angle of Attack and Supercavity Geometry

The results from the first experiment described in Section 3.2.4 are depicted in Figure 4.11, which shows the steady bubble geometry for three cavitator deflections ($\delta_c \approx \alpha_c$). Notice that the cavity axis deformation ($h(x)$), described in Section 2.7, is the distance between the blue and red lines.

Figure 4.12 is obtained based on the second experiment described in Section 3.2.4. Figure 4.12 shows the time evolution of three geometric parameters of the supercavity: Supercavity axis deformation ($h(x)$) at $x = L_{max}/2$), distance to section with maximum diameter ($L_{max}/2$), and maximum diameter of the supercavity sections (D_{max}). These geometric parameters are described in Section 2.7, depicted in Figure 2.5, and obtained using pictures of the tunnel test section as described in Section 3.2.4.

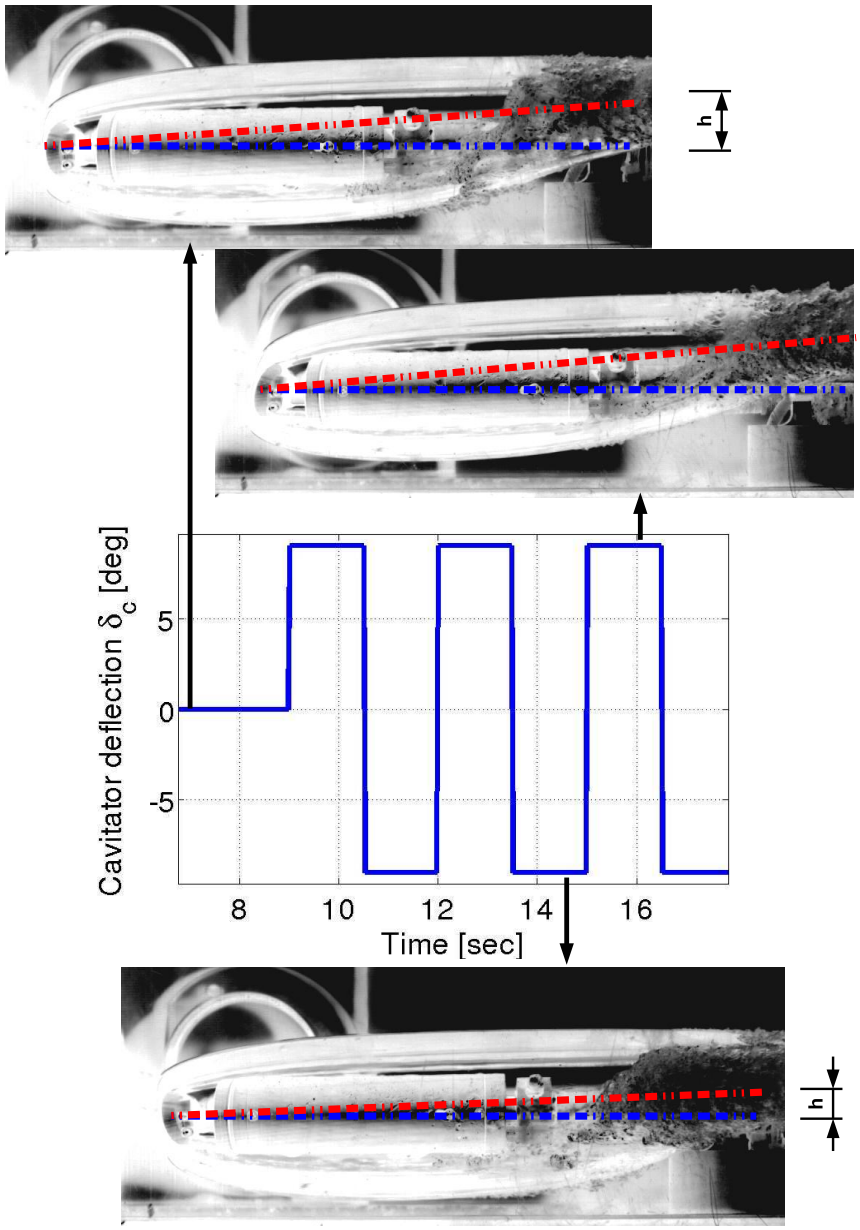

Figure 4.11: Bubble response to cavitator pulses

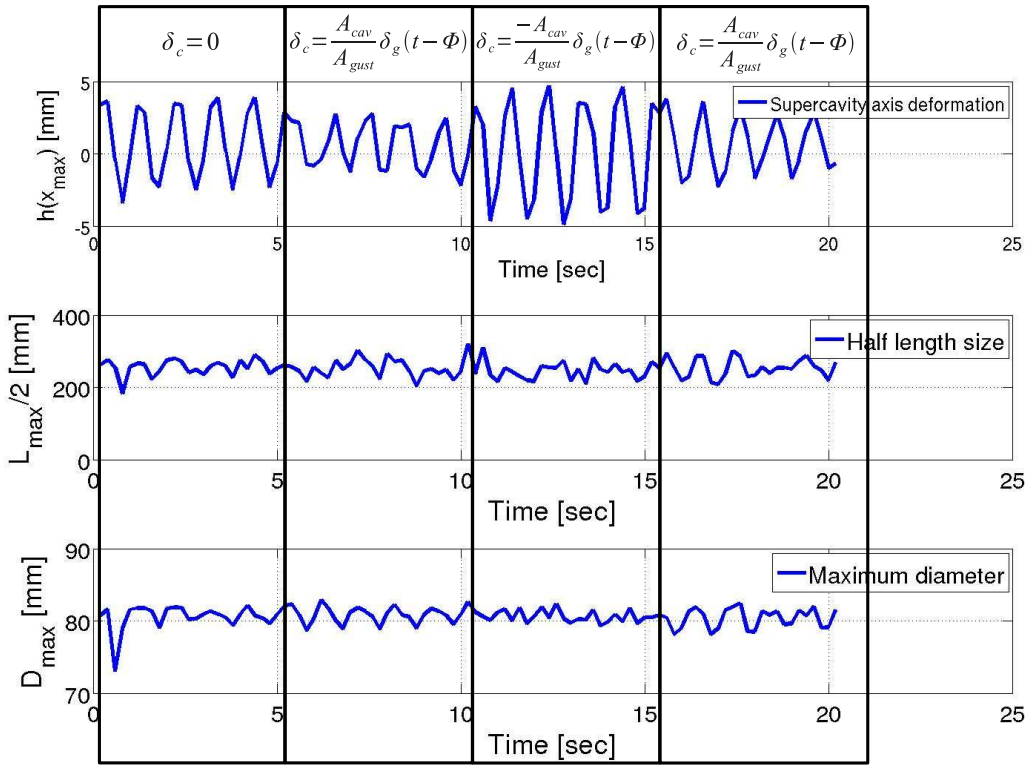

Figure 4.12: Supercavity geometric parameter with cavitator/gust phase shift

Figure 4.12 suggests that variations in $L_{max}/2$ and D_{max} are very small, but not zero since they show small oscillations at the same frequency of the gust generator and cavitator deflections (1 Hz). On the other hand, the cavity axis deformation $h(x)$ has appreciable variations. The amplitude of the $h(x)$ oscillations are function of the phase between the gust generator ($\delta_g(t) = A_{gust}\sin(2\pi f_{gust}t)$) and cavitator deflection ($\delta_c(t) = \frac{A_{cav}}{A_{gust}}\delta_g(t-\Phi) = A_{cav}\sin(2\pi f_{gust}(t-\Phi))$). Therefore, the cavitator deflection has control authority on the cavity axis displacements produced by the perturbed flow. Notice that $h(x = L_{max}/2)$ decreases when $\delta_c(t)$ changes from $\delta_c(t) = \frac{A_{cav}}{A_{gust}}\delta_g(t-\Phi) = A_{cav}\sin(2\pi f_{gust}(t-\Phi))$ to $\delta_c(t) = -\frac{A_{cav}}{A_{gust}}\delta_g(t-\Phi) = A_{cav}\sin(2\pi f_{gust}(t-\Phi) - 180^o)$.

4.1.5 Planing Force

This section presents an initial view to planing forces and an approach to generate them in the SAFL high speed water tunnel. Measurements of planing forces obtained through the experiment described in Section 3.2.5 are shown and briefly discussed. However, validation of mathematical models available in the literature is out of the scope of this thesis.

The results of the experiment described in Section 3.2.5 are presented in Figure 4.13, which shows the non-steady planing force measurements. Planing was achieved through oscillations of the gust generator at 1 Hz while the cavitator deflection was set to $\delta_c = 10^o$. Figure 4.13 also shows pictures of the vehicle fully wetted and the vehicle with maximum immersion of its aft end. In this experiment, forces are considered in the vehicle body frame; hence, positive forces in X_b and Z_b axes point left and down respectively.

The magnitude of force $F_{z_{planing}}$ is about 1 N, which is comparable with the force along Z_b generated by 5 degrees of cavitator deflection at the same water speed. The magnitude of force $F_{x_{planing}}$ represent a small variation in comparison to the axial force produced by the cavitator, which is of the order of 10 Newtons. According to these results, planing has a considerable effect on the vehicle motion because force $F_{z_{planing}}$ has high amplitude. Similarly, steady planing forces measured through experiments not described in this manuscript also lead to the same force magnitudes. The validation or development of mathematical models of planing forces can be performed through steady or non-steady planing experiments in which the immersion of the vehicle aft end should be measured and related to forces $F_{x_{planing}}$ and $F_{z_{planing}}$.

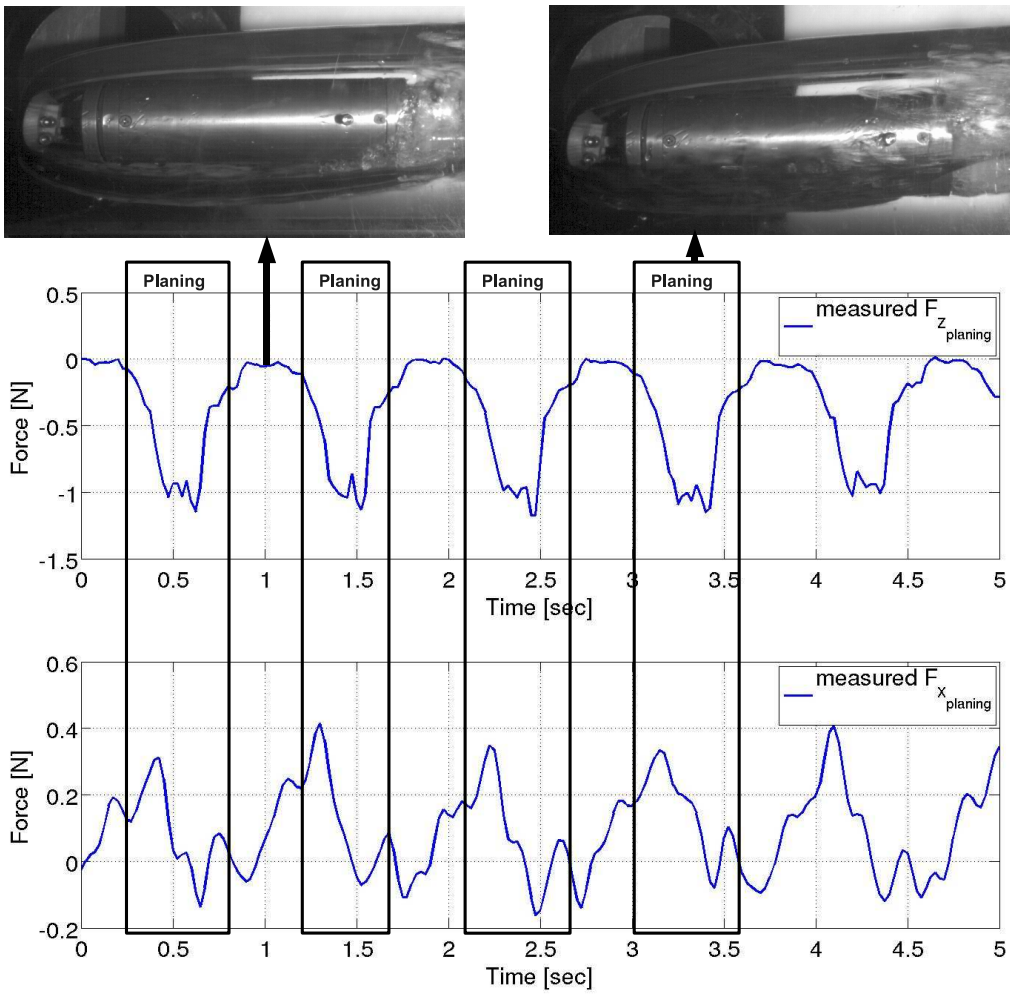

Figure 4.13: Dynamic planing force

4.2 Mathematical Model of HSSV Longitudinal Motion

The analysis of stability characteristics and control strategies for the HSSV motion requires a model of the vehicle dynamics, which are defined by the forces and moments acting on the vehicle body. The forces considered in this thesis to construct the vehicle equations of motion are produced by a disk cavitator, two lateral wedge fins, gravitational acceleration, and perturbed flow (gusts). Although this thesis is focused on the

longitudinal motion of the HSSV, the same force models can be used to derive the six degree of freedom equations of motion. Based on the results presented in Sections 4.1.1, 4.1.2 and 4.1.3 a nonlinear version of the HSSV equations of motion and equilibrium conditions are presented in Section 4.2.1. A linear approximation of the vehicle dynamics is derived in Section 4.2.2. Section 4.2.3 shows simulation results of the vehicle motion subject to perturbations of the control surfaces, cavitator and fins.

4.2.1 Nonlinear Model

Equations of Motion

The equations of motion of a HSSV in the longitudinal plane presented in Section 2.2.2 are rewritten in equations 4.7, 4.8, and 4.9. Force and moments are described in the moving body frame attached to the vehicle center of gravity and depicted in Figure 2.1.

$$m(\dot{u} + qw) = F_{x_{cav}} + F_{x_{fins}} + F_{x_{dist}} + F_{x_g} + F_{x_{thrust}} + F_{x_{planing}} \tag{4.7}$$

$$m(\dot{w} - qu) = F_{z_{cav}} + F_{z_{fins}} + F_{z_{dist}} + F_{x_g} + F_{z_{planing}} \tag{4.8}$$

$$I_{yy}\dot{q} = -l_c F_{z_{cav}} + l_f F_{z_{fins}} + l_f F_{z_{dist}} + M_{y_{planing}} \tag{4.9}$$

Cavitator

The forces and moments produced by the cavitator, expressed in the body frame, are given in equations 4.10, 4.11, 4.12, 4.13, and 4.14.

$$F_{x_{cav}} = -\frac{1}{2}\rho||V_{cav}||^2 A_c C_{D0}(1+\sigma)\cos(\alpha_c)\cos(\delta_c) \tag{4.10}$$

$$F_{z_{cav}} = \frac{1}{2}\rho||V_{cav}||^2 A_c C_{D0}(1+\sigma)\cos(\alpha_c)\sin(\delta_c) \tag{4.11}$$

$$M_{y_{cav}} = -l_c F_{z_{cav}} \tag{4.12}$$

$$\alpha_c = tan^{-1}\left(\frac{w - l_c q}{u}\right) + \delta_c \tag{4.13}$$

$$V_{cav} = \begin{bmatrix} u \\ 0 \\ w - l_c q \end{bmatrix} \tag{4.14}$$

Fins and Perturbed Flow

The perturbed flow translates to variations of the fin angle of attack that in turn vary the forces and moments acting on the vehicle's body. Hence, these forces and moment about Y_b ($F_{z_{dist}}$, $F_{z_{dist}}$, and $l_f F_{z_{dist}}$) can be simulated through perturbations to the fin angle of attack (α_f) or equivalently to the cavitator deflection (δ_c). A discussion about the perturbed flow effect on the vehicle motion is presented in Section 4.1.3. The forces and moments, described in the body frame and generated by the fins and perturbed flow are described by equations 4.15 , 4.16 , 4.17, 4.18, 4.19, and 4.20. α_f^{dist} is the perturbed fin angle of attack representing the effect of gusts. Recall that $\frac{\partial C_{FL}}{\partial \alpha_f} = 4.8487$ and $a_{fd} = 9.3734$.

$$F_{x_{fins}} + F_{x_{dist}} \approx \frac{1}{2}\rho ||V_{fin}||^2 S_f(-a_{fd}(\alpha_f + \alpha_f^{dist})^2 \cos(\theta_V^b) + \frac{\partial C_{FL}}{\partial \alpha_f}(\alpha_f + \alpha_f^{dist}) \sin(\theta_V^b)) \tag{4.15}$$

$$F_{z_{fins}} + F_{z_{dist}} \approx \frac{1}{2}\rho ||V_{fin}||^2 S_f(-a_{fd}(\alpha_f + \alpha_f^{dist})^2 \sin(\theta_V^b) - \frac{\partial C_{FL}}{\partial \alpha_f}(\alpha_f + \alpha_f^{dist}) \cos(\theta_V^b)) \tag{4.16}$$

$$M_{y_{fin}} = l_f(F_{z_{fin}} + F_{z_{dist}}) \tag{4.17}$$

$$V_{fin} = \begin{bmatrix} u \\ 0 \\ w + l_f q \end{bmatrix} \tag{4.18}$$

$$\alpha_f = tan^{-1}\left(\frac{w + l_f q}{u}\right) + \delta_f \tag{4.19}$$

$$\theta_V^b = \alpha_f - \delta_f = tan^{-1}\left(\frac{w + l_f q}{u}\right) \tag{4.20}$$

Gravitational Acceleration

The gravitational forces, expressed in the body frame, are given by equations 4.21 and 4.22. The pitch angle (θ) is positive in the clockwise direction.

$$F_{x_g} = -mg\sin(\theta) \tag{4.21}$$

$$F_{z_g} = mg\cos(\theta) \tag{4.22}$$

Planing

The integration of planing to the equations of motion is out of the scope of this thesis. This topic can be found in references [3], [4], and [1].

Thrust

Thrust (F_{thrust}) is assumed as a constant force acting along the X_b axis of the HSSV. This force is used to trim the vehicle at the desired speed.

HSSV Equilibrium

For the vehicle to be at trim ($\dot{u} = \dot{w} = \dot{q} = \dot{\theta} = 0$) the thrust ($F_{thrust}$) and forces generated by the control surface deflections (δ_c and δ_f), need to cancel out the forces in the X_b and Z_b axes as well as the moments about Y_b. The trim conditions for a vehicle flying at zero angle of attack ($u = U_0$,$w = 0$), zero pitch rate ($q = 0$), and pitch angle $\theta = \theta_0$ are presented as follows.

$$F^0_{thrust} = mg\sin(\theta_0) + \frac{1}{2}\rho U_0^2 A_c C_{D0}(1+\sigma)\cos^2(\delta_c) + \frac{1}{2}\rho U_0^2 S_f a_{fd}(\delta_f)^2 \tag{4.23}$$

$$F^0_{z_{cav}} + F^0_{z_{fins}} = mg\cos(\theta_0) \tag{4.24}$$

$$F^0_{z_{cav}} l_c - F^0_{z_{fins}} l_f = 0 \tag{4.25}$$

F^0_{thrust}, $F^0_{z_{cav}}$, and $F^0_{z_{cav}}$ denote the forces at equilibrium. Solving for forces $F^0_{z_{cav}}$ and $F^0_{z_{fins}}$, expressions 4.26 and 4.27 are obtained.

$$F^0_{z_{cav}} = -\frac{l_f mg\cos(\theta_0)}{l_f + l_c} \tag{4.26}$$

$$F^0_{z_{fins}} = -\frac{l_c mg\cos(\theta_0)}{l_f + l_c} \tag{4.27}$$

The cavitator and fin deflections for trim, computed based on equations 4.26, 4.27, 4.11, and 4.16, are given in expressions 4.28 and 4.29 respectively.

$$\delta^0_c = -\frac{1}{2}\sin^{-1}\left(\frac{4l_f mg\cos(\theta_0)}{(l_f + l_c)\rho U_0^2 A_c C_{D0})(1+\sigma)}\right) \tag{4.28}$$

$$\delta^0_f = \frac{2l_c mg\cos(\theta_0)}{(l_f + l_c)\rho U_0^2 S_f \frac{\partial C_{FL}}{\partial \alpha_f}} \tag{4.29}$$

The surface deflections δ^0_c and δ^0_f constitute only a fraction of δ_c and δ_f. Hence, the total surface deflections of the cavitator and fins are divided into the deflections for trim (δ^0_c and δ^0_f) and the deflections for the vehicle control (δ^c_c and δ^c_f). Equations 4.30 and 4.31 formalize this idea.

$$\delta_c = \delta^0_c + \delta^c_c \tag{4.30}$$

$$\delta_f = \delta^0_f + \delta^c_f \tag{4.31}$$

4.2.2 Linear Model

A simplified model of the longitudinal dynamics of the HSSV that considers the state vector $[u, w, \theta, q]^T$ is presented in this section. The vehicle is assumed to fly at zero angle of attack ($u = U_0$ and $w = 0$), zero pitch rate ($q = 0$), and pitch angle $\theta = \theta_0$ at time $t = 0$. The initial velocities along the body axes are assumed to have small variations (δu and δw) from the initial conditions (U_0, $W_0 = 0$) respectively.

$$u = U_0 + \delta u \tag{4.32}$$

$$w = W_0 + \delta w = \delta w \tag{4.33}$$

$$q = \delta q \tag{4.34}$$

The state derivatives are $\delta\dot{u} = \dot{u}$, $\delta\dot{w} = \dot{w}$, $\delta\dot{\theta} = \dot{\theta}$, and $\delta\dot{q} = \dot{q}$. For the proceeding simplifications the pitch rate δq and the perturbed velocities δu and δw are considered small quantities. Hence, multiplications among these terms are negligible. Moreover, $\sin(\gamma) \approx \gamma$, and $\cos(\gamma) \approx 1$ for γ a small angle. With these assumptions, the longitudinal equations of motion are rewritten in 4.35, 4.36, and 4.37.

$$m(\delta\dot{u} + \delta q(\delta w + W_0)) \approx m\delta\dot{u} = F_{x_{fins}} + F_{x_{cav}} + F_{x_g} + F_{x_{dist}} + F_{x_{thrust}} \tag{4.35}$$

$$m(\delta\dot{w} - \delta q(\delta u + U_0)) \approx m(\delta\dot{w} - \delta q U_0) = F_{z_{fins}} + F_{z_{cav}} + F_{x_g} + F_{z_{dist}} \tag{4.36}$$

$$I_{yy}\delta\dot{q} = l_f F_{z_{fins}} - l_c F_{z_{cav}} + l_f F_{z_{dist}} \tag{4.37}$$

Cavitator

Simplified descriptions of the cavitator forces are presented in expressions 4.38 and 4.39. It is assumed that $||V_{cav}||^2 = u^2 + (w - l_c q)^2 \approx U_0^2 + 2U_0\delta u$, $\delta u\delta_c \approx 0$.

$$F_{x_{cav}} \approx -\frac{1}{2}\rho(U_0^2 + 2U_0\delta u)A_c C_{D0}(1+\sigma) = -\frac{1}{2}\rho U_0^2 A_c C_{D0}(1+\sigma) - \rho U_0 A_c C_{D0}(1+\sigma)\delta u \tag{4.38}$$

$$F_{z_{cav}} \approx \frac{1}{2}\rho U_0^2 A_c C_{D0}(1+\sigma)\delta_c^c \tag{4.39}$$

The linear approximation of the cavitator angle of attack is given in 4.40.

$$\delta\alpha_c \approx \frac{\delta w}{U_0} - \frac{l_c\delta q}{U_0} + \delta_c^c \tag{4.40}$$

Fins and Perturbed Flow

The linear approximations of the fin forces are given in expressions 4.41 and 4.42. It is assumed that $||V_{fin}||^2 = (u^2 + (w + l_f q)^2) \approx U_0^2 + 2U_0\delta u$.

$$F_{x_{fins}} \approx \frac{1}{2}\rho(U_0^2 + 2U_0\delta_u)S_f\frac{\partial C_{FL}}{\partial \alpha_f}\alpha_f\theta_V^b \approx 0 \tag{4.41}$$

$$F_{z_{fins}} \approx \frac{1}{2}\rho(U_0^2 + U_0\delta_u)S_f\left(-\frac{\partial C_{FL}}{\partial \alpha_f}\alpha_f\right) \approx -\frac{1}{2}\rho U_0^2 S_f\frac{\partial C_{FL}}{\partial \alpha_f}\left(\frac{\delta w}{U_0} + \frac{l_f\delta q}{U_0} + \delta_f\right) \tag{4.42}$$

$\theta_V^b \approx \frac{w}{U_0} + \frac{l_f\delta q}{U_0}$ is a small angle such that $\alpha_f\theta_V^b \approx 0$. The linear approximation of the fin angle of attack is given in 4.43.

$$\delta\alpha_f \approx \frac{\delta w}{U_0} + \frac{l_f\delta q}{U_0} + \delta_f^c \tag{4.43}$$

Gravitational Acceleration

A simplified model of the gravity considering an initial pitch angle θ_0 is as follows. $\theta = \theta_0 + \delta\theta$.

$$F_{x_g} = -mg(\sin(\theta_0) + \cos(\theta_0)\delta\theta) \tag{4.44}$$

$$F_{z_g} = mg(\cos(\theta_0) - \sin(\theta_0)\delta\theta) \tag{4.45}$$

Thrust

The linear approximation of Thrust is given in equation 4.46. Notice that the approximation given in expression 4.46 cancels out the constant forces given by approximations of the cavitator and gravitational acceleration. Hence, the constant terms vanish as a result of the trim conditions.

$$F_{thrust}^0 = mg\sin(\theta_0) + \frac{1}{2}\rho U_0^2 A_c C_{D0}(1 + \sigma) \tag{4.46}$$

Linear Equations of Motion

By using the preceding simplifications and considering the trim conditions, the linear equations of motion are rewritten into expressions 4.47, 4.48 and 4.49.

$$\delta\dot{u} \approx -g\cos(\theta_0)\delta\theta - \tfrac{1}{m}\rho A_c C_{D0}(1+\sigma)U_0\delta u \tag{4.47}$$

$$\delta\dot{w} \approx U_0\delta q + \tfrac{1}{2m}\rho U_0^2 A_c C_{D0}(1+\sigma)\delta_c^c - \tfrac{1}{2m}\rho U_0^2 S_f \tfrac{\partial C_{FL}}{\partial\alpha_f}\left(\tfrac{\delta w}{U_0} + \tfrac{l_f\delta q}{U_0} + \delta_f^c\right) - g\sin(\theta_0)\delta\theta \tag{4.48}$$

$$\delta\dot{q} \approx \frac{-l_c}{2I_{yy}}\rho U_0^2 A_c C_{D0}(1+\sigma)\delta_c^c - \frac{l_f}{2I_{yy}}\rho U_0^2 S_f \frac{\partial C_{FL}}{\partial\alpha_f}\left(\frac{\delta w}{U_0} + \frac{l_f\delta q}{U_0} + \delta_f^c\right) \tag{4.49}$$

The state space model of the supercavitating vehicle with no planing effect is constructed based on equations 4.47, 4.48, and 4.49 and presented in expressions 4.50, 4.51, and 4.52.

$$\begin{bmatrix}\delta\dot{u}\\ \delta\dot{w}\\ \delta\dot{\theta}\\ \delta\dot{q}\end{bmatrix} = A_{HSSV}\begin{bmatrix}\delta u\\ \delta w\\ \delta\theta\\ \delta q\end{bmatrix} + B_{HSSV}\begin{bmatrix}\delta_c^c\\ \delta_f^c\end{bmatrix} \tag{4.50}$$

$$A_{HSSV} = \begin{bmatrix} -\tfrac{1}{m}\rho A_c C_{D0}(1+\sigma)U_0 & 0 & -gcos(\theta_0) & 0 \\ 0 & -\tfrac{1}{2m}\rho U_0 S_f \tfrac{\partial C_{FL}}{\partial\alpha_f} & -g\sin(\theta_0) & U_0 - \tfrac{l_f}{2m}\rho U_0 S_f \tfrac{\partial C_{FL}}{\partial\alpha_f} \\ 0 & 0 & 0 & 1 \\ 0 & -\tfrac{l_f}{2I_{yy}}\rho U_0 S_f \tfrac{\partial C_{FL}}{\partial\alpha_f} & 0 & -\tfrac{l_f^2}{2I_{yy}}\rho U_0 S_f \tfrac{\partial C_{FL}}{\partial\alpha_f} \end{bmatrix} \tag{4.51}$$

$$B_{HSSV} = \begin{bmatrix} 0 & 0 \\ \tfrac{1}{2m}\rho U_0^2 A_c C_{D0}(1+\sigma) & -\tfrac{1}{2m}\rho U_0^2 S_f \tfrac{\partial C_{FL}}{\partial\alpha_f} \\ 0 & 0 \\ -\tfrac{l_c}{2I_{yy}}\rho U_0^2 A_c C_{D0}(1+\sigma) & -\tfrac{l_f}{2I_{yy}}\rho U_0^2 S_f \tfrac{\partial C_{FL}}{\partial\alpha_f} \end{bmatrix} \tag{4.52}$$

4.2.3 HSSV Candidate Analysis

A hypothetical model of a high speed supercavitating vehicle is analyzed in this section. The system parameters and their values are shown in Table 4.1. The geometric parameters of the vehicle are set equal to the dimensions of the test vehicle CosCIS-3 presented in Section 3.1.3. Similarly, the initial conditions are derived from the water tunnel experiments. The velocities at which the water tunnel experiments were conducted are conservative to avoid damage of the test vehicle components.

Variable	Value
Fluid density (ρ)	1000 [Kg / m^3]
Gravitational acceleration (g)	9.81 [m/s^2]
Vehicle mass (m)	2 [Kg]
Body radius (r_{body})	0.025 [m]
Body length (l_{body})	0.21 [m]
Moment of inertia about Y_b (I_{yy})	0.0077 [Kg m^2]
Distance from c.g. to cavitator c.p. (l_c)	0.0900 [m]
Distance from c.g. to fin c.p. (l_f)	0.0793 [m]
Disk cavitator radius (r_c)	0.02 [m]
Disk cavitator area ($A_c = \pi r_c^2$)	0.0012566 [m^2]
Fin span (b)	0.035 [m]
Fin chord (c)	0.02 [m]
Fin area ($S_f = bc$)	7e-4 [m^2]
Fin angle of attack to dimensionless lift slope ($\frac{\partial C_{FL}}{\partial \alpha_f}$)	4.8487
Fin quadratic coefficient of dimensionless drag (a_{fd})	9.3734
Cavitation number (σ)	0.22
Initial pitch rate q_0	0 [rad/s]
Initial pitch angle θ_0	0 [rad]
Initial X_b velocity (U_0)	4.39611 [m/s]
Initial Z_b velocity (W_0)	0 [m/s]

Table 4.1: HSSV model parameters

The control surfaces cannot provide enough lift to the vehicle for equilibrium due to

the low speed U_0; therefore, the trim forces (equations 4.26 and 4.26) are added to the nonlinear equations of motion to guarantee equilibrium of the vehicle at initial time. The control surface deflections are zero for a vehicle trimmed with the imposed forces applied at the cavitator and fins. This enables the simulation of the vehicle motion subject to disturbances (perturbed flow) and perturbations to the initial states and control surface deflections. For higher values of U_0 and the same cavitation number σ, the control surface deflections δ_c^0 and δ_f^0 are able to zero out the forces along X_b and Z_b as well as the moments about Y_b. For instance, if the same vehicle is considered with $U_0 = 15$ [m/s], then $\delta_c^0 = -3.77$ [deg] and $\delta_f^0 = 1.557$ [deg].

The nonlinear model of the vehicle motion is implemented in Matlab/Simulink by using equations derived in Section 4.2.1. The linear model is constructed through the state space representation presented in Section 4.2.2. The state space matrices for the linearized model given the parameters and conditions of Table 4.1 are given in expressions 4.53 and 4.54.

$$A_{HSSV} = \begin{bmatrix} -9.371 & 0 & -9.8 & 0 \\ 0 & -12.73 & 0 & 13.98 \\ 0 & 0 & 0 & 1 \\ 0 & -265.8 & 0 & -21.26 \end{bmatrix} \tag{4.53}$$

$$B_{HSSV} = \begin{bmatrix} 0 & 0 \\ 70.28 & -190.9 \\ 0 & 0 \\ -1651 & -3987 \end{bmatrix} \tag{4.54}$$

The poles of the system are located at $s_{p1} = 0$, $s_{p2} = -9.37$, $s_{p3} = -17 + 60.8i$, and $s_{p4} = -17 - 60.8i$. The system has a pole at zero that makes the system marginally stable and shows up in the response of δu and $\delta\theta$ to both δ_c and δ_f. The time domain responses of the nonlinear and linear systems to a doublet sequence applied to the fin and cavitator deflections are presented in Figures 4.14, 4.15, 4.16, and 4.17.

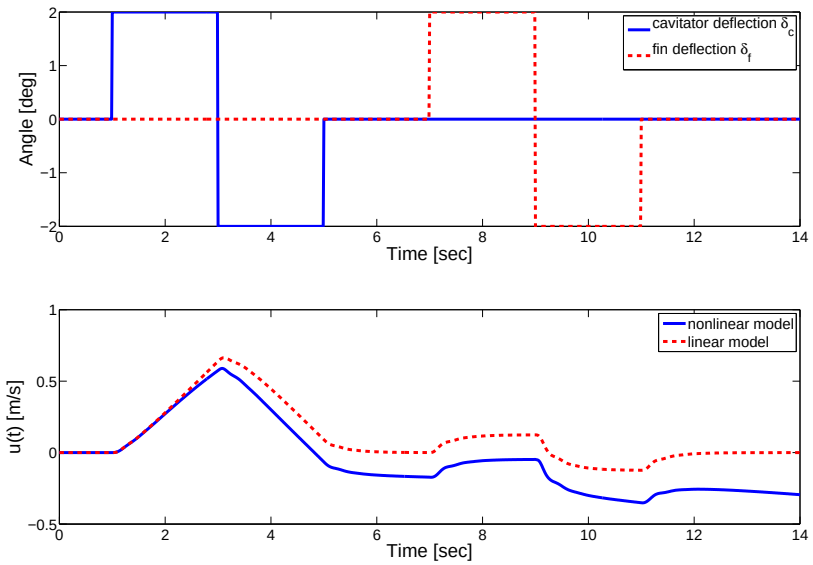

Figure 4.14: Control surface deflections and X_b velocity time response

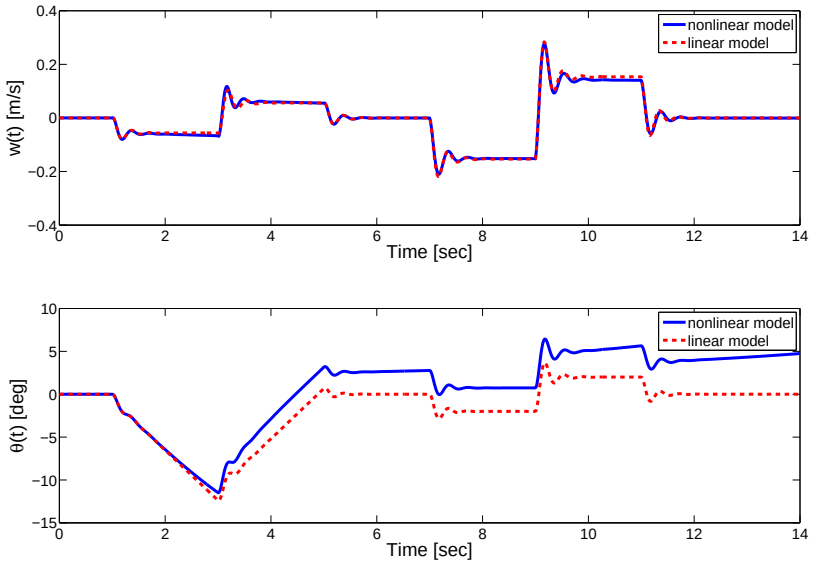

Figure 4.15: Z_b velocity and pitch angle time response

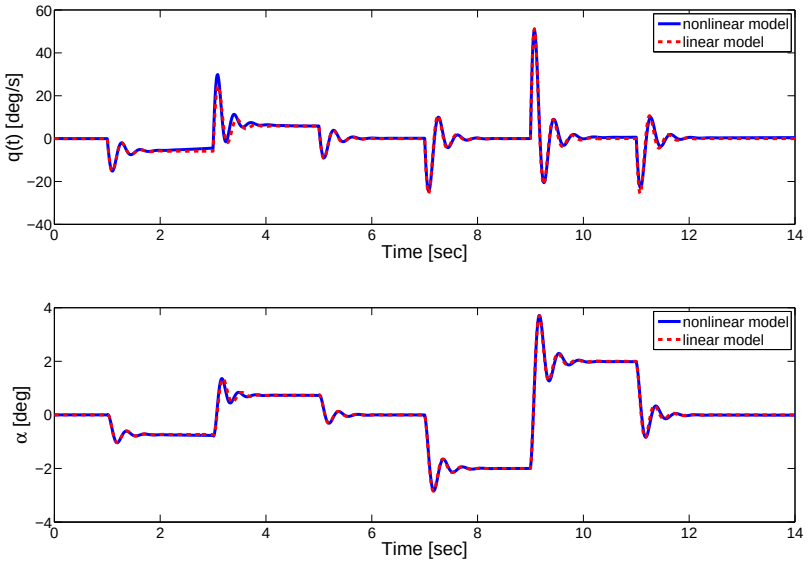

Figure 4.16: Pitch rate and vehicle angle of attack time response

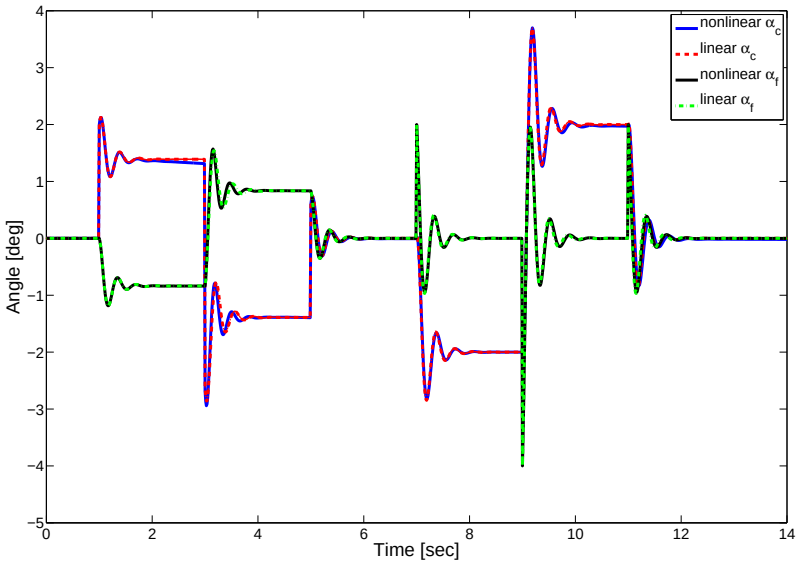

Figure 4.17: Cavitator and fin angles of attack time response

Figures 4.14, 4.15, 4.16, and 4.17 show agreement between the linear and nonlinear versions of the mathematical model of the vehicle longitudinal motion for small perturbations of the control surface deflections.

Chapter 5

Control Validation Methods

The main objective of this chapter is to present an approach to the validation and testing of the control systems of a supercavitating test vehicle in realistic flight scenarios. The validation platform is constructed based on the SAFL high speed water tunnel capabilities and HSSV modeling infrastructure presented in Section 3.1. A controller designed for disturbance rejection and pitch angle reference tracking is also presented in this chapter as well as a description of the experiments conducted on the test platform to assess the HSSV closed-loop system performance. This chapter is organized as follows: Section 5.1 describes the concept, architecture, implementation, components, and use of the control validation infrastructure. Section 5.2 presents a control law designed to track pitch angle reference commands and reject external disturbances. Finally, section 5.3 describes an experiment conducted to evaluate the HSSV closed-loop system response to pitch angle reference commands, perturbations applied to the cavitator command, and disturbances produced by the gust generator described in section 3.1.4.

5.1 Hybrid Test Platform for Supercavitating Vehicles

Hybrid testing combines analytical and experimental methods to test specific parts of a complex system in realistic scenarios. This method has been successfully used in structural engineering to study the effect of earthquakes and strong winds on structures [7]. For example, a structural specimen that is part of a large structure can be tested via hybrid simulation to avoid the construction and testing of the entire structure. The

test platform for this specimen would consists of the following: Forces applied to the specimen prototype are measured and sent to a real-time computer, which propagates the dynamics of the whole structure. The simulation of the structure dynamics generates values of the specimen displacements, which are used to command actuators that deform/displace the specimen prototype. These displacements generate forces that are measured and used again to propagate the structural dynamics. This loop is executed for a extensive amount of time to validate properties of the tested structure. A detailed discussion of this approach is presented in [7] and [8].

Specifically, for the supercavitating vehicle considered in this thesis, hybrid testing is used to evaluate control algorithms running on the vehicle's flight computer and under realistic flight scenarios created in the SAFL high speed water tunnel. The experimental part of the system consists of the real-time flight computer and the supercavitating test vehicle interacting with the supercavity, fluid, and fluid perturbations produced by the gust generator. This interaction generates hydrodynamic forces used by the analytical part of the system, which is the Motion Simulation Computer (MSC). The MSC derives the vehicle states, which are used by the embedded flight computer to drive the vehicle's motion through the forces generated by the control surfaces (cavitator and fins). The test platform introduced in this chapter is referred to as Hybrid Test Platform for Supercavitating Vehicles (HyTPSV).

5.1.1 Concept

For the development of the HyTPSV platform, it is assumed that the HSSV linear equations of motion accurately represent the vehicle nonlinear dynamic model at the desired flight conditions. Two facts inspired the system concept: First, it is possible to compute the forces produced by both cavitator and fin deflections ($F^*_{\delta_c}$ and $F^*_{\delta_f}$) by using force/moment measurements acting on the supercavitating test vehicle. Second, the linear equations of motion, rewritten into equations 5.1, 5.2, 5.3, 5.4, and 5.5, present a form in which force contributions from the states and control surface deflections are separated. Thus, the vehicle motion can be constructed by combining two components: 1) Real-time measurements of forces produced by the control surface deflections, and 2) real-time simulation of the vehicle dynamics on the motion simulation computer. In other words, it is assumed that $F_{\delta_c} \approx F^*_{\delta_c}$ and $F_{\delta_f} \approx F^*_{\delta_f}$.

$$m\dot{u} + mg\cos(\theta_0)\delta\theta + \rho A_c C_{D0}(1+\sigma)U_0\delta u \approx 0 \tag{5.1}$$

$$m\dot{w} - mU_0\delta q + mg\sin(\theta_0)\delta\theta + \frac{1}{2}\rho U_0^2 S_f \frac{\partial C_{FL}}{\partial \alpha_f}\left(\frac{\delta w}{U_0} + \frac{l_f \delta q}{U_0}\right) \approx F_{\delta_f} + F_{\delta_c} \tag{5.2}$$

$$I_{yy}\delta\dot{q} + \frac{l_f}{2}\rho U_0^2 S_f \frac{\partial C_{FL}}{\partial \alpha_f}\left(\frac{\delta w}{U_0} + \frac{l_f \delta q}{U_0}\right) \approx l_f F_{\delta_f} - l_c F_{\delta_c} \tag{5.3}$$

$$F_{\delta_c} = \frac{1}{2}\rho U_0^2 A_c C_{D0}(1+\sigma)\delta_c^c \tag{5.4}$$

$$F_{\delta_f} = -\frac{1}{2}\rho U_0^2 S_f \frac{\partial C_{FL}}{\partial \alpha_f}\delta_f^c \tag{5.5}$$

As discussed in section 4.1.3, the perturbed flow generates forces only because variations in the fin angle of attack; therefore, gust generator oscillations has effect on $F^*_{\delta_f}$, but not on $F^*_{\delta_c}$.

System Benefits and Limitations

The advantages of the test platform are:

- Captures realistic hydrodynamic vibrations and forces applied to each control surface.
- Enables the testing of the vehicle motion under complex flow conditions difficult to reproduce with computer simulations; for instance, perturbed flow produced by the oscillating foil gust generator.
- Enables the evaluation of control algorithms on the real-time flight computer.

- Validates models of the overall closed loop system and its components; for example, actuation systems, time delay, and embedded system (hardware and software).
- The cavitator forces mostly depend on the cavitator actuation; hence, for the same cavitator deflection, a static test vehicle and a moving vehicle produce the same forces in the vehicle's body frame. In other words, the HyTPSV platform accurately recreates the cavitator forces of the moving vehicle whose dynamics are simulated.

The limitations of the test platform are:

- The forces acting on the fin are not entirely captured by the system because the fin immersion is constant in both the mathematical model and water tunnel experiments. Immersion variations can be captured if the test vehicle had motion.
- Planing forces, the result of the vehicle motion respect to the bubble, are not captured by the platform. Planing can be achieved by using a moving test vehicle or by deflecting the supercavity such that planing is achieved.
- The effect of thrust is not experimentally captured.

5.1.2 System Architecture

The system is composed of three main components: 1) Test vehicle including actuated control surfaces and force measurement unit; 2) real-time embedded flight computer; and 3) motion simulation computer. Figure 5.1 depicts the system architecture.

The forces produced by the interaction among fluid, control surfaces and supercavity are measured by the force measurement unit and then sent to the MSC. The MSC computes the forces produced by deflections in the cavitator and fins. These forces together with the HSSV equations of motion are used to propagate the system states (u,w,q,θ). The states (sensor data) are sent to the real-time flight computer, where the control law at each time step is computed. Lastly, the control law commands the surface deflections (δ_c and δ_f) to vary the forces applied to the test vehicle and therefore drive the HSSV motion.

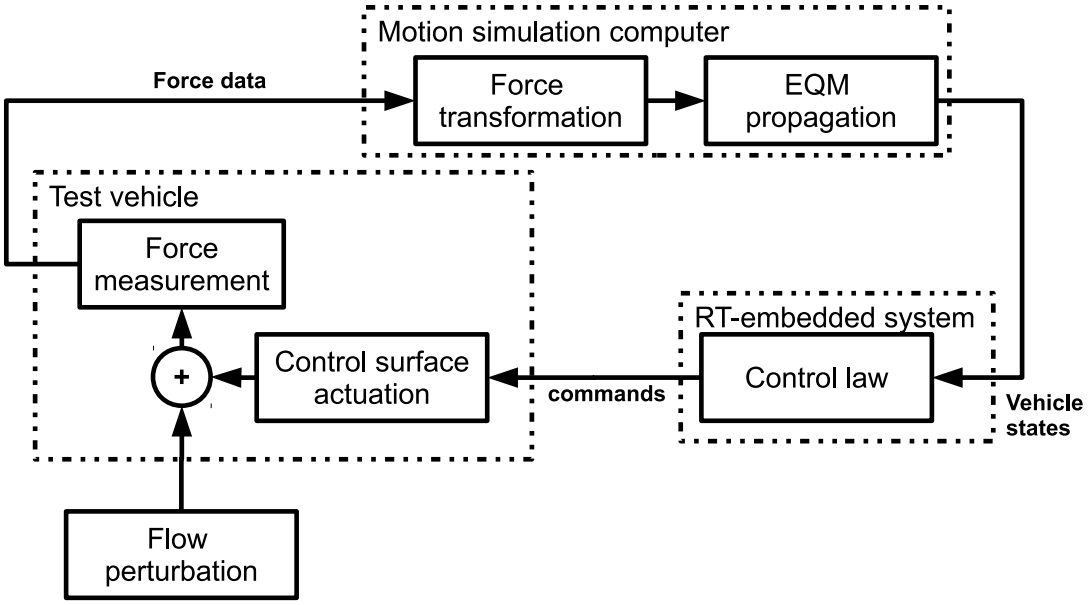

Figure 5.1: Overall architecture of control validation platform (HyTPSV)

5.1.3 Vehicle Motion Simulation

The HSSV linear dynamics presented in equations 5.1, 5.2, and 5.3 are propagated via integration of the state derivatives ($\dot{u}$, $\dot{w}$, $\dot{q}$, $\dot{\theta}$). Figure 5.2 shows a schematic of the dynamics propagation implemented on the MSC. Notice that the gray dashed blocks correspond to real time force measurements whereas white blocks correspond to the analytical part of the dynamic simulation.

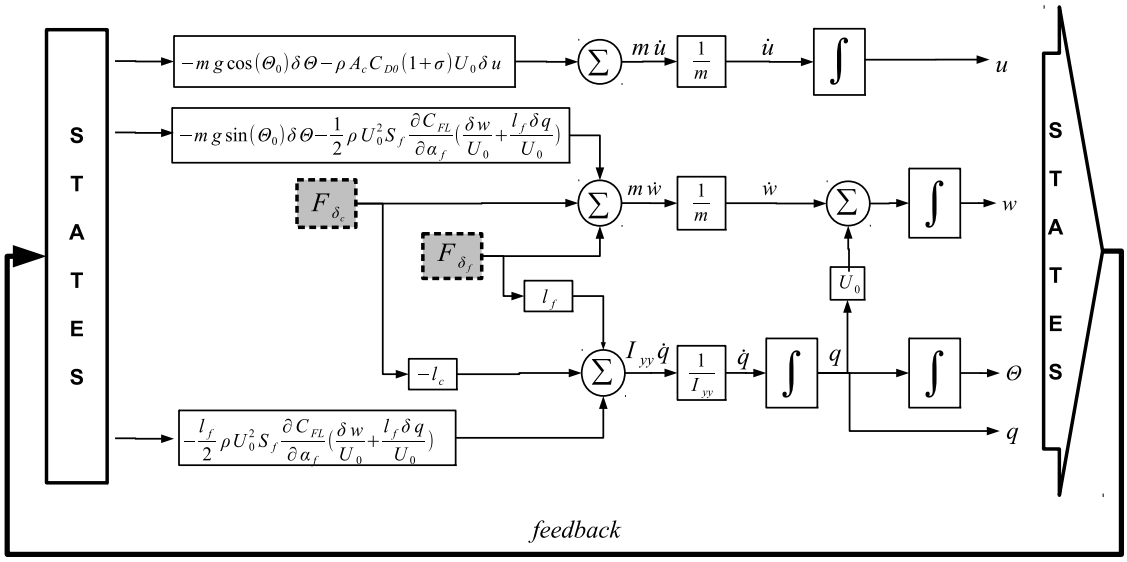

Figure 5.2: Linear dynamics propagation

5.1.4 Force Transformation

The total force (F_m) and moment (M_m) applied to the test vehicle are measured with respect to the measurement frame (X_m, Y_m, Z_m) that is depicted in Figure 5.3.

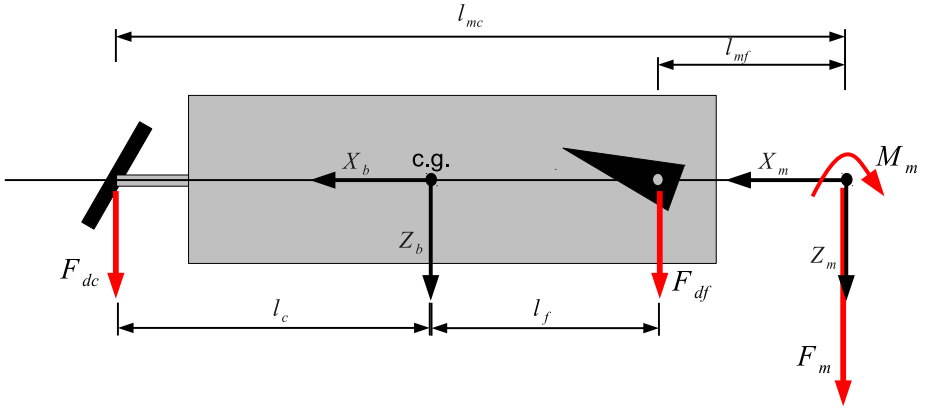

Figure 5.3: Schematic of forces on test vehicle

The interest is on forces F_{δ_c} and F_{δ_f} acting along Z_b or equivalently Z_m. Thus, given

F_m and M_m, forces F_{δ_c} and F_{δ_f} are computed though equations 5.6 and 5.7 respectively.

$$F_{\delta_c} = \frac{F_m l_{mf} - M_m}{l_{mf} - l_{mc}} \tag{5.6}$$

$$F_{\delta_f} = \frac{M_m - F_m l_{mc}}{l_{mf} - l_{mc}} \tag{5.7}$$

Recall that F_{δ_c} captures the cavitator deflection effect while F_{δ_f} captures the effect of both fin deflections and gust generator oscillations (perturbed flow).

5.1.5 System Implementation

A specific implementation of the (HyTPSV) developed in this thesis is depicted in Figure 5.4.

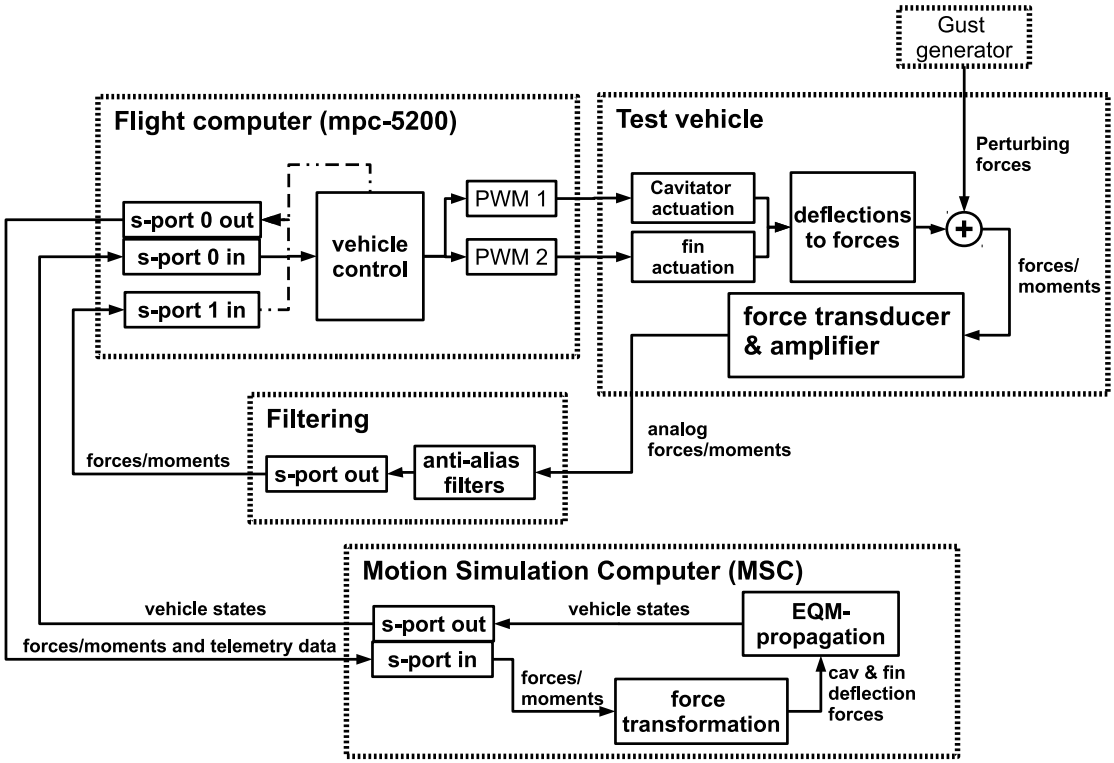

Figure 5.4: Schematic of HyTPSV implementation

The components of the implemented test platform are described below.

Supercavitating Test Vehicle

The supercavitating test vehicle described in subsection 3.1.3 together with the gust generator described in section 3.1.4 were installed in the SAFL high speed water tunnel to deploy the hybrid test system.

Motion Simulation Computer - MSC

The real-time simulation of the vehicle dynamics was implemented on a 32 bits computer with a serial port devoted to exchange data with the flight computer. The real-time dynamics propagation software, depicted in Figure 5.2, was implemented on Matlab/Simulink using Real-Time-Windows-Target [23]. The vehicle states, computed through the dynamics simulation, are transmitted via serial communication to the flight computer at 40 data frames per second. Telemetry data coming from the flight computer is read through the same serial line and transmission rate. The telemetry data contains the values of forces and moments applied to the test vehicle, deflection of the control surface, gust generator position, and flight computer time. Notice that the force measurements are sent by the flight computer because only one serial port is available in the MSC. If two serial ports were available, one port would read the force data from the filtering device while the other reads the flight computer data.

Real-Time Flight Computer

The embedded system used to run the control algorithms is described in section 3.1.7. This system reads the HSSV states through serial port s-port 1 and the force data through serial port s-port 0. By using the vehicle states the embedded system computes the control law output at each time step. The outputs of the control law are the cavitator and fin commands, which are transformed to PWM signals that drive the servomotors attached to the control surfaces. The force data, actuator commands, and time are transmitted at each time step to the MSC. The control algorithms, data acquisition, and telemetry functions are executed in a single thread that runs at 40 Hz.

5.1.6 HyTPSV Experimental Procedure

The procedure to carry out an experiment using the HyTPSV platform is as follows.

1. Initialize the high speed water tunnel at the desired speed and then establish the supercavity around the test vehicle.
2. Apply a sinusoidal command to the cavitator. The lift force data is used to obtain the cavitation number (σ) as described in section 4.1.1.
3. Initialize the dynamics simulation software (MSC) by using the value of σ found in Step 2 and the water tunnel speed. The value of the water speed has to be assigned to the initial vehicle speed in the X_b axis, that is U_0.
4. Set the cavitator deflection to zero degrees and zero out the force transducer by using the signal amplifier manual reset. Hence, the vehicle is trimmed such that measured forces are only due to variations of control surfaces and gust generator.
5. Load and run the flight computer program that contains the control law.
6. Run the dynamics simulation program on the MSC.
7. Run the gust generator if it is needed.
8. Stop the MSC program and save the experimental data.

5.2 HSSV Control

The objectives of the control system to be tested on the HyTPSV platform are disturbance rejection and tracking of pitch angle reference commands (θ_{ref}). Although both cavitator and fins can be used for the HSSV control, only the cavitator is considered in this thesis. The states used for feedback are pitch rate (q [rad/s]) and pitch angle (θ [rad]).

5.2.1 Closed-Loop System Model

A cascade control structure is adopted in this thesis. This structure enables effective disturbance rejection in the inner loop. Figure 5.5 shows a schematic of the closed-loop system that integrates the HSSV dynamics, actuation, controller, and delay of the interconnection. The filtering stage is not considered for the control design because its bandwidth is much higher than the bandwidth of the vehicle dynamics and actuation.

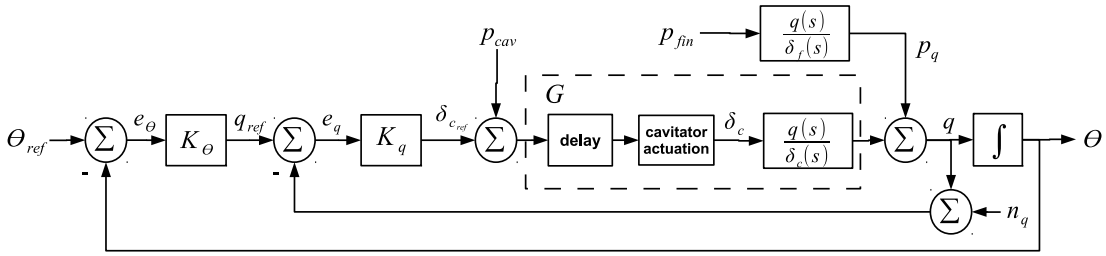

Figure 5.5: HyTPSV closed-loop system

The main objective of the control system (K_q, K_θ) is to minimize e_θ and e_q under uncertain perturbations (p_{cav} and p_{fin}). p_{cav} are software induced perturbations to the cavitator deflection command ($\delta_{c_{ref}}$) and p_{fin} are perturbations to the fin angle of attack produced by the gust generator (perturbed flow). According to expression 2.21, perturbations to δ_f are equivalent to perturbations to α_f. $\frac{q(s)}{\delta_c(s)}$ and $\frac{q(s)}{\delta_f(s)}$ are the transfer functions from cavitator and fin deflections to pitch rate respectively.

The synthesis of control laws to drive the motion of the HSSV on the HyTPSV platform requires knowledge of the mathematic models of the HSSV dynamics, time delay, and actuation.

HSSV Dynamics

The same vehicle model used in subsection 4.2.3 is considered for the HyTPSV construction. Recall that the parameters to build the model correspond to the real geometry of the test vehicle and conditions in which experiments are conducted in the SAFL high speed water tunnel.

Time Delay

The communication among the HyTPSV components (MSC, flight computer, and filtering device) results in a delay of the closed-loop interconnection. This time delay was found as follows: First, a proportional controller ($K_p = 1$) was implemented to stabilize the plant whose input is the cavitator command $\delta_{c_{ref}}$ and output the pitch angle θ. Second, a step command generated in the flight computer was applied to the reference pitch angle (θ_{ref}). Finally, the time between the step and the response of θ was measured. This is the total time delay of the loop that captures: 1) Time between cavitator command and cavitator actuation, 2) time of data transmission from filtering device to flight computer, 3) time of data transmission from flight computer to MSC, 4) time of data transmission from MSC to flight computer. The total time delay was found to be 4 samples of the flight computer, whose sample time is 0.025 [sec].

The transfer function of the delay is $T_{delay}(s) = e^{-s\tau}$, being $\tau = 0.1$ [sec] the time delay. A linear approximation of $T_{delay}(s)$ is given in equation 5.8.

$$T^*_{delay}(s) = \left(\frac{1 - \frac{\tau s}{2n}}{1 + \frac{\tau s}{2n}}\right)^n \tag{5.8}$$

The order of the linear approximation is selected as $n = 4$. This provides good agreement between T^*_{delay} and T_{delay} for frequencies up to 6 Hz, which is higher than the cavitator actuation and vehicle dynamics bandwidths and therefore suitable for the system analysis at the frequencies of interest. This linear approximation of the delay is used for the control design. Figure 5.6 shows the phase of the time delay as a function of frequency as well as its linear approximation.

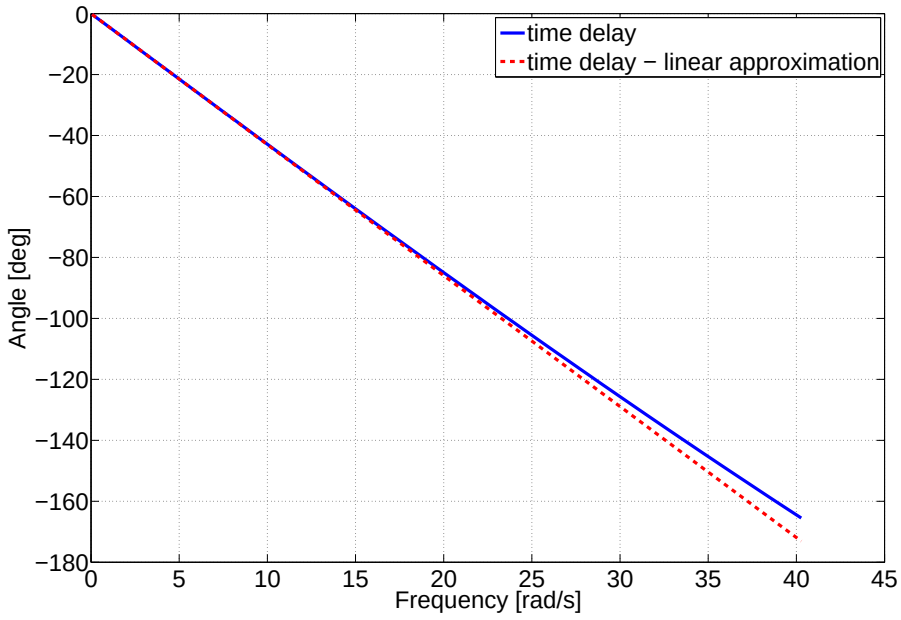

Figure 5.6: Phase plot, closed-loop time delay

Actuation Model

The model of the cavitator actuation is obtained using system identification. An autoregressive with external input estimator (ARX) model is proposed. This estimator, based on least squares, finds the parameters of a discrete time linear system given experimental input-output data and the order of the system.

The input data were frequency varying sinusoids (0.25, 0.5, 1, and 2 Hz) of amplitide 8 degrees applied to the cavitator deflection. The frequencies are conservative to avoid actuator damages experienced during previous tests. The output data were force measurements scaled such that the gain from cavitator command to force was one at low frequencies. The force measurements capture the transient response of the cavitator actuation, from which the actuation dynamics can be estimated. The time delay between cavitator command and force measurements was removed because it is considered as part of the whole closed-loop time delay, but not as part of the cavitator actuation model. The discrete time model obtained via ARX is transformed to the continuous

time transfer function presented in expression 5.9

$$\frac{\delta_c(s)}{\delta_{c_{ref}}(s)} = \frac{0.2725s + 29.5}{s + 29.5} \tag{5.9}$$

The time domain responses of the actuator and actuator ARX model given as input the frequency varying sinusoids used for the system identification are shown in Figure 5.7. Figure 5.7 shows the transition from frequency 0.5 Hz to 1 Hz for the input and output signals scaled to have maximum amplitude equal to one in the range of frequencies shown in Figure 5.7.

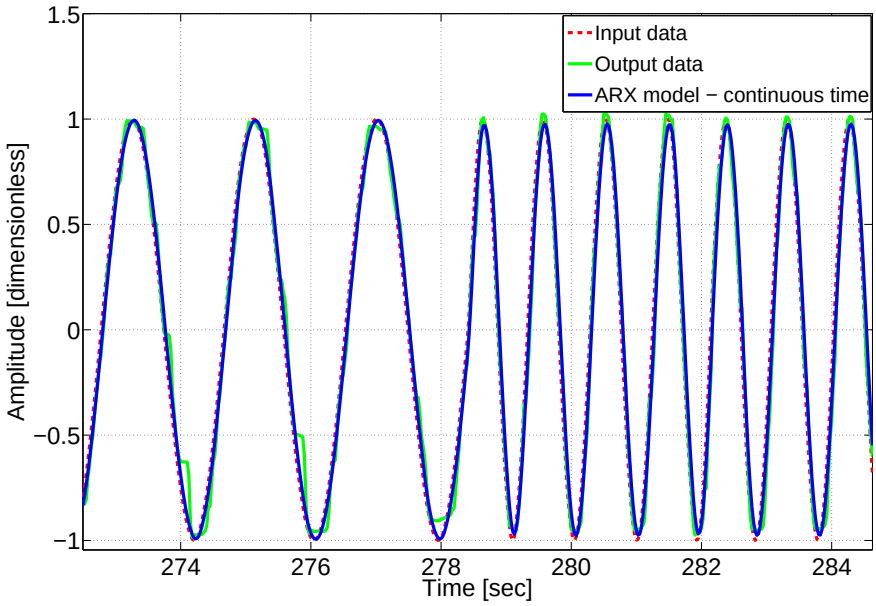

Figure 5.7: Time domain response of actuator and actuator model

The magnitude Bode plot of the actuator model described by the transfer function given in equation 5.9 is given in Figure 5.8. The bandwidth of the cavitator actuation is 32 rad/s (5.09 Hz), which is the frequency at which the actuation gain decays to -3 db. Notice also that the high frequency gain does not decay to 0 ($-\infty$ [db]) because the transfer funciton of expression 5.9 has relative degree equal to zero, that is, numerator and denominator have the same degree (1).

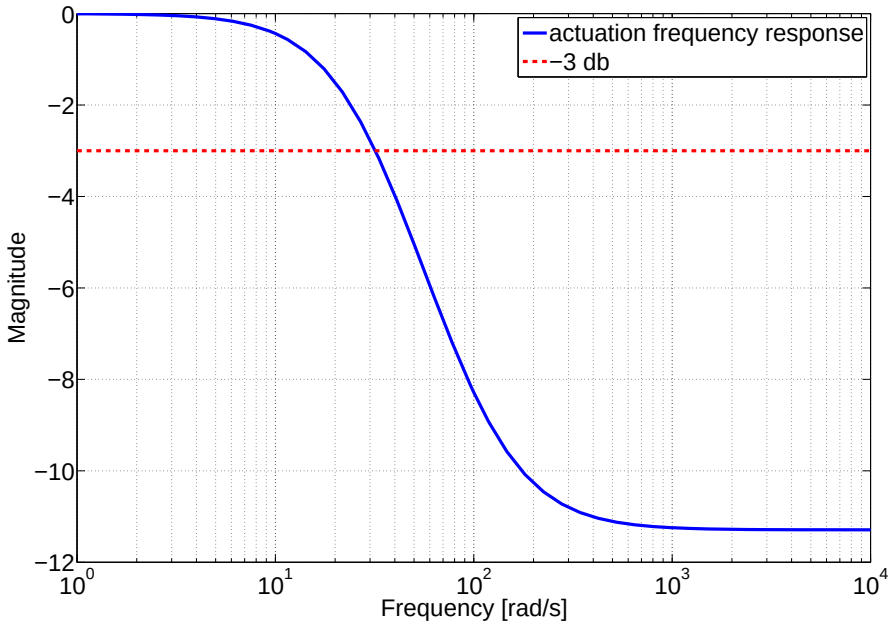

Figure 5.8: Bode magnitude, cavitator actuation

Loop Frequency Response

The frequency responses of the open-loop transfer function from cavitator command to pitch rate and anti-alias filter implemented in the filtering device are shown in Figure 5.9.

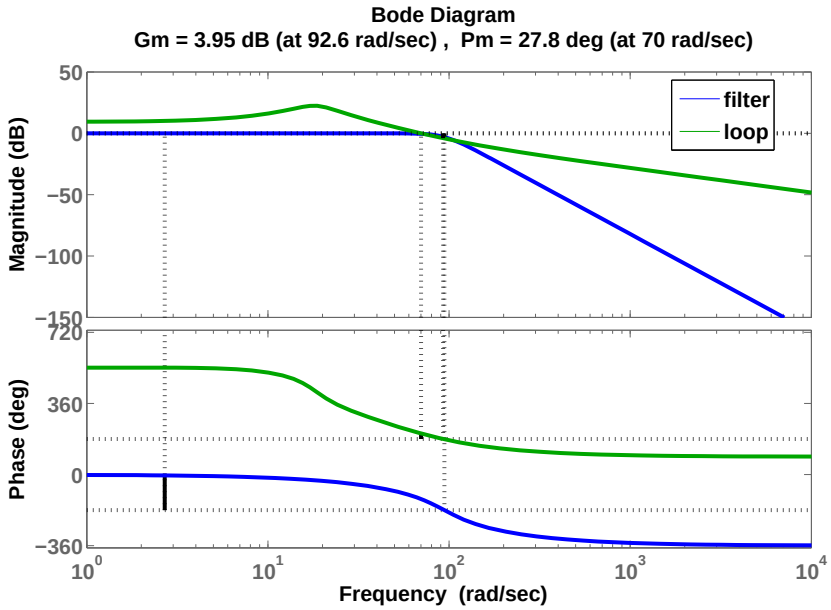

Figure 5.9: Bode plot, cavitator delfection to pitch rate

Figure 5.9 shows that the magnitude of the filter starts decaying near 94 rad/s (15 Hz) while the magnitude of the vehicle dynamics starts decaying near 20 rad/s (3.18 Hz). For this reason, the control design can be performed without considering the filtering stage described in subsection 3.1.5.

5.2.2 Control Design

Inner Loop

The objectives of inner-loop controller (K_q) are:

1. Tracking of pitch rate reference commands (q_{ref}.
2. Rejection of disturbances produced by perturbed flow and cavitator induced disturbances.
3. Keeping the cavitator commands below the position and rate saturation limits.
4. Filtering of vibrational effects caused by the vehicle structural modes and interaction with the fluid. The first mode of the vehicle structure is at 8 Hz.

The controller K_q is designed through mixed sensitivity synthesis, a particular scheme of H-infinity synthesis [10]. This method computes an optimal controller that minimizes the infinity norm of the closed loop system $T_{\bar{u}\to\bar{y}}$, depicted in Figure 5.10 and given in expression 5.10.

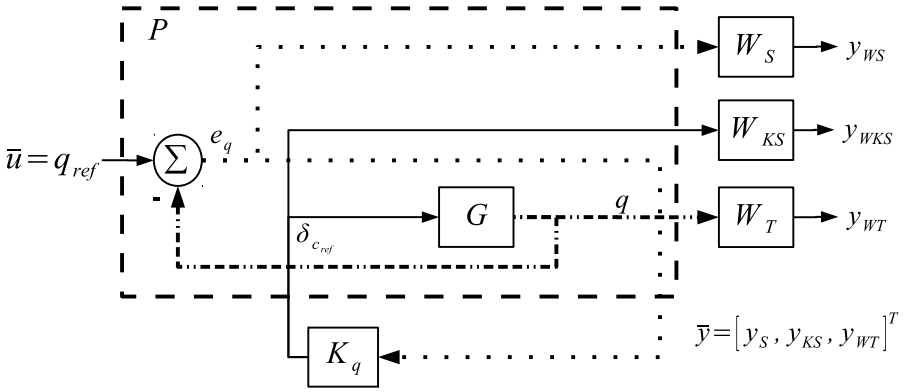

Figure 5.10: Generalized plant for H-infinity control synthesis

$$T_{\bar{u}\to\bar{y}} = \begin{bmatrix} W_S(s)S(s) \\ W_{KS}(s)K(s)S(s) \\ W_T(s)T(s) \end{bmatrix} \tag{5.10}$$

Weights $W_S(s)$, $W_{KS}(s)$, and $W_T(s)$ are used to achieve the closed-loop control objectives by shaping the frequency response of $S(s) = \frac{e_q(s)}{q_{ref}(s)} = \frac{q(s)}{p_q(s)}$, $K(s)S(s) = \frac{\delta_{c_{ref}}(s)}{q_{ref}(s)}$ and $T(s) = 1 - S(s) = \frac{q(s)}{n_q(s)}$. For simplicity, p_q is used as the disturbance instead of p_{fin}. Notice that a sinusoid applied to δ_f leads to a sinusoid of different phase and amplitude in p_q. An optimal control law satisfying the closed-loop objectives also satisfies expressions 5.11, 5.12, and 5.13 for all for all frequencies ω.

$$|S(j\omega)| < 1/|W_S(j\omega)| = |B_S(j\omega)| \tag{5.11}$$

$$|K(j\omega)S(j\omega)| < 1/|W_{KS}(j\omega)| = |B_{KS}(j\omega)| \tag{5.12}$$

$$|T(j\omega)| < 1/|W_T(j\omega)| = |B_T(j\omega)| \tag{5.13}$$

For tracking and disturbance rejection at low frequencies $S(s)$ has to be small such that the tracking error and disturbance effect on q are minimized. Given this rationale, $B_S(s) = 1/W_S(s)$ is constructed through the following parameters: Bandwidth $w_{b_S} = 9.42$ [rad/s] (1.5 Hz), low frequency gain $A_S = 0.01$, and high frequency gain $M_S = 2$. $B_S(s)$ is given in expression 5.14

$$B_S(s) = \frac{M_S s + \sqrt{7} W_{b_S} A_S}{s + W_{b_S}} = \frac{2s + 0.25}{s + 25} \tag{5.14}$$

The control effort $K(s)S(s)$ should be limited by the maximum cavitator deflection ($\delta_{c_{ref}} < \delta_{c_{max}}$) and bandwidth of control commands to avoid rate saturation. Thus, $|K(jw)S(jw)|$ is bounded by $|B_{KS}(jw)| = 1/|W_{KS}(jw)|$ such that: Bandwidth $w_{b_{KS}} = 6.29$ [rad/s] (1 Hz), low frequency gain $M_T = 1$, high frequency gain $A_T = 0.0125$, and maximum cavitator command $\delta_{c_{max}} = 0.175$ [rad] (10 deg). $B_{KS}(s)$ is given in expression 5.16.

$$B_{KS}(s) = \frac{1}{\delta_{c_{max}}} \left(\frac{A_{KS}\sqrt{(2M_{KS}^2 - 1)}s + W_{b_{KS}} M_{KS}}{\sqrt{(2M_{KS}^2 - 1)}s + W_{b_{KS}}} \right) = \frac{0.0022s + 1.1}{s + 6.28} \tag{5.15}$$

Filtering of vibrational effects beyond the actuation bandwidth is done by minimizing $|T(j\omega)|$ at high frequencies. Specifically, it is of interest to ignore the effect of the first structural mode of the test vehicle (8 Hz). The bound of $|T(jw)|$ given by $|B_T(jw)| = 1/|W_T(jw)|$ is selected such that: Bandwidth $w_{b_T} = 37.7$ [rad/s] (6 Hz), low frequency gain $M_T = 1.2$, and high frequency gain $A_T = 0.1$. $B_T(s)$ is given in expression 5.16.

$$B_T(s) = \frac{A_T\sqrt{(2M_T^2 - 1)}s + W_{b_T} M_T}{\sqrt{(2M_T^2 - 1)}s + W_{b_T}} = \frac{0.137s + 45.2}{1.37s + 37.7} \tag{5.16}$$

Given the above formulation, a controller of 8 states was obtained by using Matlab and the Robust-Control Toolbox [10]. The H-infinity cost associated to the controller is $\gamma = 2.7$, which is a suboptimal value. However, more important than optimality is the fact that the control law has very fast poles, which results in instability of the closed-loop interconnection when the controller is discretized with the flight computer sample time (0.025 sec). To decrease the magnitude of the controller poles, the optimization

is relaxed by rising the lower bound of γ to 4.1. In this way, the closed-loop system implemented with the discrete time controller accurately follows the stable response of the continuous time system. Despite the sub-optimality, the close loop interconnection created with the second controller achieves an acceptable performance and does not saturate neither the position nor rate of the cavitator for the considered inputs (tracking commands, disturbances). The tracking error at low frequencies is less than 4% while the disturbance are attenuated by 95% approximately. Therefore, this controller is selected to be tested on the HyTPSV platform. The Bode magnitude plots of $S(s)$, $B_S(s)$, $K(s)S(s)$, $B_{KS}(s)$, $T(s)$, and $B_T(s)$ are shown in Figures 5.11, 5.12, and 5.13,

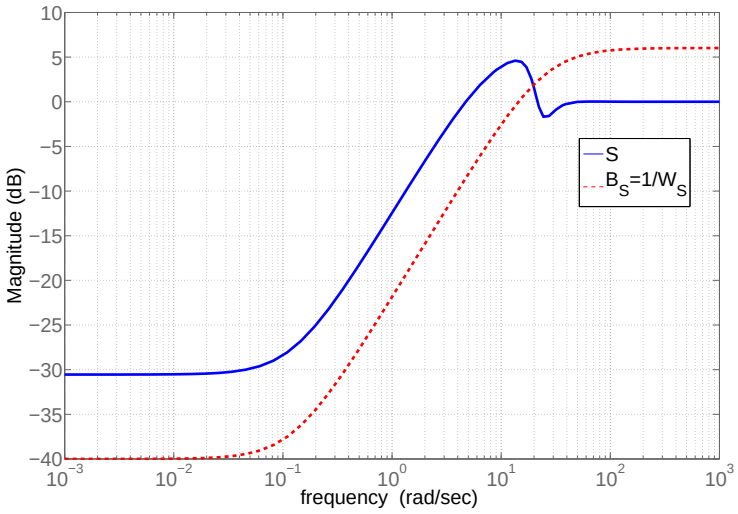

Figure 5.11: Bode magnitude, sensitivity and weight

The sensitivity transfer function obtained with controller K_q has lower bandwidth than the desired one; nevertheless, the bandwidth is acceptable as well as the low and high frequency gains. The low frequency gain indicates that the tracking error at low frequencies is lower than 4%. Moreover, $||S(j\omega)||_\infty < 2.5$ suggests good stability margins for the closed-loop interconnection.

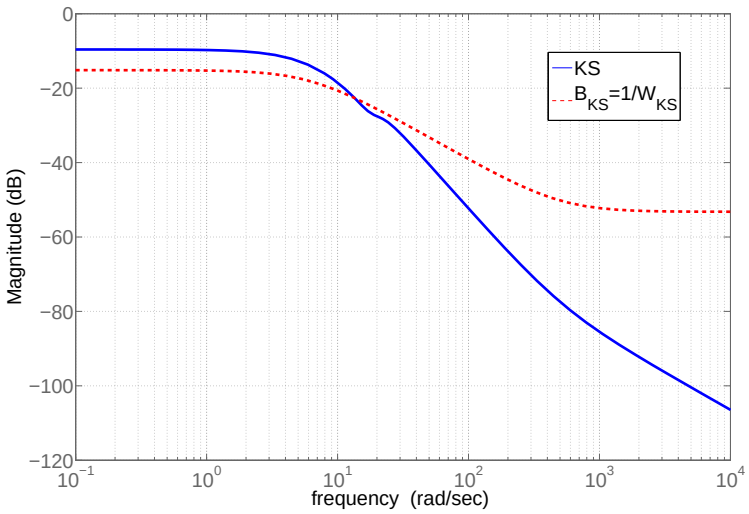

Figure 5.12: Bode magnitude, control effort and weight

Although the low frequency gain of $|K(j\omega)S(j\omega)|$ exceeds the maximum allowed cavitator deflection, the maximum pitch rate reference (q_{ref}) used by the mixed sensitivity synthesis is 1 rad/s (57.3 deg/s), which is higher than the rate commands demanded by the outer loop controller described in Section 5.2.2. Therefore, the closed-loop system does not saturate the cavitator deflection, as it is validated in Chapter 6.

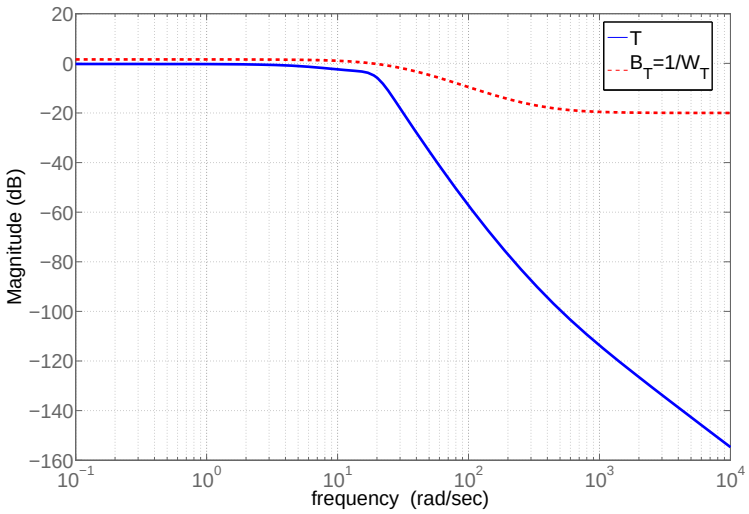

Figure 5.13: Bode magnitude, complementary sensitivity and weight

The complementary sensitivity transfer function ($T(s)$) satisfies the design specifications because its frequency magnitude is below $|B_T(j\omega)|$ for all ω. Hence, the closed-loop system filters the vibrational effects of the vehicle structure.

The transfer function from cavitator perturbations (p_c) to pitch rate (q) dictates the closed-loop performance regarding cavitator disturbance rejection. The magnitude of the frequency response of this transfer function is shown in Figure 5.14

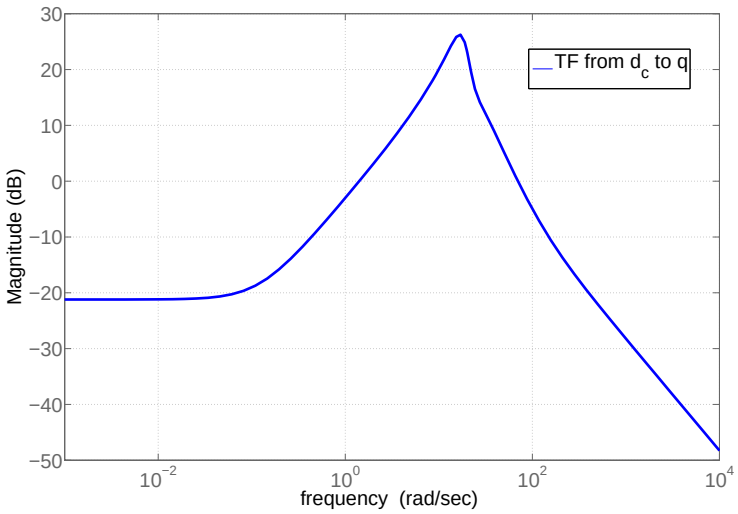

Figure 5.14: Bode magnitude, cavitator perturbation to pitch rate

The Bode magnitude of $\frac{q(s)}{p_c(s)}$ indicates that for frequencies lower than 0.9 rad/s and higher than 88 rad/s the closed-loop system attenuates cavitator perturbations below -3 db. This means that for frequencies between 0.9 and 88 rad/s, the system amplifies cavitator perturbations.

Outer Loop

The objective of the outer loop control is tracking of pitch angle reference commands (θ). This is addressed through a simple proportional controller (K_θ) that guarantees small tracking error at low frequencies, zero overshoot, and acceptable stability margins.

For $K_\theta = 1.5$ the gain margin is $GM = 13.26$ [db], phase margin is $PM = 71.97$ [deg], and overshot is zero. A Bode plot of the loop transfer function from e_θ to θ is shown in Figure 5.15.

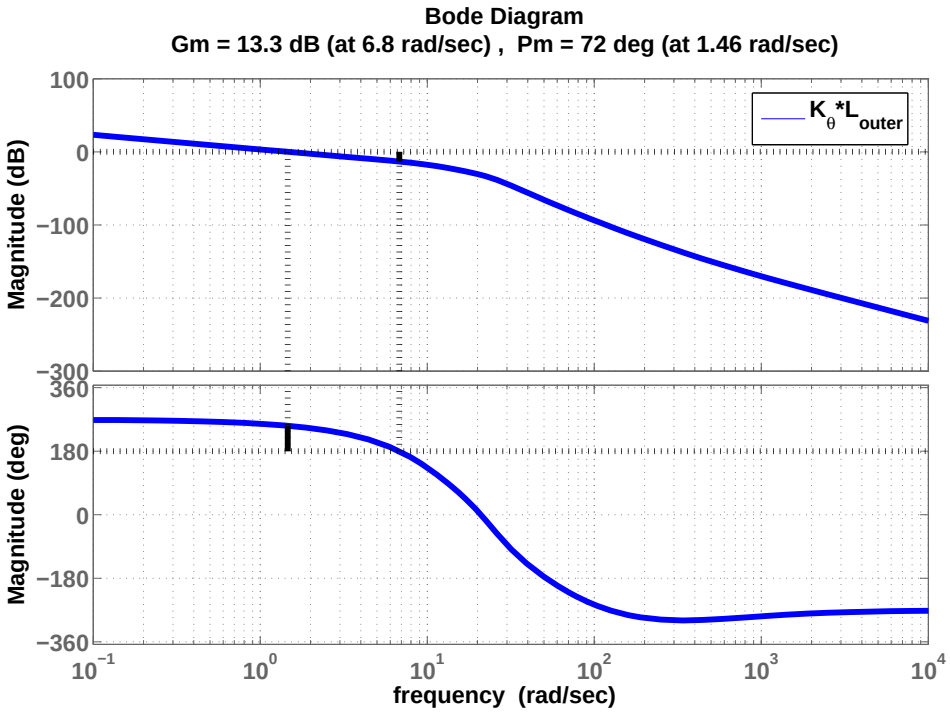

Figure 5.15: Bode: transfer function from e_θ to θ

Overall Control Structure

Both K_θ and K_q are transformed to a single controller K with two inputs (e_θ, q) and one output ($\delta_{c_{ref}}$). The controller K has the form given in expression 5.17.

$$K = [K_\theta K_q, -K_q] \tag{5.17}$$

5.2.3 Control Law Implementation

The procedure to implement and test control laws on the HyTPSV platform is as follows:

1. Given a continuous time state space representation of a linear time invariant controller and the sample time at which it is implemented in the embedded system, its discrete time version is computed. The sample time used by the flight computer to run the control law is 0.025 sec.

2. Matlab Scripts were developed to automatically generate C++ code of MIMO linear time invariant systems. The discrete time controller is automatically transformed to C++ classes through these scripts.

3. The C++ code is tested in a simulation of the system under Matlab/Simulnk. This validation stage is referred to as Software in the Loop (SIL) simulation. The SIL simulation contains models of the HSSV dynamics, actuation systems, filtering stage, and time delay.

4. The C++ code of the control law is combined with the flight computer software, compiled, and loaded onto the flight computer hardware.

5. The HyTPSV experiment is executed as is described in subsection 5.1.6.

5.3 Experimental Approach

An experiment to validate the disturbance rejection and tracking performance of the control law described in subsection 5.2.2 is presented as follows: The SAFL high speed water tunnel was run at $U_\infty = 4.39$ [m/s]. Based on discussion from section 4.1.1, the cavitation number was found to be $\sigma = 0.26$. Given U_∞ and σ, the dynamics propagation was set up and the HyTPSV platform executed. The experiment consisted of three stages.

1. A doublet perturbation generated in the flight computer program was applied to the cavitator deflection command $\delta_{c_{ref}}$. The doublet signal had an amplitude of 8 degrees and a duration of 4 seconds. Note that the cavitator perturbation is added to the control law output. Figure 5.16 shows the time evolution of the perturbation applied to the cavitator command.

2. A doublet command was applied to the pitch angle reference (θ_{ref}) to evaluate the tracking performance of the closed-loop system. The doublet command had an amplitude of 5 degrees and duration of 30 seconds. Figure 5.16 shows the time evolution of θ_{ref}. The cavitator perturbation was set to zero in this part of the experiment.

3. The gust generator was turned on to evaluate the disturbance rejection performance of the closed loop system. The frequency of the gust generator sinusoids was 0.5 Hz and the amplitude 10 degrees. The pitch reference command and cavitator perturbation were set to zero.

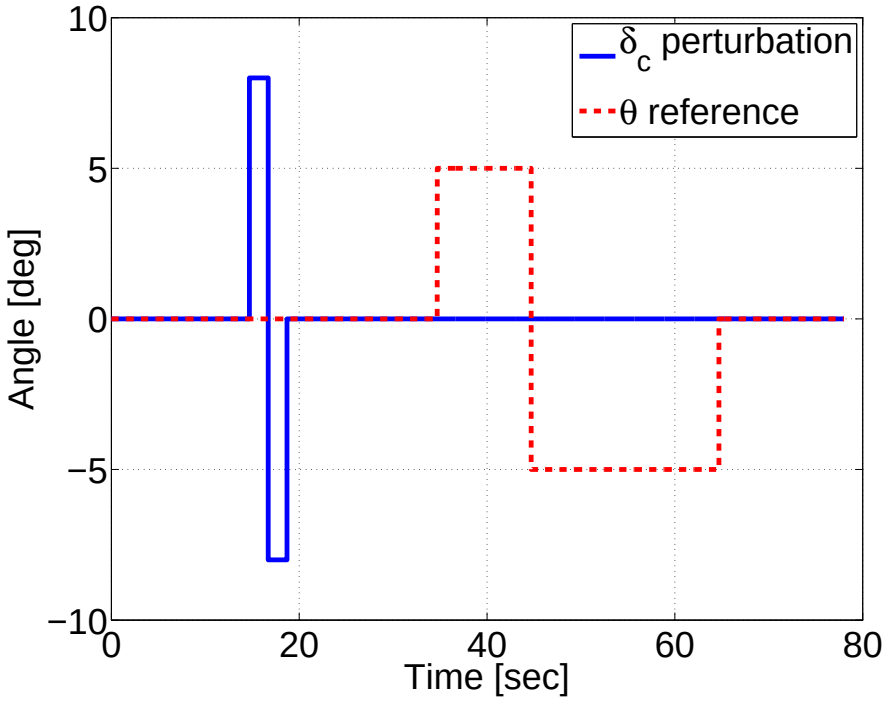

Figure 5.16: Cavitator perturbation and reference pitch angle

Chapter 6

Control Validation Results

The main objective of this chapter is the assessment of the HyTPSV platform through the control law described in Section 5.2.2 and whose objectives are tracking of pitch reference commands and disturbance rejection. Results of the experiment, described in Section 5.3, in which the control law is tested on the control validation infrastructure are presented in this chapter. The discussion of the results is divided into three sections: Section 6.1 presents experimental and simulation results of the HSSV closed-loop system response to cavitator perturbations generated in the flight computer. Experimental data and simulation results of the HSSV closed-loop system response to pitch reference commands are discussed in Section 6.2. Finally, Section 6.3 presents experimental results about the effect of perturbed flow on the HSSV closed-loop dynamics.

6.1 Cavitator Perturbations

The system response to doublet perturbations applied to the cavitator command, described in Section 5.3, is presented in this section. These perturbations are generated in the flight computer and added to the control law output, that is, the cavitator deflection command. The frequency response of the transfer function from cavitator perturbations (p_{cav}) to pitch rate (q), shown in Figure 5.14, indicates that for frequencies lower than 0.9 rad/s and higher than 88 rad/s the closed-loop system attenuates cavitator perturbations below -3 db. For the remaining range of frequencies the closed-loop does no

attenuate cavitator perturbations. The time domain responses of the cavitator command $\delta_{c_{ref}}$, cavitator and fin forces ($F_{|delta_c}$ and $F_{|delta_f}$), and vehicle states (u, w, θ, and q) are described throughout this section.

Figure 6.1 shows: 1) Cavitator doublet perturbation generated in the flight computer; 2) cavitator deflection result of the control law output plus cavitator perturbation; 3) cavitator deflection according to nonlinear and linear simulations of the closed-loop system; and 4) cavitator force computed by the MSC and scaled by $\frac{1}{0.5\rho U_0^2 A_{cav} C_{D0}(1+\sigma)}$ to obtain its corresponding cavitator deflection. Recall that cavitator and fin forces are obtained by the MSC through the force transformation described in Section 5.1.4. For visualization purposes, offsets of the cavitator deflection and forces from the experiment are removed. These offsets are produced by the controller to compensate for errors in the initial vehicle trim.

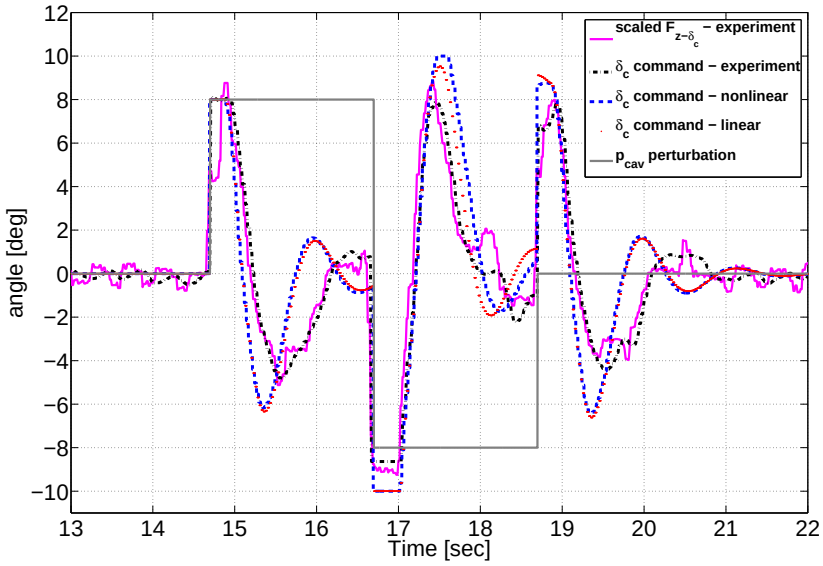

Figure 6.1: Cavitator perturbation - cavitator deflection and force

Figure shows 6.1 good agreement between the cavitator deflections from the experiment, linear and nonlinear simulations. In addition, the scaled cavitator force, computed by the MSC, follows the mathematical model of the cavitator forces discussed in Sections 2.3 and 4.1.1.

The fin force, computed through the force transformation, is shown in Figure 6.2. This force is scaled by $\frac{1}{0.5\rho U_0^2 S_f \frac{\partial C_{FL}}{\partial \alpha_f}}$ to obtain its corresponding fin deflection. The force contribution of the fin in this part of the experiment was null because the fins and gust generator had zero deflections.

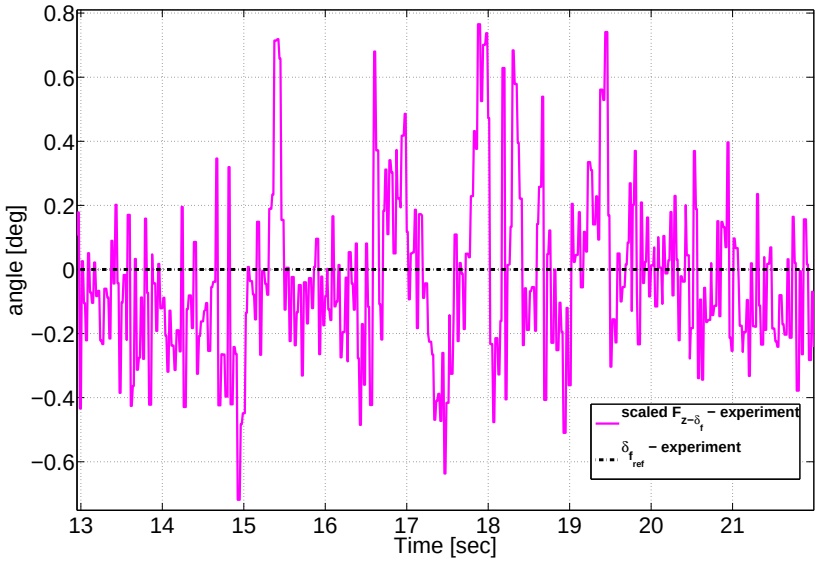

Figure 6.2: Cavitator perturbation - fin deflection and force

The pitch angle and pitch rate responses, propagated by the MSC, are shown in figure 6.3. This plot shows good agreement among the experimental data, linear, and nonlinear simulations of the closed-loop system. Notice that the pitch angle reference command is zero in this part of the experiment.

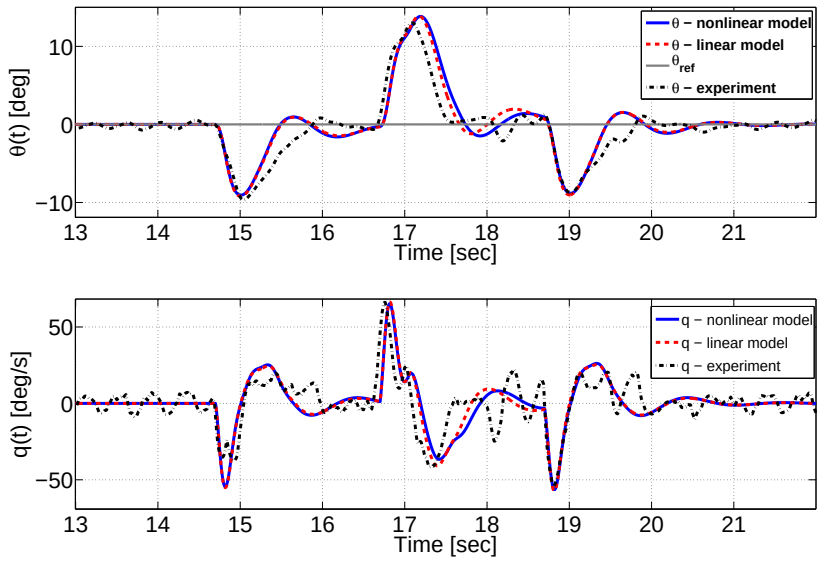

Figure 6.3: Cavitator perturbation - pitch angle and rate

The longitudinal components of the vehicle velocity (u and w), computed in the MSC, are presented in Figure 6.4.

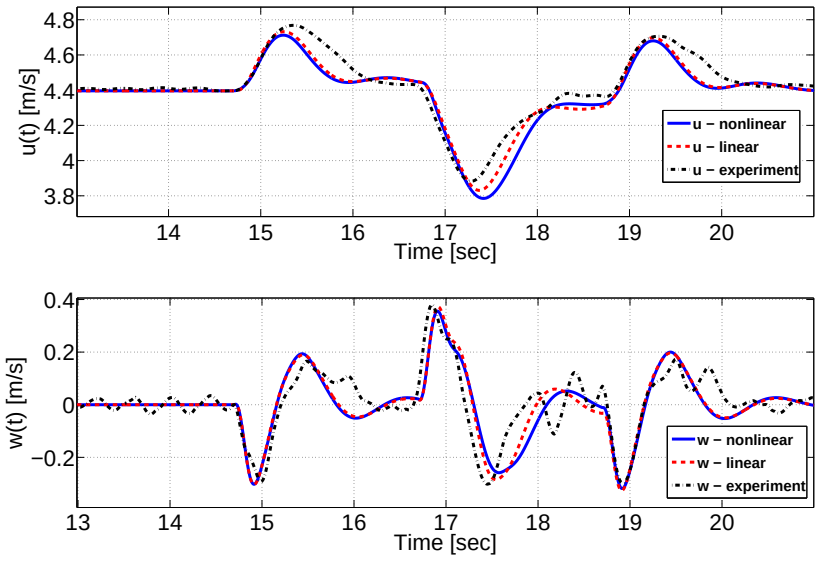

Figure 6.4: HyTPSV - velocities u and w

Although the closed loop system is able to reject the cavitator perturbations, a control law that minimizes the transfer function from cavitator disturbance (p_{cav}) to pitch rate (q) over a wide range of low frequencies would provide better performance of the closed-loop system.

6.2 Pitch Angle Reference Tracking

The tracking performance of the HSSV closed-loop interconnection is evaluated through the time domain response of the system to pitch angle reference commands described in Section 5.3. The responses to doublet reference commands of the reference cavitator deflection $\delta_{c_{ref}}$, cavitator and fin forces ($F_{|delta_c}$ and $F_{|delta_f}$), and vehicle states (u, w, θ, and q) are described throughout this section.

Figure 6.5 shows: 1) Cavitator deflection result of the control law output; 2) cavitator force computed by the MSC and scaled to obtain its corresponding cavitator deflection; and 3) linear and non-linear simulations of the cavitator deflection. For visualization purposes, offsets of the cavitator deflection and forces from the experiment are removed.

Notice that the cavitator perturbations generated in the flight computer are equal to zero in this part of the experiment. The cavitator deflection and force show good agreement validating the force transformation as well as the model of cavitator forces.

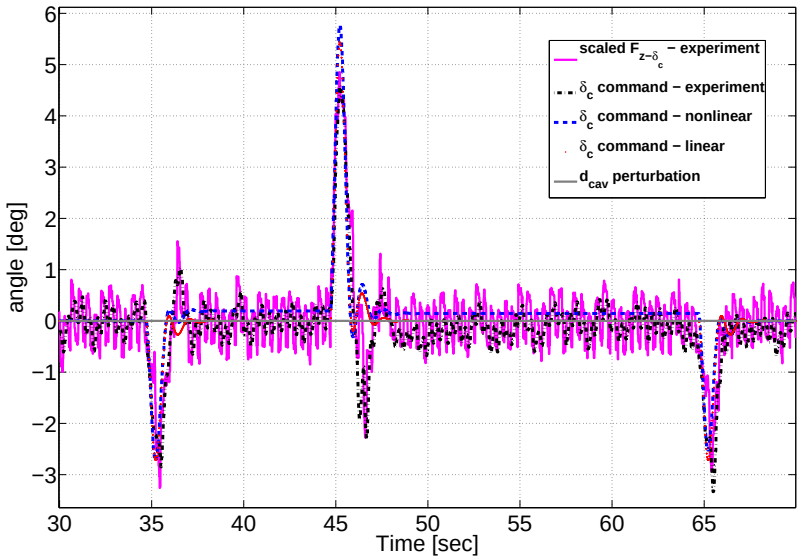

Figure 6.5: Pitch angle reference tracking - cavitator deflection and force

The fin force converted to its corresponding fin deflection (δ_f) is shown in Figure 6.6. The fin force data are close to zero because fin and gust generator deflections are both zero in this part of the experiment.

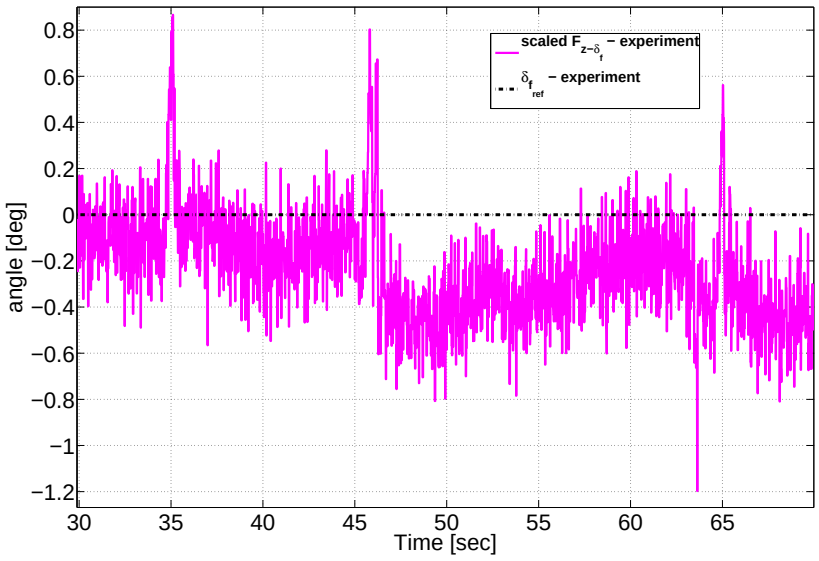

Figure 6.6: Pitch angle reference tracking - fin deflection and force

The pitch angle and pitch rate responses to the pitch angle reference tracking commands are shown in Figure 6.7. The pitch angle tracks with zero steady error the reference commands. This is expected because of the integrator in the transfer function from pitch reference command (q_{ref}) to pitch angle (θ), which is shown in Figure 5.5.

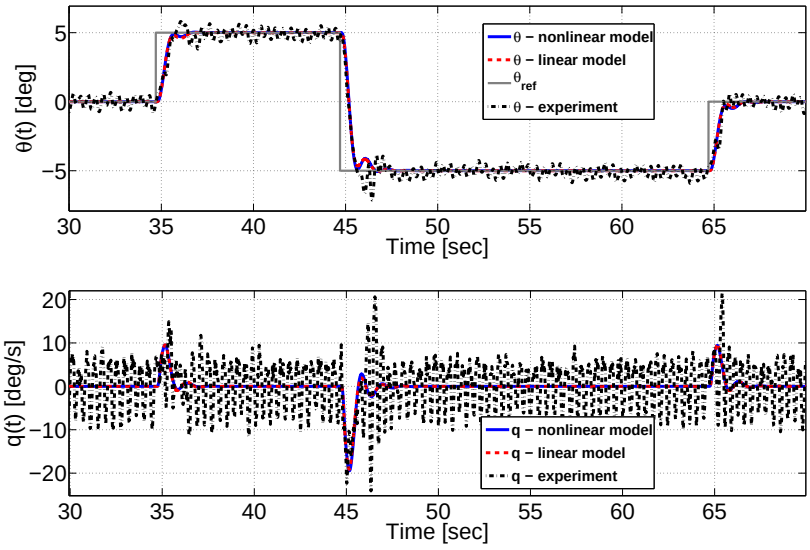

Figure 6.7: Pitch angle reference tracking - pitch angle and rate

The longitudinal components of the vehicle velocity (u and w) are presented in Figure 6.8.

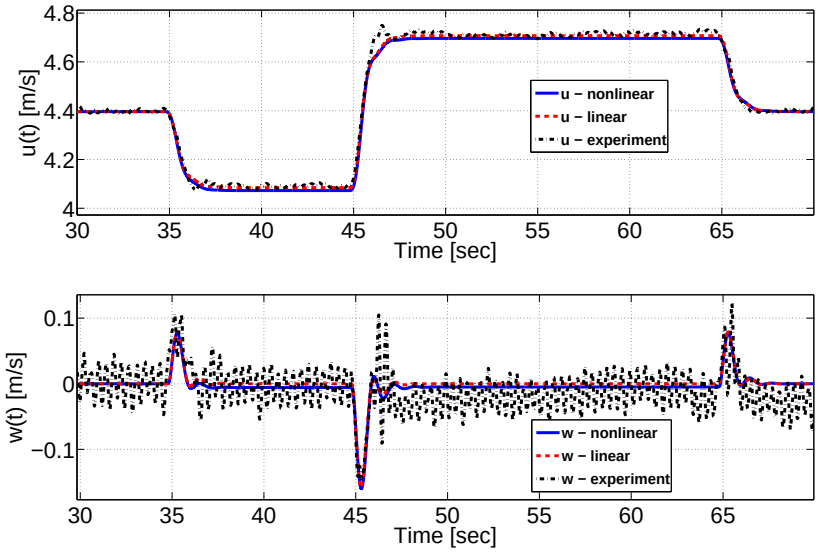

Figure 6.8: Pitch angle reference tracking - velocities u and w

6.3 Gust Generator Disturbance Rejection

The HSSV closed-loop system performance subject to the perturbed flow is evaluated in this section through the experimental results of the test vehicle response to the gust generator oscillations described in Section 5.3. The gust generator effect on the vehicle motion is not simulated through the linear and nonlinear equations of motion because of the complexity of analytical models describing the fin angle of attack as a function of the gust generator oscillations. In fact, one of the benefits of the HyTPSV platform is its ability to perform experiments that are complex to reproduce in a computer simulation.

The control surface deflections, δ_c and δ_f, as well as the cavitator and fin forces scaled to their corresponding surface deflections are shown in Figures 6.9 and 6.10 respectively. For visualization purposes, offsets in the cavitator deflection and cavitator force are removed.

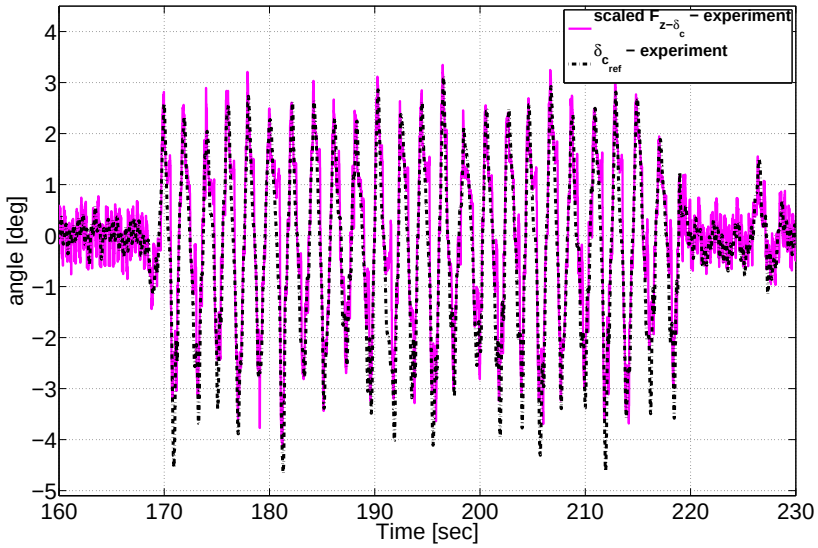

Figure 6.9: Gust disturbance rejection - cavitator deflection and force

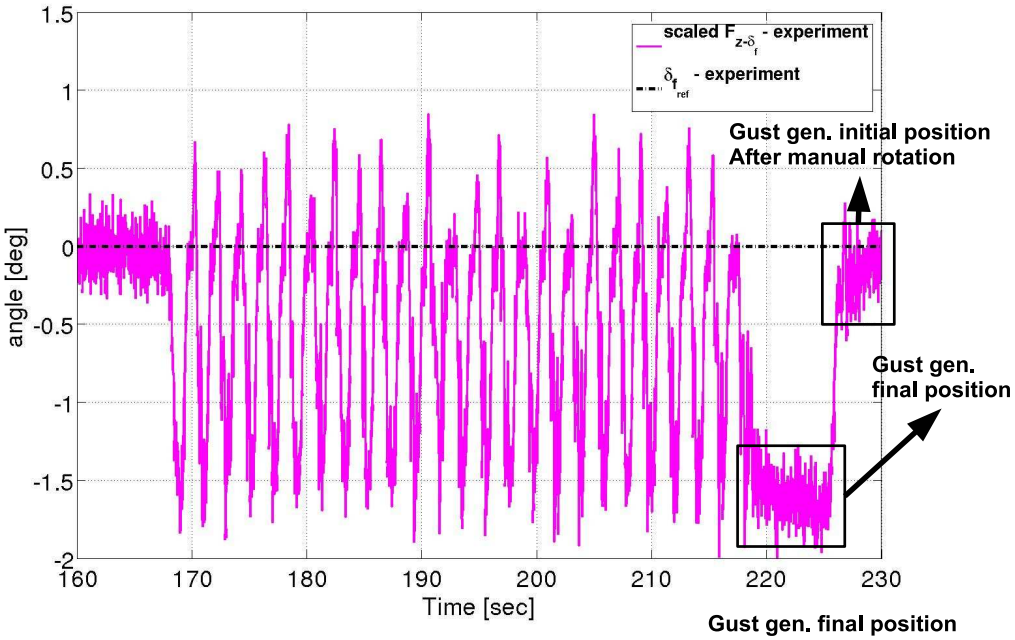

Figure 6.10: Gust disturbance rejection - fin deflection and force

Figure 6.9 shows good agreement between the cavitator deflection generated by the controller and cavitator scaled force computed in the MSC. Figure 6.10 shows that during the fluid perturbations the scaled fin force (F_{δ_f}) oscillates between -2 and 0.7 degrees at 0.5 Hz (frequency of the gust generator). The results from Figures 6.9 and 6.10 successfully validate the force transformation approach in which the cavitator force is associated with only cavitator deflection, whereas the fin force is associated with both fin deflection and perturbed flow. Figure 6.10 also shows that the values of the steady fin forces before and after the gust oscillation are different. This occurs because the gust generator initial and final positions were different. Near second 225, the gust was manually moved to its initial position and therefore the scaled fin force went back to zero. Moreover, Figure 6.10 shows that the fin force oscillations are not symmetric with respect to zero. This is due to the fact that the force transducer was zeroed out with the gust generator located near its maximum deflection.

The pitch angle and pitch rate responses to the gust generator oscillations are shown in Figure 6.11. Despite the perturbations, the closed-loop system maintains the pitch angle close to zero, which is the pitch angle reference command during this part of the experiment.

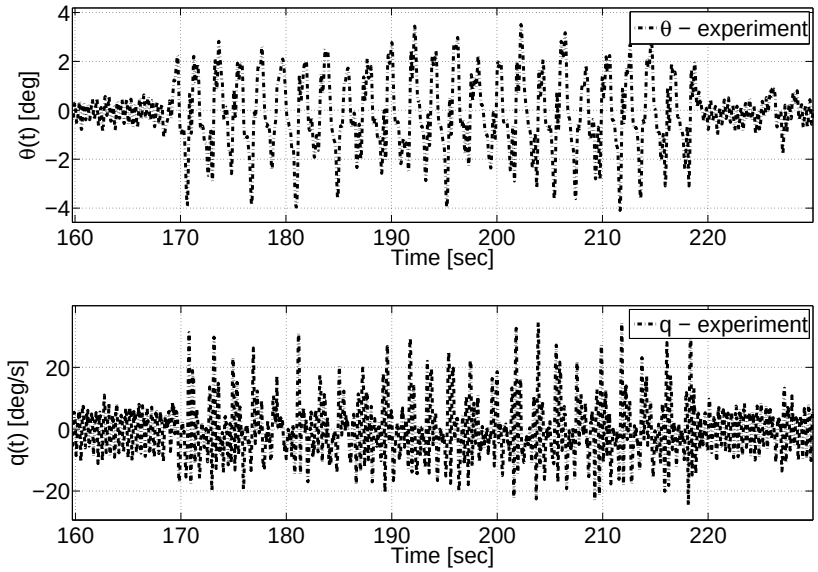

Figure 6.11: Gust disturbance rejection - pitch angle and rate

The longitudinal components of the vehicle velocity (u and w) are presented in Figure 6.12.

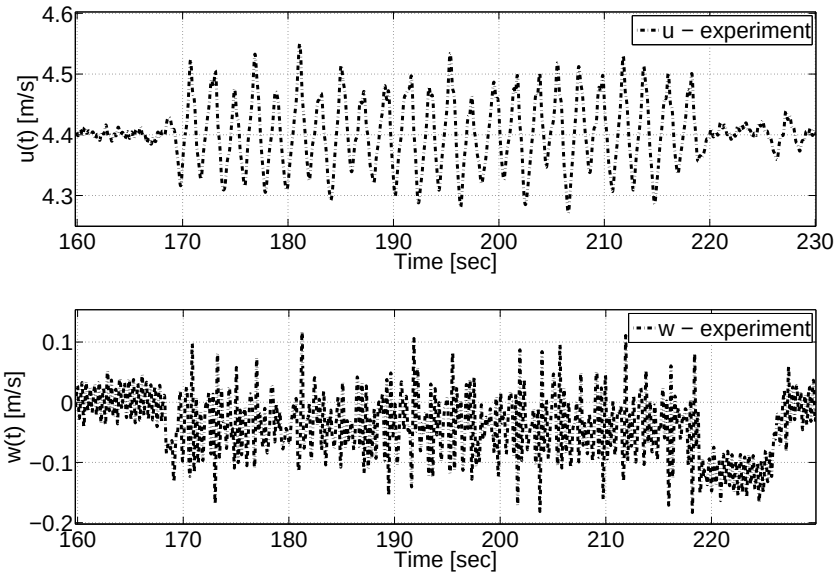

Figure 6.12: Gust disturbance rejection - velocities u and w

6.4 Validation of Linearity in System Operation

The HyTPSV platform is constructed under the assumption that the linear equations of motion accurately follow the nonlinear dynamics. This can be qualitatively validated by checking the agreement between the HyTPSV data and linear simulations with the nonlinear dynamics for the considered reference commands and perturbations. An approach to quantitatively validate the operation of the system in the linear regime is evaluating the magnitude of the cavitator and fin angles of attack (α_c and α_f). The fin angle of attack should not exceed 7 degrees of magnitude, which corresponds to the maximum value used to obtain the fin force models. Similarly, the cavitator angle of attack should follow $cos(\alpha_c) \approx 0$, $sin(\delta_c) \approx \delta_c$.

The cavitator and fin angles of attack for all three parts of the experiment described in Section 5.3 are shown in Figure 6.13. Notice that the angles of attack are constructed by using data from both flight computer (δ_c, δ_c) and MSC (q, w). Equations 4.40 and 4.43 are used to compute α_c and α_f respectively. According to Figure 6.13 the magnitudes of α_c and α_f do not exceed 10 and 6 degrees respectively; therefore, the

linear approximations hold for the HyTPSV experiment described in this chapter.

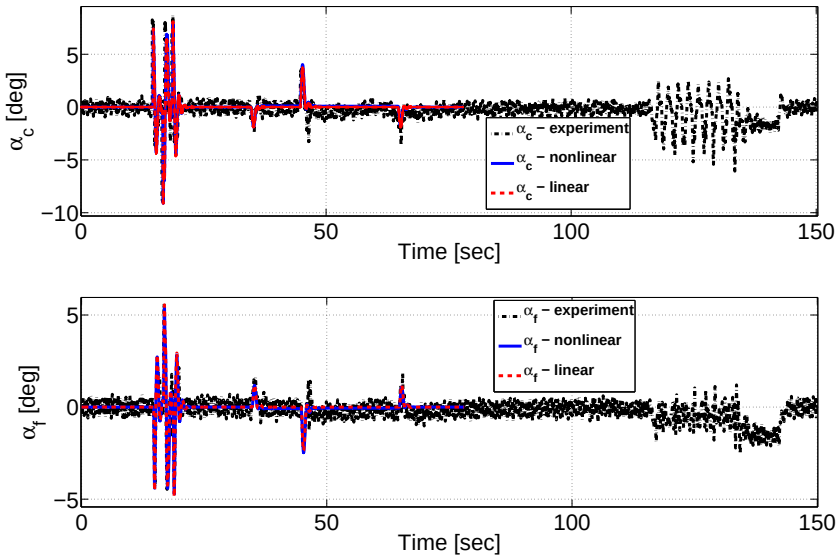

Figure 6.13: Cavitator and fin angles of attack

Chapter 7

Conclusions and Future Directions

This chapter presents conclusions and future directions on the modeling and control validation work developed throughout this thesis. Section 7.1 summarizes important findings and future recommendations about the vehicle motion and forces generated by the cavitator, fins, perturbed flow, and planing. Section 7.2 presents the main features and results of the control test platform described in Section 5.1. Recommendations on further control strategies and experimental work are also given in Section 5.1. Finally, Section 7.3 proposes a new test platform capable to overcome limitations of the control test platform developed through this thesis, that is, the lack of being able to capture the fin immersion variations and planing.

7.1 Model Validation

This section presents conclusions and future directions on the modeling of supercavitating vehicles presented in this thesis. Future directions are focused on experimental work to be performed in the SAFL high speed water tunnel.

7.1.1 Model Validation Conclusions

Cavitator Forces

The contribution of a disk cavitator to the supercavitating vehicle motion is given by the cavitator forces expressed in the body frame (X_b, Y_b, Z_b), which is attached to the vehicle center of gravity. The net force ($F_{cav} = \frac{1}{2}\rho||V_{cav}||^2 A_c C_{D0}(1+\sigma)\cos(\alpha_c)$) applied at the cavitator center of pressure is always normal to the cavitator surface since tangential forces are negligible. If the cavitator has zero deflection ($\delta_c = 0$), then the net force is parallel to X_b, which results in zero force along Z_b and therefore zero moment about Y_b.

The cavitator forces expressed in the body frame and for small angles α_c and δ_c can be approximated as $F_{x_{cav}} \approx -\frac{1}{2}\rho||V_{cav}||^2 A_c C_{D0}(1+\sigma)$ and $F_{z_{cav}} \approx \frac{1}{2}\rho||V_{cav}||^2 A_c C_{D0}(1+\sigma)\delta_c$. These expressions indicate that the force along Z_b is mainly dependent on the cavitator deflection, but not on the motion of its center of pressure. Moreover, according to the approximation, the cavitator force along X_b is constant.

For the above reasons q, w, and deviations of u from U_0 do not contribute to the forces generated by the cavitator. In addition, perturbed flow varying α_c has negligible effect on the cavitator forces expressed in the body frame.

Fin Forces

In contrast with the cavitator, forces generated by the fins and expressed in the vehicle body frame are function of the states u, w, and q as well as the fin deflection δ_f. This occurs because at nonzero angles of attack the fin force components in the X_b and Z_b axes are both nonzero. Furthermore, the fins are the principal means for achieving vehicle open-loop stability because they generate restoring forces that decelerate the vehicle rotation about Y_b and motion along Z_b.

Perturbed Flow

A supercavitating vehicle has tremendous advantage over conventional underwater vehicles in terms of rejection of flow perturbations. This occurs because a HSSV has less wetted area exposed to the fluid. Perturbed flow produced by oscillations of the gust

generator results in much smaller force oscillations acting on the test vehicle when the supercavity is established, as shown in Section 4.1.3.

Specifically, for a supercavitating vehicle with a disk cavitator and lateral wedge fins, perturbed flow varies the cavitator and fin angles of attack, but only the fins generate considerable forces that affect the vehicle motion. Therefore, the impact of flow perturbations on the vehicle motion can be modeled through perturbations of the fin angle of attack or equivalently of the fin deflection.

Planing

From experiments conducted in the SAFL high speed water tunnel and presented in Section 4.1.5, it was observed that planing can be achieved by increasing the cavitator angle of attack through combinations of cavitator deflections and perturbed flow. This suggests that flow perturbations and cavitator actuation should be considered when constructing models of the HSSV motion subject to planing. Finally, according to the experiments, planing forces are comparable with forces produced by large deflections of the control surfaces; hence, the magnitude of these forces highly impacts the HSSV motion.

HSSV Longitudinal Dynamics

The linear dynamical model of the vehicle candidate used throughout his thesis and described in Section 4.2.3 shows that the system has no poles in the right half plane. The pitch rate q and velocity w converge to their initial conditions after impulsive perturbations of the control surface deflections or nonzero initial conditions, whereas pitch angle θ and velocity u do not return to their initial conditions. The later occurs because of the presence of a pole in the imaginary axis. The stable behavior in states q and w is due to restoring forces generated by the fin motion that decelerate the rotation of the vehicle about Y_b and motion along Z_b.

7.1.2 Model Validation Future Directions

Fins

Accurate models of the HSSV motion should consider the effect of fin immersion on the fin forces. The fin immersion is critical in the longitudinal and lateral motion of the vehicle. Longitudinal displacements of the supercavity with respect to the vehicle produce variations in the lift and drag forces at the fins. Similarly, lateral displacements of the supercavity with respect to the vehicle produce variations in the torque about X_b. Mathematical models of the fin forces as a function of the immersion can be constructed through measurements of forces at different immersions and fin angles of attack. Considerable variations in fin immersion can be achieved by using the current experimental infrastructure, but with a few modifications. Hence, an experiment to acquire fin force data as a function of fin immersion and fin angle of attack is proposed as follows: The test vehicle described in Section 3.1.3 should be modified such that the fin axis Y_f becomes parallel to the vehicle body axis Z_b as shown in Figure 7.1. For this experiment only one fin should be used to avoid indetermination of fin forces as a function of fin immersion. The fin immersion can be varied in two ways: First, using the cavitator angle of attack to deform the cavity axis and vary the position of the bubble respect to the fin. Second, by using fins with different span (b). In either case, the immersion should be computed using the position of the supercavity boundary with respect to the fins, which can be obtained throughout pictures of the bubble and test vehicle.

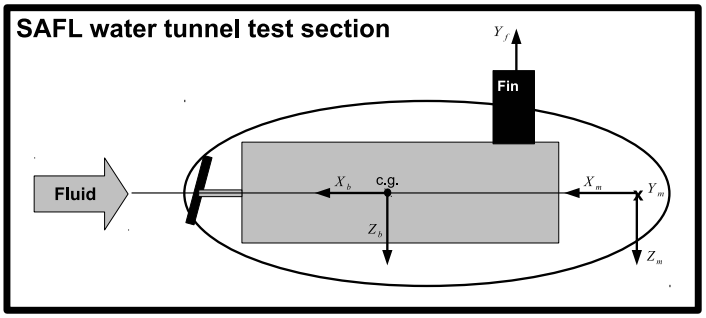

Figure 7.1: Proposed experiment for fin immersion

For the computation of lift and drag forces, it is assumed that the fin deflection is

equal to the fin angle of attack ($\delta_f \approx \alpha_c$) and forces are measured in the measured frame (X_m, Y_m, Z_m). Notice that the angle of attack now is measured in the lateral plane formed by either X_b and Y_b or Z_f and X_f.

Force variations along Y_m and X_m can be measured when the fin is deflected. These forces correspond to lift and drag forces respectively. Torque variations about X_m and Y_m can be used to compute the position of the fin center of pressure. To accurately separate the force contribution of cavitator and fins, the fin deflections can be sinusoids of frequency f. It is expected that the resulting lift and drag forces will be sinusoids with frequencies f and $2f$ respectively. Notice that the drag force can be approximated as $D_{fin} \approx K_{drag}\alpha_f^2(t) = K_{drag}A_{fin}sin^2(2\pi ft)$, which has frequency equal to $2f$.

Planing

Validation of available models of planing forces or construction of new models can be performed through experimental data to be obtained in the SAFL high speed water tunnel. The infrastructure described in Section 3.1 can be utilized to generate and measure planing forces as well as to compute the immersion depth and angle of the vehicle aft end. Planing can be generated by varying the cavitator angle of attack as described in Sections 3.2.5 and 4.1.5. The immersion depth and angle could be computed by using photographs of the water tunnel test section.

Look up tables can be constructed using data from immersion depth, immersion angle, and planing forces in the body frame. The data can be also used to validate available models, for example, Logvinovich [11].

As a recommendation, the immersion depth and angle should be derived as a function of the vehicle states, cavitator trajectory, and cavitator angle of attack. Similar derivations have been presented in [3] and [24], but they do not consider the effect of the cavitator angle of attack.

Scaling of Vehicle Dynamics

Experiments in the SAFL high speed water tunnel are carried out with a vehicle prototype whose dimensions and velocities are smaller than those of a real vehicle. Therefore, equivalence in terms of dimensions and flight conditions between the scaled prototype vehicle and the real vehicle need further analysis.

7.2 Control Validation

This section presents conclusions and future directions on the control validation work presented in this thesis. Future directions are focused on experimental work to be performed in the SAFL high speed water tunnel.

7.2.1 Control Validation Conclusions

The hybrid test platform for supercavitating vehicles (HyTPSV) is a successful method to test components of a HSSV prototype under realistic flight scenarios. This system assembles a closed loop interconnection that consists of the flight computer, test vehicle with actuated control surfaces, and vehicle dynamics propagated in the motion simulation computer. Important features of this system are as follows.

- The HyTPSV enables software and hardware testing of the HSSV flight computer, where control algorithms are executed in real time. This platform allows the recognition of design errors and implementation constraints that lead to incorrect behaviors of the HSSV close-loop system.
- Complex fluid-vehicle interactions as flow perturbations and hydrodynamic forces and vibrations are captured during testing of the HSSV closed-loop system.
- Mathematical models of time delay and actuation can be validated and updated through the HyTSPV platform. If models represent the behavior of the system components, then simulations and experiments agree as it is demonstrated in Chapter 6.

The above features are validated throughout the experiments presented in Chapter 6, which show agreement with mathematical models of the system components and control laws.

7.2.2 Control Validation Future Directions

The HyTPSV platform can be used for the validation of control strategies and flight scenarios other than those presented in this thesis. Regarding control strategies, if the fin deflections are used, then maneuvers in which motion along Z_b can be sustained

without pitch rotation. Validation of control laws using fins can be performed through the HyTPSV framework. It is recommended to model the fin forces with uncertainties that capture the fin immersion variations. This can be done by treating the slope of lift force versus angle of attack ($\frac{\partial C_{FL}}{\partial \alpha_f}$) as an uncertain parameter.

Furthermore, a variety of flight envelope points can be tested on the HyTPSV platform. For example, if the test platform is slightly modified, then it is possible to validate control laws at different vehicle speeds. The velocity of the SAFL high speed water tunnel should be varied, measured and transmitted to the DPC, where it is used to update the trim velocity (U_0) of the HSSV model.

The next step in testing of control algorithms is to overcome the drawbacks of the HyTPSV platform presented in Section 5.1. A candidate for this system is presented in the following Section.

7.3 Next Generation Test Platform

A new generation test platform can overcome two of the drawbacks presented in Section 5.1, which are the lack in capturing planing and fin immersion variations. These phenomena can be captured through a moving test vehicle constrained to move inside the water tunnel test section. At the same time, this vehicle should approximate the dynamics of an unconstrained supercavitating vehicle flying under the sea. Analysis and simulations of the test vehicle motion are necessary to validate the similarity between the unconstrained and constrained vehicles. A candidate for the next generation test vehicle is presented in the following Section.

7.3.1 Test Vehicle Concept

A first approach for a new test bed is a vehicle with rotational and vertical motion, but without motion along the horizontal axis. It is expected that the vertical velocity and position for the unconstrained and constrained vehicles have agreement. A simulation of the vertical position of the unconstrained vehicle, expressed in the inertial frame, for maneuvers presented in Section 5.3 and Chapter 6 is shown in Figure 7.2. These maneuvers correspond to the response of the HSSV closed-loop system to cavitator perturbations and pitch angle reference commands. The geometrical and inertial

parameters as well as the flight conditions used for the unconstrained vehicle simulation are equal to those used throughout this thesis and presented in Table 4.1.

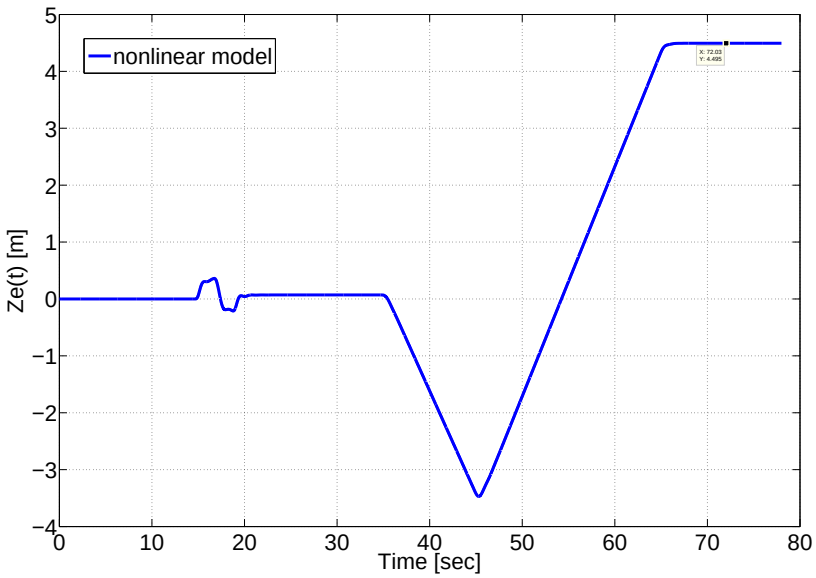

Figure 7.2: Vertical position of HSSV

The maximum vertical position of the vehicle, when cavitator perturbations are applied, is 0.36 [m]. When the closed-loop system tracks reference pitch angles, the maximum value of the vehicle vertical position is 4 [m]. These values exceed the dimensions of the SAFL high speed water tunnel test section. Recall that for these maneuvers it is assumed that the trim forces applied to cavitator and fins are externally supplied. Higher speeds are required to trim the next generation test vehicle. At those speeds the reachable vertical velocity and position are even higher making the test vehicle difficult to operate inside the tunnel. This type of problems can be avoided by using a vehicle with rotation, but not translation. Thus, a rotational test vehicle, depicted in Figure 7.3, is proposed as alternative for the new generation text platform.

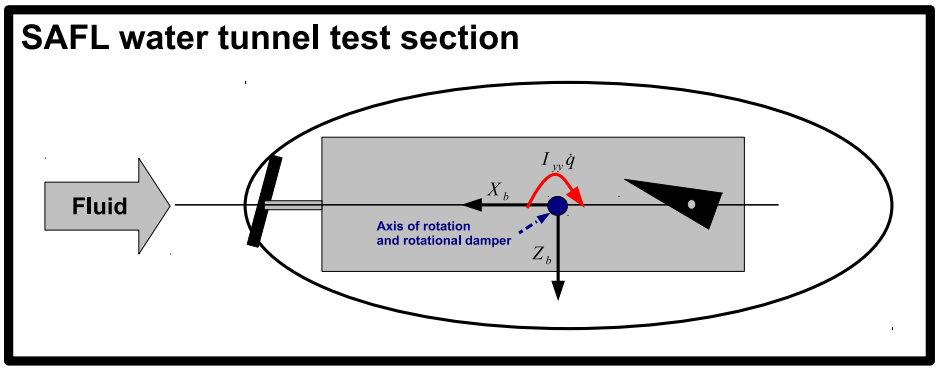

Figure 7.3: Schematic of new generation test vehicle

This vehicle should be capable of rotating about the axis of rotation that pierces the bubble and is connected to a lateral window of the tunnel test section and a rotational damper attached to the other lateral window.

For an unconstrained HSSV, the effect of the translational motion (equation of motion along Z_b) on the rotational motion (equation of motion about Y_b) will lead to increased damping. Therefore, the rotational damper, attached to the constrained vehicle, is placed to substitute the rotational damping effect of the translational motion.

The equations of motion, expressed in the body frame, for the next generation test vehicle are given in expressions 7.1, 7.2, 7.3, 7.4, and 7.5. Notice that planing forces are not included in the equations.

$$u = U_0 cos(\theta) \tag{7.1}$$

$$w = U_0 sin(\theta) \tag{7.2}$$

$$\dot{u} = -U_0 q sin(\theta) \approx U_0 \delta q \delta\theta \approx 0 \tag{7.3}$$

$$\dot{w} = U_0 q cos(\theta) \approx U_0 \delta q \tag{7.4}$$

$$I_{yy}\dot{q} = -l_c F_{z_{cav}} + l_f F_{z_{fins}} + M_{y_{damper}} \tag{7.5}$$

$M_{y_{damper}} \approx -\beta_D q$ is the moment generated by the rotational damper with damping β_D. The damper applies a force that has opposite direction to the vehicle rotation. Forces $F_{z_{cav}}$ and $F_{z_{fins}}$ are given in expressions 4.11 and 4.16 respectively.

Forces generated by the cavitator and fins in the constrained vehicle are function of the relative velocity between the fluid and the center of pressure of the control surfaces. These relative velocities have the equivalent effect to forces generated by the absolute velocity of the control surfaces belonging to the unconstrained HSSV. Nevertheless, the linear approximation of these forces are only function of $U_0 = U_\infty$, which is the velocity of the water tunnel or initial velocity in the linear model of the vehicle motion. The linear equations of motion, in state space form, for the rotational test vehicle are given as follows.

$$\begin{bmatrix} \delta\dot{w} \\ \delta\dot{\theta} \\ \delta\dot{q} \end{bmatrix} = A_{HSSV} \begin{bmatrix} \delta w \\ \delta\theta \\ \delta q \end{bmatrix} + B_{HSSV} \begin{bmatrix} \delta_c^c \\ \delta_f^c \end{bmatrix} \tag{7.6}$$

$$A_{HSSV} = \begin{bmatrix} 0 & 0 & U_0 \\ 0 & 0 & 1 \\ -\frac{l_f}{2I_{yy}}\rho U_0 S_f \frac{\partial C_{FL}}{\partial \alpha_f} & 0 & -\frac{l_f^2}{2I_{yy}}\rho U_0 S_f \frac{\partial C_{FL}}{\partial \alpha_f} - \beta_D \end{bmatrix} \tag{7.7}$$

$$B_{HSSV} = \begin{bmatrix} 0 & 0 \\ 0 & 0 \\ -\frac{l_c}{2I_{yy}}\rho U_0^2 A_c C_{D0}(1+\sigma) & -\frac{l_f}{2I_{yy}}\rho U_0^2 S_f \frac{\partial C_{FL}}{\partial \alpha_f} \end{bmatrix} \tag{7.8}$$

In contrast with the linear equations of motion found in Chapter 4, the state space of the next generation test vehicle does not have u as state. This occurs because the approximation of u is a constant.

7.3.2 Test Vehicle Simulation Results

The objective of this section is to compare the dynamics of the constrained and unconstrained supercavitating vehicles. The geometric and inertial characteristics of both vehicles as well as the flight conditions are equal to those used throughput this thesis and presented in Table 4.1. The transfer functions from inputs $[\delta_c(s), \delta_f(s)]^T$ to outputs

$[w(s), \theta(s), q(s)]^T$ for the unconstrained and constrained vehicles are presented in expressions 7.9 and 7.10 respectively. The damping of the rotational damper attached to the constrained vehicle is set to $\beta_D = 3.73$. For this value of damping, the characteristic polynomials of both constrained and unconstrained systems are equal.

$$G_{cons} = \frac{1}{s^3 + 9.845s^2 + 339.2s} \begin{bmatrix} s(6.037s - 544.6) & s(-16.4s - 1491) \\ -141.8s - 2.215 * 10^{-12} & -339.2s + 1.747 * 10^{-13} \\ s(-141.8s + 1.058 * 10^{-12}) & s(-339.2s + 1.506 * 10^{-13}) \end{bmatrix} \tag{7.9}$$

$$G_{uncons} = \frac{1}{s^3 + 9.845s^2 + 339.2s} \begin{bmatrix} -623.4s & -1491s \\ -141.8s - 994.8 & -339.2s - 5.298 * 10^{-12} \\ s(-141.8s - 994.8) & s(-339.2s + 2.53 * 10^{-12}) \end{bmatrix} \tag{7.10}$$

The responses of the next generation vehicle dynamics to impulses applied to the cavitator and fins, for different values of damping β_D, are shown in Figures 7.4 and 7.5. For comparison purposes, the response of the unconstrained vehicle dynamics derived in Chapter 4 is also presented in Figures 7.4 and 7.5.

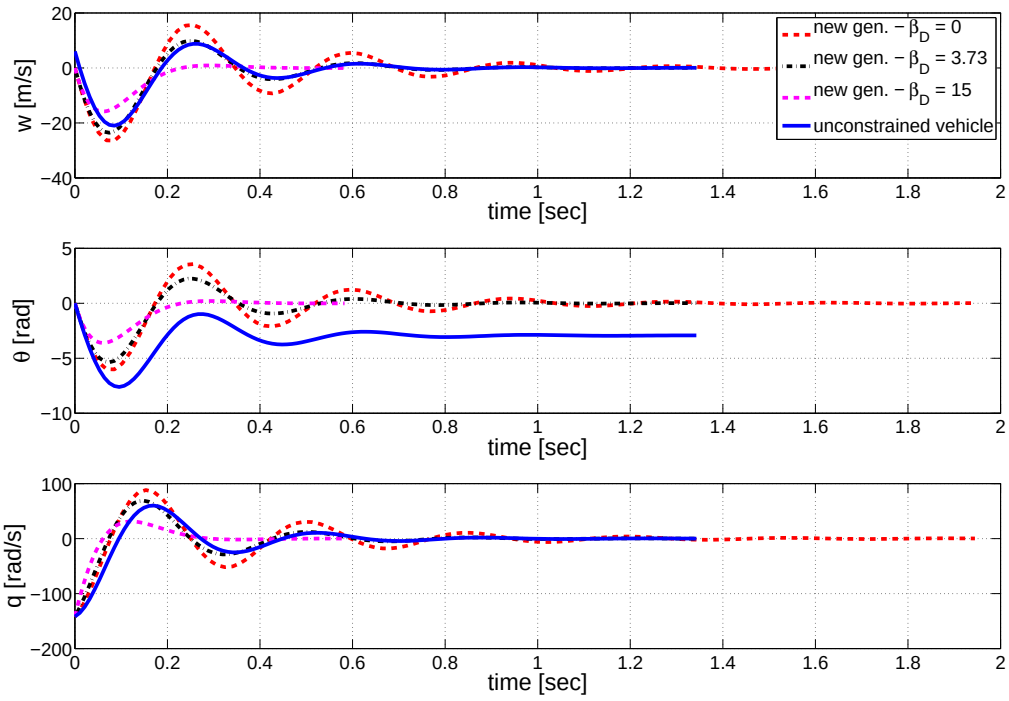

Figure 7.4: Response of next generation test vehicle to cavitator impulse

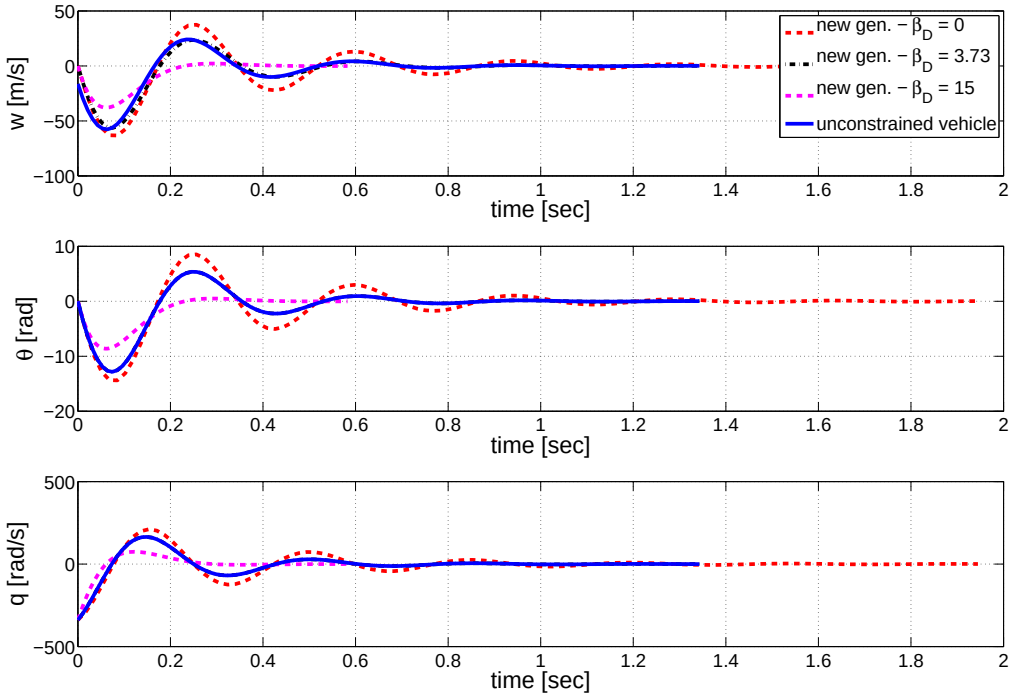

Figure 7.5: Response of next generation test vehicle to fin impulse

Notice that given a value of damping equal to $\beta_D = 3.73$, the next generation test vehicle approaches the dynamics of the unconstrained vehicle. This result demonstrates the suitability of building a rotational test vehicle to emulate HSSV undersea flights in which planing forces and small variations of fin immersion can be captured. Nevertheless, the numerator of the transfer functions impose differences in the dynamics between the unconstrained and constrained vehicles that need further analysis.

7.3.3 Next Generation Control System

The new generation test system could use some of the components of the HyTPSV system; for example, the code generation scripts, simulation tools, and flight computer. The measurement unit to acquire the real-time measurements of pitch angle and rate,

used for control, could be either an encoder attached to the vehicle axis of rotation or a rate gyro inside the vehicle. Finally, control strategies that deal with planing should be designed, simulated, and tested on the new platform.

References

[1] Vanek, B., *Control Methods for High-Speed Supercavitating Vehicles*, Ph.D. thesis, University of Minnesota, 2008.

[2] Ng, K., "Experimental studies in the control of cavitating bodies," *AIAA Guidance, Navigation, and Control Conference and Exhibit*, No. AIAA 2006-6440, Keystone, Colorado, August 2006.

[3] Dzielski, J. and Kurdila, A., "A benchmark control problem for super-cavitating vehicles and an initial investigation of solutions," *Journal of Vibration and Control*, Vol. 9, No. 7, 2003, pp. 791–804.

[4] Mao, X. and Wang, Q., "Nonlinear Control Design for a Supercavitating Vehicle," *IEEE Transactions on control systems technology*, Vol. 17, No. 4, 2009.

[5] Kirschner, I. N., Kring, D. C., Stokes, A. W., Fine, N. E., and Uhlman, J. S., "Control Strategies for Supercavitating Vehicles," *Journal of Vibration and Control*, Vol. 8, 2002.

[6] Vanek, B., Balas, G., and Arndt, R., "Linear, parameter-varying control of a supercavitating vehicle," *Control Engineering Practice*, Vol. 18, No. 9, 2010, pp. 1003 – 1012.

[7] Saouma, V. and Sivaselvan, M., *Hybrid Simulation: Theory, Implementation and Applications*, Balkema-proceedings and monographs in engineering, water, and earth sciences, Taylor and Francis, 2008.

[8] Carrion, J. and Spencer, B., "Model-based Strategies for Real-time Hybrid Testing," Tech. rep., Newmark structural engineering laboratory, University of Illinois at Urbana-Champaign, December 2007.

[9] Doyle, J., Glover, K., Khargonekar, P., and Francis, B., "State-space solutions to standard H2 and H infin; control problems," *Automatic Control, IEEE Transactions on*, Vol. 34, No. 8, aug 1989, pp. 831 –847.

[10] Balas, G., Chiang, R., Packard, A., and Safonov, M., "Robust control toolbox 3 user's guide," Tech. rep., The MathWorks, 2007.

[11] Logvinovich, G., "Hydrodynamics of free-boundary flows," *US Department of Commerce, Washington D.C.*, 1972, translated from the Russian (NASA-TT-F-658).

[12] Kawakami, E. and Arndt, R., "Investigation of the Behavior of Ventilated Supercavities," *Journal of Fluids Engineering*, Vol. 133, No. 9, 2011, pp. 091305.

[13] May, A., "Water entry and cavity-running behavior of missiles," Tech. Rep. SEA-HAC/TR 75-2, Naval Sea Systems Command, 1975.

[14] Wosnik, M. and Arndt, R., "Control Experiments with a Semi-Axisymmetric Supercavity and a Supercavity-Piercing Fin," *7th International Symposium on Cavitation - CAV2009*, Ann Arbor, Michigan, USA, 2009.

[15] Paryshev, E., "The plane problem of immersion of an expanding cylinder through a cylindrical free surface of variable radius," *International Summer School on High Speed Hydrodynamics*, Cheboksary, Russia, 2002.

[16] Willy, C. J., *Attitude Control of an Underwater Vehicle Subjected to Waves*, Master's thesis, Massachusetts Institute of Technology, 1994.

[17] Sabra, G., *Wave Effects on Underwater Vehicles in Shallow Water*, Master's thesis, Massachusetts Institute of Technology, 2003.

[18] Kopriva, J. E., *Experimental Study of a High Performance Partial Cavitating Hydrofoil under Steady and Periodic Flows*, Master's thesis, University of Minnesota, 2006.

[19] Murch, A., "Supercavitation Model Generation III. Design, Assembly, and Operation," Tech. rep., Aerospace Engineering and Mechanics, University of Minnesota, 2011.

[20] Hjartarson, A., *Experimental Study of Control Laws for Supercavitating Vehicles*, Ph.D. thesis, University of Minnesota, USA, 2012.

[21] Rice, J., *Investigation of a Two-Dimensional Hydrofoil in Steady and Unsteady Flows*, Master's thesis, Department of Ocean Engineering, MIT, 1992.

[22] Massa, A., *Embedded software development with ecos*, Prentice Hall, 2002.

[23] "Matlab, Simulink, real-time windows target 3 user's guide," Tech. rep., The MathWorks, 2008.

[24] Vanek, B., Bokor, J., Balas, G. J., and Arndt, R. E., "Longitudinal Motion Control of a High-Speed Supercavitation Vehicle," 2006.

[25] Mokhtarzadeh, H., *Supercavitating Vehicle Modeling and Dynamics for Control*, Master's thesis, University of Minnesota, 2010.

[26] Logvinovich, G., "Some problems in planing surfaces," *Trudy TsAGI*, , No. 2052, 1980, Translated from: Nekotoryye voprosy glissirovaniya i kavitatsii [Some Problems in Planing and Cavitation].

[27] Waid, R., "Cavity shapes for circular disks at angles of attack," Tech. Rep. E-73.4, California Institute of Technology, Hydrodynamics Laboratory, 1957.

[28] Waid, R., "Water Tunnel Investigation of Two-Dimensional Cavities," Tech. Rep. E-73.6, California Institute of Technology, Hydrodynamics Laboratory, 1957.

[29] Kermeen, R., "Experimental investigation of three-dimensional effects on cavitating hydrofoils," Tech. Rep. 47-60, California Institute of Technology, 1960.

[30] Kuklinski, R., Henoch, A. F. C., and Castano, J., "Experimental studies in the control of cavitating bodies," *AIAA Guidance, Navigation, and Control Conference and Exhibit*, No. AIAA 2006-6443, Keystone, Colorado, August 2006.

[31] Fine, N. and Kinnas, S., "A boundary element method for the analysis of the flow around 3-D cavitating hydro-foils," *Journal of Ship Research*, Vol. 31, No. 1, 1993.

[32] Semenenko, V., "Artificial Supercavitation. Physics and Calculation," Tech. rep., National Academy of Sciences - Institute of Hydrodynamics, Ukraine, 2001.

[33] Cechticky, V., Montalto, G., Pasetti, A., and Salerno, N., "The AOCS Framework," *International ESA Conference on Spacecraft Guidance, Navigation and Control Systems*, Frascati, Italy, oct 2002.

[34] Rohlik, O., Pasetti, A., Cechticky, V., and Birrer, I., "Implementing Adaptability in Embedded Software through Aspect Oriented Programming," *IEEE Mechatronics & Robotics 2004*, Aachen, Germany, sep 2004, pp. 85–90.

[35] Cechticky, V., Pasetti, A., and Schaufelberger, W., "The Adaptability Challenge for Embedded Control System Software," *IFAC World Congress 2005*, Prague, Czech Republic, 2005.